8-2016

Development of Position-Dependent Luminescent Sensors: Spectral Rulers and Chemical Sensing Through Tissue

Melissa M. Rogalski
Clemson University

DEVELOPMENT OF POSITION-DEPENDENT LUMINESCENT SENSORS: SPECTRAL RULERS AND CHEMICAL SENSING THROUGH TISSUE

A Dissertation
Presented to
the Graduate School of
Clemson University

In Partial Fulfillment
of the Requirements for the Degree
Doctor of Philosophy
Chemistry

---

by
Melissa M. Rogalski
August 2016

Accepted by:
Dr. Jeffrey N. Anker, Committee Chair
Dr. John D. DesJardins
Dr. George Chumanov
Dr. Joseph Kolis

ABSTRACT

Assessing the performance of medical devices is critical for understanding device function and monitoring pathologies. With the use of a smart device clinically relevant chemical and mechanical information regarding fracture healing may be deduced. For example, strain on the device may be used as a mechanical indicator of weight-bearing capacity. In addition, changes in chemical environment may indicate the development of implant associated infections. Although optical methods are widely used for *ex vivo* strain/motion analysis and for chemical analyses in cells and histological tissue sections, there utility is limited through thick tissue because light scattering reduces spatial resolution. This dissertation presents four novel luminescent sensors that overcome this limitation. The sensors are capable of detecting chemical and physical changes by measuring position or orientation-dependent color/wavelength changes through tissue.

The first three sensors are spectral rulers comprised of two patterned thin films: an encoder strip and an analyzer mask. The encoder strip is either a thin film patterned with stripes of alternating luminescent materials (quantum dots, particles or dyes) or a film containing alternating stripes of a dye that absorbs luminescence from a particle film placed below. The analyzer mask is patterned with a series of alternating transparent windows and opaque stripes equal in width to the encoder lines. The analyzer is overlaid upon the encoder strip such that displacement of the encoder relative to the analyzer modulates the color/spectrum visible through the windows. Relative displacement of the sensor layers is mechanically confined to a single axis. When the substrates are overlaid in the “home position” one line spectrum is observed, and in the “end position,” another

line spectrum is observed. At intermediate positions, spectra are a linear combination of the “home” and “end” spectra. The position-modulated signal is collected by a spectrometer and a spectral intensity ratio from closely spaced emission peaks is calculated. By collecting luminescent spectra, rather than imaging the device surface, the sensors eliminate the need to spatially resolve small features through tissue by measuring displacement as a function of color. We measured micron scale displacements through at least 6 mm of tissue using three types of spectral ruler based upon 1) fluorescence, 2) x-ray excited optical luminescence (XEOL), and 3) near infrared upconversion luminescence. The sensors may be used to investigate strain on orthopedic implants, study interfragmentary motion, or assess tendon/ligament tears.

In addition to monitoring mechanical strain it is important to investigate clinically relevant implant pathologies such as infection. To address this application, we have developed a fourth type of sensor. The sensor monitors changes in local pH, an indicator of biofilm formation, and uses magnetic fields to modulate position and orientation-dependent luminescence. This modulation allows the sensor signal to be separated from background tissue autofluorescence for spectrochemical sensing. This final sensor variation contains a cylindrical magnet with a fluorescent pH indicating surface on one side and a mask on the other. When the pH indicating surface is oriented towards the collection optics, the spectrum generated contains both the sensor and autofluorescence signals. Conversely, when the pH sensor is oriented away, the collected signal is composed solely of background signals.

All four of the sensors described can be used to build smart devices for monitoring pathologies through tissue. Future work will include the application of the strain and chemical sensors *in vivo* and *ex vivo* in animal and cadaveric models.

DEDICATION

This work is dedicated to my parents, **Eileen and Nick Rogalski**, and my brothers, **Daniel and Steven Rogalski**. Without your never ending love and support none of this would have been possible. Thank you for helping me become the person I am today and for always encouraging and believing in me; especially during my days of doubt.

To my parents - Thank you for always encouraging me to pursue my dreams, standing by me every step of the way, and being my number one supporters. Thank you for always instilling in me a good work ethic, a desire for knowledge, teaching me persistence and perseverance, and motivating me to strive for excellence. Although we have been separated by a distance of ~ 700 miles during my time at Clemson, miles don't mean anything. I always knew you were really no more than a phone call away.

To my brothers, my fellow scientists and my lifelong best friends – I am eternally grateful for your support and I am so proud of both of your accomplishments. Dan, my fellow chemist, we make a great lab partner team. Thank you for believing in me and always being a listening ear, especially when I wanted to talk science. Steven, thank you for showing me that with hard work and determination it is possible to achieve your dreams. Watching you complete your P.A. degree has inspired me and helped me to continue to strive towards completion of my own goals.

ACKNOWLEDGMENTS

I would like to acknowledge all those who have inspired me to pursue a degree in science. A special thanks to my professors at Kutztown University where I received my bachelor degree including Dr. Rolf Mayrhofer, Dr. Douglas Swartz II, Dr. Thomas Betts, and Dr. Paul Quinn for encouraging me to pursue a doctoral degree.

I would also like to acknowledge my advisor, Dr. Jeffrey N. Anker for his guidance throughout my time at Clemson beginning with my first research experience as an undergraduate REU student and continuing through my time as a graduate student. Thank you for introducing me to conducting independent scientific research and for the countless hours of mentoring and scientific advice as I worked through my projects. You have helped me develop into the scientist I am today and I know I will take with me the invaluable skills and knowledge you have imparted upon me. Additionally, I would like to thank Dr. John DesJardins for his insightfulness on all mechanical aspects of the project and guidance during our weekly meetings and my committee members Dr. George Chumanov and Dr. Joseph Kolis.

I would like to acknowledge our funding sources that made this work possible. These projects were funded by the NASA/SC Space Grants Palmetto Academy program under award number NNG05G168G, The Center of Biomaterials for Tissue Regeneration (CBTR) under NIH grants 5P20RR021949 and 8P20GM103444, by *NIGMS* of the National Institutes of Health under award number 5P20GM10344-07, and NIH NIBIB under award number 1R21EB019709-01A1.

I have had the pleasure of working with a diverse group of graduate and undergraduate students throughout my time at Clemson. Thank you to my colleagues in the DesJardins lab who have contributed to this project; especially Joshua Lake, Nakul Ravikumar, and Hunter Pelham as well as my team of undergraduates in the Anker lab including Dakotah Anderson, Jonathan Heath, Donald Benza, Ian Adkins, Bobby Smith, and Morgan Jasper. I would also like to thank my fellow graduate students and colleagues in the Anker lab especially, Hongyu Chen, Khanvahn Nyguen, Fenglin Wang, Gretchen Schober, Donald Benza, and Fathima Ameer for not only their insightful scientific conversations, but more importantly for their friendship, support, and laughter on a daily basis.

To my friends, Dr. Sara Comer, Dr. Leah Corley, and Dr. Charles Lowe – you have stood by me through the ups and downs of graduate school and have become my lifelong friends, thank you. With the submissions of this document – we have done it – We are now all PhDs! And lastly, I would like to thank Richard Suckey for believing in me; your everyday words of encouragement have helped me immensely. I couldn't have done it without you; you have been my rock.

TABLE OF CONTENTS

Page

Table of Contents (Continued)

Page

LIST OF TABLES

LIST OF FIGURES

List of Figures (Continued)

Figure Page

List of Figures (Continued)

Figure Page

List of Figures (Continued)

Figure Page

List of Figures (Continued)

Figure Page

List of Figures (Continued)

Figure Page

List of Figures (Continued)

Figure Page

List of Figures (Continued)

Figure Page

List of Figures (Continued)

Figure Page

List of Figures (Continued)

Figure Page

List of Figures (Continued)

Figure Page

CHAPTER ONE

INTRODUCTION

This dissertation presents the development and characterization of position-dependent luminescent sensors for non-invasive measurements through tissue. The sensors provide mechanical and chemical information pertinent to assessing the performance of biomedical devices and monitoring pathologies. The primary focus of this work was to develop spectral rulers to be utilized as strain indicators on the surface of orthopedic implants, capable of measuring micron sized displacements by monitoring color change. This goal was fulfilled by the fabrication and characterization of three sensors: fluorescent, x-ray excited optical luminescent (XEOL), and upconversion luminescent spectral rulers. Additionally this work describes a magnetically actuated pH sensor for the discrimination of sensor signal from tissue autofluorescence backgrounds. The pH sensor may be used to monitor the formation of biofilms/infection on the surface of orthopedic implants.

A brief introduction to key topics covered in the body of this document is provided below followed by a brief summary of the contents of each chapter.

1.1 Strain Measurements for Assessing Fracture Healing

The following section highlights the need for diagnostic tools for monitoring the performance/function of medical devices. Although this section focuses on meeting this need for fracture healing, this need extends to the monitoring of a wide array of device functions, pathologies and healing processes.

Clinical Need

In the United States there is a high number of musculoskeletal injuries reported annually. In 1995, there were approximately 28 million musculoskeletal injuries reported and it is believed that this number will rise as the aging population (> 65 years) continually increases.[1-3] Within this class of injuries there are over 2 million fracture fixation surgeries performed each year. It is estimated that the number of fixation surgeries will rise to ~ 3 million incidences per year by 2025. [2-6] As part of the revision surgery, orthopedic hardware (pins, wires, rods, or plates) is implanted to maintain proper bone position/ alignment. These devices share load with the fracture callus during healing. As bone heals, callus stiffness increases and load sharing between the implanted device and the fracture callus decreases.[7]

Bone healing is a continuous process with typical fracture healing periods ranging from 4 to 40 weeks depending on the type of fracture (transverse, oblique, comminuted, spiral, greenstick, etc.), method of fracture fixation (casts, pins, screws, intramedullary rods, plates, etc), type of bone, and patient characteristics including age and health among other factors. The endpoint of fracture healing is difficult to assess clinically. Currently, there is no "gold standard" for defining the endpoint of healing; however restoration of a bone's mechanical function is essential for fracture repair, and is therefore a critical merit to measure that is indicative of the degree of healing.[7-8]

There is a clinical need for a diagnostic tool that can provide a simple non-invasive assessment of healing by monitoring bone's mechanical properties. A quote from the

literature by Bottlang and Augat in the Journal of Injury, emphasizes and elegantly states the need for such devices:

> "Today, the remaining bottleneck in evidenced-based fracture care is the virtual absence of clinical tools that allow for direct, quantitative assessment of the fracture healing state. While surgeons face an unprecedented choice of novel implants, growth factors, and bone stimulation therapies, ***there remains a lack of evidence on how these novel treatment modalities affect fracture healing***, which can have profound consequences on patient outcome."[9]

Currently, plain x-ray radiographs are used in clinical setting as a non-invasive diagnostic tool. As the fracture callus forms bone calcification increases and an increase in x-ray attenuation is observed.[8] Although plain radiographs are capable of providing images of the fracture gap allowing for fracture geometry and callus formation to be studied, they are incapable of measuring mechanical properties of a healing fracture.[7-8, 10-11] Plain radiographs have an accuracy of ± 5 mm for measurements of bone deformation, making them unsuitable for measuring small scale displacements. When radiographic imaging is combined with marker tracking, radiostereometric analysis (RSA), measurements with accuracy greater than 50 microns can be achieved, however this method requires the implantation of radiopaque markers.[7, 12-13]

The work in chapters 2 and 3 of this dissertation present a novel device (spectral rulers) for assessing these modalities. The approach is capable of providing mechanical measurements by non-invasive means. Below, a brief discussion on measuring

mechanical properties of healing bone is provided, emphasizing the advantage of measuring fracture callus stiffness and the need for a new methodology for non-invasive measurements for internal fixation.

Methods of Strain Measurement

There are several methodologies available for monitoring strain ranging from electrical resistance strain gauges to photoelasticity. Additionally, optical interferometry (Moiré analysis) and fiber-optic sensors can be used for strain measurements. This list is not all inclusive, but rather highlights the variety of techniques available. Although, each of the named techniques has been highly successful at measuring strain, the use of these techniques for *in vivo* strain analysis is limited due to the required instrumentation, limited optical access, or the use of transdermal wiring increasing the risk of infection.

Although these techniques suffer from the above mentioned limitations and cannot be used for extended time periods, *in vivo* strain on bone has been monitored and is reported in the literature. *In vivo* bone strain has been measured as early as 1975 by Lanyon and colleagues.[14] In their study, a 45° rosette strain gauge was attached to the tibia of a 35 year old man and the patient was monitored during periods of running and walking.[14] *In vivo* strain measurements were also reported by Burr et al. in 1996 on the human tibial shaft in response to normal loading conditions and under vigorous activity. The vigorous activities included walking, jogging, and sprinting and were consistent with training conditions for Israeli infantry recruits. Their approach used rosette strain gauges attached to the midshaft and 2 cm below the midshaft of the tibia. The sensors contained

percutaneous wires hooked to an external junction box.[15] These studies provided insight on tibial stress fractures.

Additionally, fracture healing has been studied using instrumented fixation devices. Seide et al. have developed a telemetric strain sensing device to investigate healing in 27 patients who have experienced non-union after the removal of femur fixation devices. The instrumented devices contain a strain gauge and an electronic circuit (12 mm x 12 mm in dimension), a microprocessor and coil. With this instrumented plate the authors were able to measure an increase in stiffness during fracture healing, while radiographs did not yet show signs of healing.[16] Although this study provided useful information regarding healing, the device is bulkier and more complex than the sensor presented in the work here.

Telemetric intramedullary nails have also been used to study fracture healing. In a study by, Schneider et al., loading studies were performed on the femur of a 33 year old man who had been involved in a car accident resulting in a multifragmentary femur fracture. Although the study revealed an increasing fracture stiffness as healing progressed, this study has not been directly compared with other work in the literature and the measurements are the result of a single patient.[17] Burny and colleagues have developed a nail-plate device and monitored strain in a 39 year old male. The authors measured strain 5 and 34 days after implantation. However, this device required the use of percutaneous wires, which may result in an increased infection risk.[10]

In the case of external fixation, several studies have been conducted on measuring bone strain. With external fixation, the deformation of external fixation rods can be easily

monitored. Burny and colleagues have conducted a 20 year study investigated strain on external fixation rods and have shown that by monitoring stiffness they could determine the type of bone healing (i.e. normal, delayed, non-union, callus breakage, etc.).[18]

A study by Richardson et al. using external fixation highlights the importance of monitoring fracture callus stiffness during bone healing. The studies show that monitoring the mechanical aspects of bone may reduce the time to safe weight bearing for patients and reduce the risk of re-fracture.[19] Briefly, the authors performed a comparative study assessing healing using 2 different protocols: (1) monitoring fracture healing by radiographs and (2) monitoring fracture healing using strain sensors attached to the external fixation device to determine fracture stiffness.[19] Although plain x-ray radiographs represent a standard for monitoring fracture healing in clinical practices, they are only able to indicate changes in fracture geometry and the formation of the fracture callus.[7-8] Plain x-ray radiographs are unable to provide biomechanical measurements. In this study, the instrumented external fixation device was used to provide the mechanical assessment. In the medical field, the accepted mechanical stiffness for considering a fracture to be "healed" is 15 N/m degree, 25 % of the bending stiffness for intact bone.[7] The 15 N/m^2 threshold is considered sufficient for allowing a patient to begin weight bearing with a reduced risk of re-fracture.[7, 19-20]

In this study, once this threshold was met, patients in group 2 were allowed to begin weight bearing. From their experimental groups of n =117 (healing monitored by radiographs) and n = 97 (healing monitored by mechanical stiffness measurements) they determined that the second group was able to begin weight bearing a median of 3 weeks

earlier than the radiograph group. Additionally, there were fewer cases of re-fracture, 8 for group one and 0 for group two respectively.

The studies highlighted here for monitoring healing with internal and external fixation devices suggests that monitoring fracture stiffness is an effective way for reducing the time to weight bearing. Similar to these examples, the sensors presented in this work will offer a method for assessing fracture healing. The sensors offer a non-invasive means of measurement that does not require the use of percutaneous wires or complex instrumentation.

Although this section has briefly highlighted the measurement of strain for monitoring fracture healing, fracture healing is not the only biomedical problem that could benefit from measuring mechanical stiffness. Similar to fracture healing, the progression of tendon healing is difficult to monitor non-invasively. We highlight the use of our spectral rulers for tendon healing in chapter 3.

1.2 What is Strain?

Strain is defined as a measure of an object's deformation (i.e. change in size or shape) as a result of an applied load (stress). Mathematically, strain (ε) can be expressed by the following equation: $\Delta L/L_0$, where ΔL is equal to the final – initial length of the specimen and L_0 the initial or reference length.[21-24] In the work presented in this dissertation, spectral rulers are used to measure changes in length by monitoring displacement of two substrates.

Strain can also be expressed in terms of stress (σ) applied to the object and the material's Young's modulus (E) by the equation $\varepsilon = \sigma/E$. Stress is a measure of the force applied to the object per unit cross-sectional area ($\sigma = F/A$) and is often expressed in units of N/m^2 or pascals.[22] The Young's Modulus (also known as the modulus of elasticity) of a material is defined as a measure of a material's resistance to deformation or more simply stated, an object's "stiffness." It is commonly expressed in units of Newtons per meter squared.[23-24]

The strains values that we intend to measure with the sensor described within the body of this work fall within the elastic region of the stress vs. strain curve. Within this region, the object's deformation is reversible with no permanent deformation upon removal of an applied load. Initially, stress vs. strain varies linearly, until reaching the proportional limit. Within the linear region of the stress-strain curve, the slope of the line is equal to the Young's modulus of the material. The strain in this region can be described by Hooke's law, $\varepsilon = \sigma/E$.[23-24] The elastic limit of the material falls above the proportional limit and indicates the transition from elastic deformation to plastic deformation. Plastic deformation results in a permanent irreversible deformation of an object. This transition is often difficult to define; therefore within the plastic region of the curve, a measure of the material's yield strength is defined. The yield strength is typically defined as the point at which a line drawn parallel to the linear portion of the curve and offset by a strain value of 0.2 %, intersects the stress-strain curve.[23-24] As the material strain increases, the maximum stress the material can withstand before breaking

is reached, and is referred to as the tensile strength of the material. Past this point, if enough stress is applied to the object, the object breaks, reaching the fracture point.

1.3 Introduction to Spectral Rulers

This document presents the use of spectral rulers to measure displacements non-invasively through tissue. Spectral rulers are a measurement tool that provide length/distance measurements by monitoring a color/wavelength change using optical methods. Several types of spectral rulers are known and their utility has been demonstrated through a wide variety of biological applications ranging from measuring the length of DNA strands to providing a relationship between distance and concentration of chemical analytes.[25-45] A few types of spectral rulers include FRET and plasmonic spectral rulers and a unique alternative, photonic band gap materials. Each provides a different length scale, with FRET rulers providing the shortest distances, less than 10 nm, and photonic band gap materials with a measurement scale ranging from microns to millimeters. Each ruler has a unique approach for measuring distance, for example FRET rulers measure distance by monitoring fluorescence lifetime decay of donor and acceptor fluorophores and determining luminescence ratios between the donor and acceptor molecules.[28, 36, 39-40, 46] Plasmonic rulers determine length from monitoring shifts in wavelength from optical scattering as a result of a change in orientation or distance between coupled plasmonic dimers or from a change in particle environment.[26, 29, 32, 42-44] Plasmon resonance of metallic particles is not only determined by the size and shape of the particle but also the dielectric environment of the particle.[47] Finally, photonic band

gap materials measure distance by monitoring wavelengths shift as a result of a change in spacing between diffraction elements in ordered arrays.[48-51] Further discussion of these rulers is provided in the introduction of chapter 2.

Our Spectral Ruler Approach

The spectral rulers we describe in chapters 2 and 3 have a simple design, yet provide an elegant and effective method for measuring micron scale displacements with an easily interpreted signal output. Briefly, the sensor contains two substrates with a series of alternating lines of different materials. The bottom layer, the encoder strip, contains alternating opaque stripes of luminescent materials with distinguishable spectral features while the top layer, the analyzer mask contains regions of alternating opaque black ink or transparent windows. When the substrates are overlaid and the encoder is translated relative to the mask, a color change can be observed by eye, camera, or spectrometer. **Figure 1.1** displays an example of the sensor design; as a visual, each type of luminescent material is designated with a unique color. Details on sensor design and luminescent signal collection methods are provided in the following chapters.

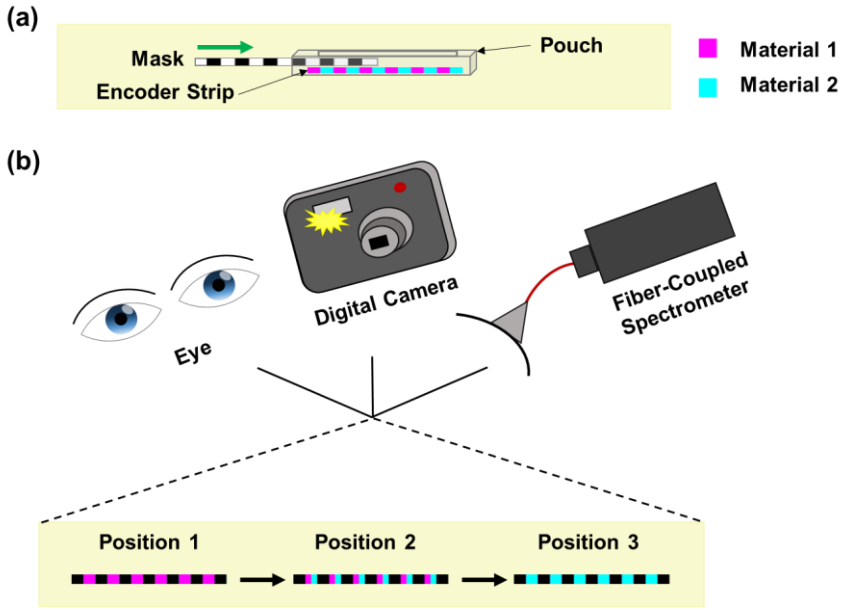

Figure 1.1 (a) Schematic of the spectral ruler sensor design. (b) Spectral ruler in 3 distinct positions showing three different detection methods above for the observed color change.

Figure 1.2 below demonstrates one of the intended uses of the sensor; attachment of the sensor to a fracture fixation device.

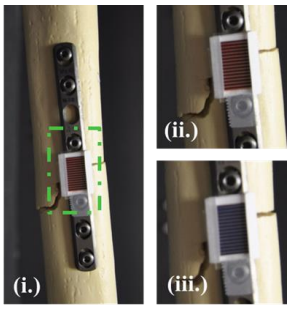

Figure 1.2 (i.) Photograph of a fracture fixation device attached to a bone mimic containing a spectral ruler. The two sensor extremes (red and blue) are shown in (ii.) and

(iii.). The resultant color visible through the windows is altered as the bone is compressed or lengthened.[52]

Using spectral rulers offers a significant advantage over detecting small displacements by imaging luminescent features through tissue. Significant light scattering through tissue imposes limitations on the collection of luminescent images due to an increased point spread function of the photons. (Further discussion on the propagation of photons through tissue is described in section 1.5 of this chapter). With the use of spectral rulers as a measurement tool, the source of the luminescence emission and sharp image features do not need to be resolved. In the presence of tissue the resolution of optical images is reduced due to optical scattering. This phenomena is demonstrated below in **figure 1.3** with a series of alternating colored lines overlaid with a mask. Three unique positions are shown. From top to bottom, the image is progressively blurred to demonstrate the effect of loss in image resolution through increasing depths of tissue. Although it becomes increasingly difficult to resolve individual lines, the sharp transition from one line type to another, or tell that there has been relative motion between the two substrates, the overall color visible through the transparent regions is distinguishable. Using a digital camera or spectrometer, the color/wavelength can be quantified to provide a measurement of displacement of the encoder with respect to the mask.

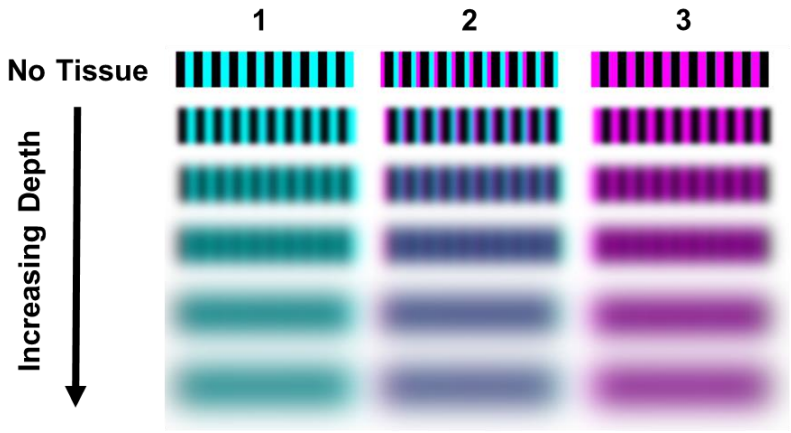

Figure 1.3 Schematic demonstrating the effect of image resolution loss through increasing depths of tissue using a series of patterned lines (spectral ruler design).

1.4 Light interactions with matter

All sensors described in this work are based on the collection and measurement of light generated from luminescent materials. Light interacts with matter in several ways; when light impinges on a sample it is either reflected, absorbed, or scattered. The techniques described in this dissertation focus on light absorption and its subsequent re-emission. Specifically, x-ray excited optical luminescence (XEOL), fluorescence, and upconversion processes will be utilized and discussed. The following section briefly summarizes each of these processes and its utility for analytical measurements through biological tissues.

The Jablonski diagram, **figure 1.4**, depicts several light interactions with matter. The first being light absorption. When light is absorbed by a sample, incoming photons promote electrons from the ground state (S_0) of a molecule to a higher, excited electronic state (example: S_2 or S_1) occurring on the time scale of 10^{-15} s.[53] For this transition to

occur, the incident radiation must have a frequency that is equal to the difference in energy between two states within the irradiated molecule.

Light absorption is described by Beer's law (see equation 1).[54] Beer's law is valid for dilute solutions (< 0.01 M) excited with a monochromatic light source.

$$A = \varepsilon bc \qquad \text{(Equation 1.1)}$$

In the above equation, A is defined as the sample absorbance, ε, a measure of molar absorptivity, and c, is defined as the concentration of the absorbing molecules. Absorbance is determined by measuring the amount of light that is transmitted (T) by the sample and is related to absorbance through the following equation,

$$A = -\log(T) \qquad \text{(Equation 1.2)}$$

Absorbance spectra are typically broad due to the presence of many vibrational energy levels within each electronic level; the electrons may be in one of many excited vibrational states.[53-54]

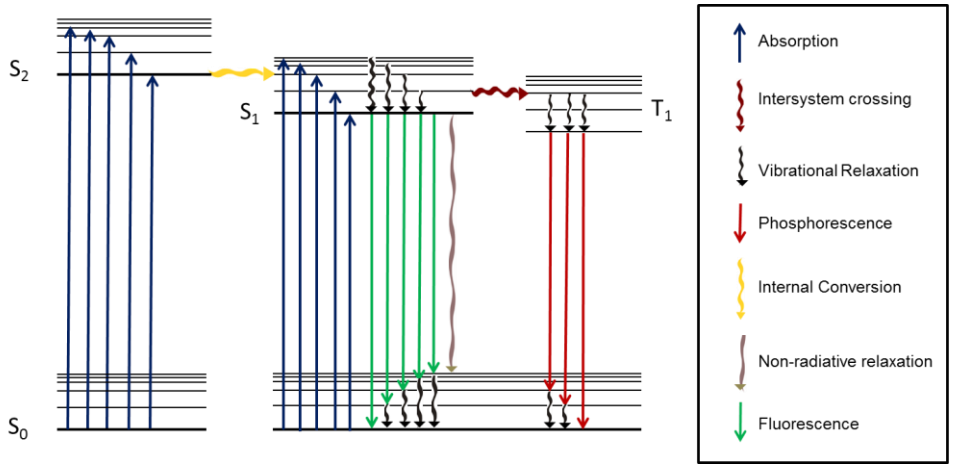

Figure 1.4 Jablonski energy diagram

The absorbance data presented within the body of this work are represented as extinction spectrum, including both absorption and scattering by the sample. Absorption plays a key role in two of the three spectral rulers presented in this work.

Light Emission

When light is absorbed, it has several possibilities for re-emission, including fluorescence, phosphorescence, or energy dissipation as heat. The latter is referred to as a non-radiative decay process and is the result of the conversion of electronic energy into translational, rotational, or vibrational energies while fluorescence and phosphorescence may be broadly defined as luminescence. Luminescence is defined as the emission of light from a body that is not a result of thermal excitation rather it is a result of electronic excitation.[53] Several of these emission processes are also highlighted in the Jablonski diagram (**figure 1.4**).

Fluorescence

Fluorescence, a form of radiative decay, involves the absorption of photons followed by light emission when the excited electrons return to the ground state. Typically electrons are promoted to energy levels S_1 or S_2. Selection rules dictate that for fluorescence to occur, the electronic states involved must have the same spin multiplicity.[53, 55] Fluorescence excited states have a relatively short lifetime, approximately 100 picoseconds to 100 nanoseconds for typical fluorescent dyes.[55-56]

In fluorescence, before returning to the ground state, relaxation of electrons to the lowest vibrational state within the S_1 occurs. Fluorescence from S_2 is not observed due to internal conversion. This internal conversion can be seen in **figure 1.3**. Following this relaxation, the electron returns to a vibrational level within the ground electronic state, S_0, resulting in emission of a photon at a longer wavelength than the incoming excitation light. The emitted photon is of lower energy due to energy loss as heat during the process or as a result of excited-state reactions, energy transfer, or solvent effects. The energy difference between the incoming photons and the subsequent emission ($h\upsilon_{ex} - h\upsilon_{em}$) is referred to as the Stokes shift and was first described by Sir G.G. Stokes in 1852 when observing the blue light emission from quinine excited with UV light.[53, 55] Tuning the Stokes shift is useful in spectroscopy especially for fluorescent measurements through tissue where the fluorescent signal may be obscured by tissue autofluorescence.[55] By increasing the Stokes shift, it is possible to limit the autofluorescence interference.

X-ray Excited Optical Luminescence

X-rays were first discovered by Röntgen in 1895 and have been used extensively for biomedical imaging from x-ray projection imaging to computed tomography scans.[57-58] Imaging of this nature is advantageous because there is low x-ray absorption and scattering in tissue allowing x-rays to penetrate through thick tissue. In the work described in this dissertation, we utilize x-ray excitation to excite scintillator particles doped with rare earth elements (i.e. gadolinium oxysulfide doped with Eu^{3+}). The scintillators convert x-ray energy to visible light through a multi-step process. The host

material of the scintillators first absorbs x-ray energy resulting in the generation of electron-hole pairs. When the energy of the electrons and holes falls below the ionization threshold, the electrons and holes interact with the lattice and lose energy through phonon generation. The reduced energy of the electron-hole pairs approaches the band gap of the material. The electron-hole pairs then transfer energy to the dopant molecules, during a phase referred to as the "migration stage." The electron –hole pairs re-combine and relax via a radiative transition, generating visible light from the dopant/activator that can be detected by a spectrometer.[59-61] This process is termed **x**-ray **e**xcited **o**ptical **l**uminescence (XEOL). The x-ray scintillators we have selected for use in our spectral rulers generate a red light signal with emission peaks at 625 and 700 nanometers. A detailed list of x-ray scintillators available can be found in a review by our group on functional x-ray imaging techniques published in the journal of Physical Chemistry Chemical Physics.[57]

In the work described in this dissertation, we use a film of x-ray scintillator particles as a light source that is "turned" on when irradiated. In our measurements, we pair the x-ray scintillators with a dye that absorbs red light. The dye exhibits an absorbance profile that partially overlaps the emission spectrum of the x-ray scintillators. For our spectral rulers, luminescence from the scintillators passes first through the dye patterned encoder strip followed by the analyzer mask. By altering the amount of dye visible through the mask, the emission signal from the luminescent particles is modulated as the dye absorbs a portion of the particle luminescence. A detailed description of our dye selection and the workings of our sensor, specifically the relationship between spectral output and displacement, are described in detail in chapter 2.

Previously, our group has demonstrated that XEOL is also a useful technique for chemical imaging through the development of an XEOL pH sensor for monitoring bacterial biofilm growth on orthopedic implants.[62] Additionally, we have developed a scanning technique for imaging luminescence through biological tissues.[63-64]

Upconversion Luminescence

Upconversion luminescence is a multi-photon absorption process. Dissimilar to fluorescence, where the emitted luminescence is of longer wavelength than the excitation source, the emitted photons in upconversion luminescence are a shorter wavelength than the photons absorbed. In upconversion, absorption occurs via a sequential process; the upconversion absorption/emission process can be described by one of 3 primary mechanisms. These mechanisms include: (1) excited-state absorption (ESA), energy transfer upconversion (ETU), and photon avalanche.[65-66] The following paragraphs will briefly describe each one of these mechanisms. Additionally, cooperative upconversion (CUC) and energy migration upconversion (EMU) mechanisms have been reported and detailed descriptions of the processes can be found in the literature.[66]

According to the excited-state absorption theory (ESA), a photon is initially absorbed by an ion promoting an electron from the ground state to the first excited energy level, E_1. If the excited state is long-lived, absorption of a second photon can occur that promotes the excited electron to an even higher electronic state. Relaxation of the excited electron results in luminescence emission. This process is one of the least efficient of the known upconversion processes.[66]

In the process energy transfer upconversion (ETU), sequential photon absorption also occurs, however via a slightly different mechanism. ETU requires the excitation of two neighboring ions, a sensitizer and an activator. Both ions are excited by photons to a higher energy level state, E_1. This step is followed by a non-radiative energy transfer from the sensitizer to the activator. Upon relaxation of the activator, light is emitted. This upconversion process is the most efficient, approximately two orders of magnitude more efficient than ESA.[66]

Also, upconversion can occur via a photon avalanche method, a power dependent mechanism. In this case, excited state absorption (ESA) occurs followed by cross-relaxation between the excited ion and a neighboring ground state ion. This cross-relaxation leaves the electron in the first excited state. From this first excited state, the process is repeated; the electrons are promoted to E_2 where cross-relaxation again occurs.[67] Repetition of this process results in an exponential increase in the population of the excited state.[66]

Upconversion Materials

Upconversion particles are composed of inorganic materials and are doped with lanthanide ions that serve as either a sensitizer which absorbs the incoming laser excitation or an activator which controls the wavelength of the photon emission. The lanthanide ions are particularly well-suited for the upconversion process due to the many possible electron configurations (14). Typically host materials for the particles include $NaYF_4$, $NaGdF_4$, Y_2O_3, $LiYF_4$, LaF_3, Lu_2O_3, and $NaLuF_4$ among others. This list highlights

the use of Y^{3+}, Gd^{3+}, and Lu^{3+} as host material cations. These cations are optically inert, containing either a full or half full valence shell and do not interfere with emission of the activator ions. Fluorides are among the list of common host anions due to their low phonon energies; the low phonon energy means there is limited non-radiative decay processes.[68-69]

In this work we utilize Erbium doped upconversion microparticles (4.0 micron mean diameter), containing Yb^{3+} as the sensitizer and Gd_2O_2S as the inorganic host. Yb^{3+} is an excellent sensitizer choice as it has a larger absorption cross-section at 980 nm (the excitation wavelength utilized) than other lanthanide ions. Excitation of Yb^{3+} ($^2F_{7/2} \rightarrow {}^2F_{5/2}$) allows for energy to be transferred to the Er^{3+} activator.[68, 70-71] Our sensors will employ the use of the 660 nm emission peak resulting from the $^4F_{9/2} \rightarrow {}^4I_{15/2}$ transition of the Er^{3+} ion; however there are several other transitions that result in photon emission.[66, 68, 70] These transitions for Er^{3+} are highlighted in **figure 1.5**.

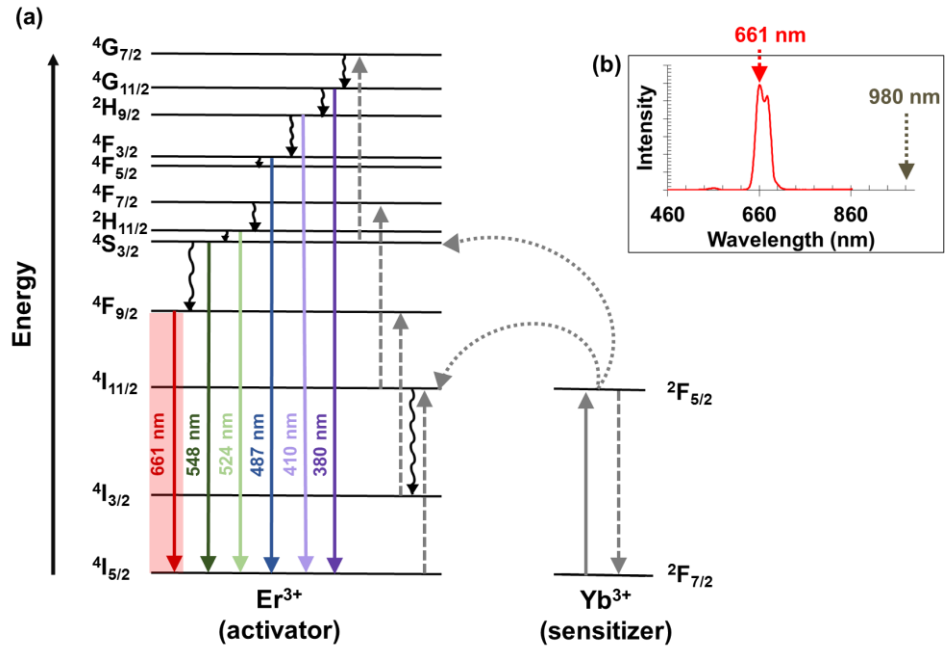

Figure 1.5 (a) Upconversion luminescence transitions for a host material doped with Yb^{3+} as a sensitizer and Er^{3+} as an activator. Transition highlighted in red is utilized in the work presented in chapter 3. Figure adapted from reference number 66. (b) Emission spectrum of Gd_2O_2S:Yb, Er microparticles under 980 nm excitation.

Upconversion particles are particularly attractive for biological studies due to a wide array of advantages over traditional organic fluorescent dyes and quantum dots. The particles are commonly excited with 980 nm or 808 nm light.[68, 71] This near-infrared excitation permits not only deep penetration depths in tissue but also falls within the optimal window for tissue imaging where there is high optical transparency and limited tissue autofluorescence.[72] The resultant emission bands are much narrower than those exhibited by organic dyes (10 – 20 nm FWHM with even narrower fine structure peaks for particles vs ~100 nm FWHM for typical fluorophores). The particles also display

lower toxicity than quantum dots which contain heavy metals.[66, 71] A disadvantage of these particles is their low solubility in aqueous solutions often requiring surface functionalization. Particle size can also be a concern for applications involving injection of particles *in vivo* or intracellular uptake *in vitro*. However, neither is a limitation of the studies presented here because the particles are encapsulated in thin films and protected from solvent.[71]

1.5 Signal Collection through Biological Tissues

When light passes through tissue, a portion of the light is transmitted through the sample and the remaining light is either absorbed, scattered, or reflected.[73-74] The probability of photon re-emission is described by the absorption and scattering coefficients of the tissue as well as an anisotropy parameter.[75]

The wavelength of light strongly affects photon re-emission. Visible light is strongly absorbed and scattered by tissue, especially light less than 650 nm. Often, the wavelength range 650 – 950 nm is referred to as a suitable window for conducting light measurements through tissue. Within this window, less light is scattered and attenuated by biological tissue (skin and fatty tissue) as well as oxygenated and deoxygenated blood than at shorter wavelengths within the visible range of the spectrum.[74, 76] However, within this range, biological tissues are subject to autofluorescence as a result of the presence of amino acids, melanin, collagen, elastin, nicotinamide adenine dinucleotide (NADH) and flavins among other naturally present fluorophores.[77] Additionally, scientists have defined a second region for optical imaging between 1,000 and 1,350 nm.

Within this region, tissue autofluorescence is reduced and the absorption and scattering coefficients are low.[78]

Scattered light, light which undergoes a change in directionality, largely affects the spatial resolution of optical imaging through tissue. Scattered photons traverse a meandering path through tissue with a path length dependent in part by the properties/morphology of the tissue as well as the wavelength of the incoming light.[79]

Several mathematical models including diffusion (radiative transport theory) and random walk theories have been proposed to explain photon trajectories through tissue The intensity of emitted light through tissue is useful for determining fluorescent yields and photon escape probabilities.[75, 80-81] Mathematically, the mean free path of the photons can be defined as $1/ \mu_t$, where μ_t is the sum of the absorption (μ_a) and scattering coefficients (μ_s).[74, 80, 82] Typically the scattering coefficient is much larger than the absorption coefficient, so that the mean free path approximates $1/\mu_s$. On average, the mean free path of photons traversing through tissue is ~ 100 microns, limiting the measurement depth using conventional microscopy approaches if high quality resolution images are necessary.[82]

When considering photon propagation through thick tissue it is necessary to consider a second variable to describe their trajectory, the **transport** mean free path. This variable takes into account multiple scattering events that result in randomization of the photon propagation direction and is defined as the distance required for photons to lose their initial directionality. The transport mean free path typically extends the trajectory of the photons by ~ 10 times the mean free path and can be defined mathematically as $1/ \mu_{s'}$,

where $\mu_{s'}$ is equal to (1-g)*μ_{s}. The variable g accounts for the anisotropic scattering, represents the light scattering in the forward direction, and typically ranges from 0.8 to 1.0. The value of g is dependent on tissue type. For example, the g term for ground chicken muscle tissue is 0.965 at 633 nm (reported by Wilson) using diffusion theory with an "added absorber." For Caucasian human skin tissue (g) is 0.81 as determined by Jacques.[80, 82] Variation on (g) values are reported in the literature for each tissue type as a result of assumptions in the predictive mathematical model.

As tissue thickness is increased, the probability of photon absorption increases along with the mean free path of the photon trajectory (point spread function). Unscattered light is attenuated exponentially with increasing tissue depth.[75, 80]

1.6 Dissertation Outline

Chapter 1 has briefly introduced the concept of position-dependent luminescent measurements used in the four sensor types described in this document. Additionally, this chapter provides pertinent background information for understanding the context of this work. Topics including the need for technologies that assess fracture state, methods of strain detection through tissue, light interactions with matter, and signal collection through biological tissues have been highlighted.

Chapter 2 focuses on the design and concept of the spectral ruler described throughout this dissertation. Proof of concept is demonstrated with the fabrication of spectral rulers with conventional printer ink and subsequent attachment of the sensor to a computer controlled motorized stage. Digital photography is used to track sensor

displacement and MATLAB analysis performed to quantify color change. The focus of the chapter then shifts to modification of the design to measure displacements through tissue. Two variations of the sensor design are discussed; a fluorescent spectral ruler and an x-ray excited optical luminescent ruler. The fluorescent approach offers the advantage of a bright signal using a non-ionizing radiation source; however the chapter discusses autofluorescence limitations observed using red light as an excitation source. To overcome this limitation, x-ray excited optical luminescent (XEOL) sensors were prepared. Calibration curves are presented for each sensor type along with a discussion on measurement reproducibility and signal noise. Additionally, this chapter describes the overarching goal and application for our sensor; attachment of the sensor to a tibial fracture fixation plate to monitor strain during fracture healing to aid in the determination of when safe-weight bearing may begin. The chapter includes preliminary mechanical testing of the sensor attached across the interfragmentary gap of a tibia fracture mimic with a Mark10 Force testing system.

Chapter 3 introduces a modification of the spectral ruler described in chapter 2. The modified sensor allows for excitation using non-ionizing radiation, and is an essentially background-free approach, using 980 nm light to excite the ruler. Spectral rulers patterned with bromocresol green dye and overlaid upon an upconversion luminescent microparticle film (Gd_2O_2S:Yb, Er) are described. Proof-of concept is demonstrated using a similar collection system (microscope objective and spectrometer) to that described in the previous chapter. Additionally, luminescent measurements using a portable collection system are introduced. The portable system will allow for

measurements to be performed in a clinical setting. Calibration curves are presented for both collection systems. Using the portable system, measurement reproducibility and noise are analyzed for the sensor in the presence and absence of tissue. This chapter discusses an alternate biomedical application for the spectral ruler, attachment of the spectral ruler to a tendon/ligament to provide strain information during the healing process. Tendon/ligament injuries are highly prevalent in sports medicine. We describe future mechanical testing proof-of-concept studies for our sensor attached to a synthetic cruciate ligament.

The focus of Chapter 4 shifts away from the spectral rulers that measure physical changes (displacement) and introduces another use for position-dependent luminescence collection through tissue, the measurement of a chemical change (pH). We have selected pH as our target because measuring local pH on the surface of implanted medical devices is clinically relevant for monitoring infection. The chapter describes the sensor design and shows preliminary measurement results for pH 7 and pH 10 sensors through 6 mm of chicken breast tissue. Using magnetic actuation, we demonstrate the removal of a background signal, largely composed of tissue autofluorescence. Removal of tissue autofluorescence can aid in improving sensitivity of the measurements by increasing the signal to noise ratio and removing background interferences that may skew experimental outcomes.

Chapter 5 summarizes the work presented in this text and briefly describes future directions of the project including sensor miniaturization and application as a chemical

sensor. We also introduce the use of the spectral ruler in orthopedic screws to be used along-side the plate/bone sensor.

Finally, the appendices provide information regarding the MATLAB script used for many of the analyses. Additionally presented is an in depth description of the motorized stage and backlash corrections used for all spectral ruler measurements.

CHAPTER TWO

FLUORESCENT AND X-RAY EXCITED OPTICAL LUMINESCENT (XEOL) SPECTRAL RULERS

2.1 Introduction

A wide variety of scientific instruments and applied technologies rely upon measuring displacements via optical, magnetic, ultrasound, and other sensors. Optical displacement measurements are attractive because they can be non-invasively performed at a distance with a wide variety of samples. Optical displacement measurements can be subdivided in two groups: a) tracking objects within an image, and b) spectral rulers. In general, displacement measurements based upon image analysis are useful when objects in the image are well-resolved (e.g. using optical encoders to measure the position of mechanical stages,[83-85] video tracking to measure strain in materials systems,[86-88] single particle tracking to track intracellular transport and diffusion, [89-91] or moiré pattern analysis for measuring topography [92-94]). However, spectral rulers are preferable when the objects cannot be well-resolved (e.g. because there is poor optical access, optical focus or object orientation changes in time, or image resolution is poor due to optical diffraction, scattering, and other effects).

Several types of spectral rulers have been developed and implemented in a wide variety of biological studies.[27-29, 31-41, 46] For example, fluorescence resonance energy (FRET) rulers detect the ratio of donor and acceptor fluorescence emission, which depends on their orientation and separation. FRET is routinely used to monitor conformational changes of biomolecules including nucleic acids, proteins, and DNA.[28-29,

[33, 35-36, 39-40, 46] FRET has also been used to monitor drug release and molecular cleavage by proteases in cells[95-96] and in live animal models.[97] FRET-based spectral rulers offer a sensitive method for determining separation of donor and acceptor fluorophores on the angstrom-nanometer scale, but are limited to a detection distance of less than ~10 nm (distance over which electronic energy transfer occurs). [27, 29, 32, 34] This distance can be extended an order of magnitude by measuring separation-dependent optical scattering of plasmonic nanoparticle dimers, but is still on the <100 nm scale.[29, 34, 38, 41]

Photonic band gap structures such as colloidal crystal arrays and optical fibers have been used to detect displacement and strain over micrometer to millimeter scales. Diffraction in these structures produce relatively sharp spectral features in absorption and transmittance with a peak dependence proportional to the spacing of the diffraction elements and thus to the strain on the sensor. For example, for a photonic structure with a transmittance peak at 600 nm, a 1% strain will cause a 1% (6 nm) shift in transmittance. This sensor technology has been applied to a variety of swelling-induced chemical sensors such as glucose sensing with glucose-dependent swelling contact lenses.[48, 50] Although monitoring reflection provides a simple and elegant readout if the sensors were to be implanted in tissue, the light reflected from the overlying skin and tissue would obscure the much weaker attenuated reflection from the photonic sensor.[73-74] In addition, the peak wavelength is angle dependent and broadens greatly decreasing sensitivity when multiple angles are used, as would occur if they are implanted beneath scattering tissue. Alternatively, fiber optic strain sensors use periodic spacing of high and low refractive index material to generate an interference pattern similar to the photonic crystals, but the

light source is coupled with a fiber allowing remote sensing with an intense light source. Fiber optic strain sensors with fiber Bragg gratings are used to measure mechanical strain in difficult to access samples, ranging from construction materials (e.g., strain in bridges[98-99]) and biomechanical measurements[100] (e.g. strain on bones[101-102], tendons[103-104] and orthopedic plates[105]). These fiber optic sensors provide sensitive measurements over small ranges of strain, but to connect to the light source and detector in biological applications, the fiber must pass through the skin which can cause irritation and infection.

Herein, we describe a novel and versatile type of spectral ruler to measure micron to millimeter displacements through tissue without the use of percutaneous wires or fibers. These spectral rulers are similar in design to an optical encoder and contain two overlaid substrates: a surface patterned with alternating stripes of luminescent materials or dyes (the encoder) and a mask containing opaque regions and transparent windows. Displacement of the encoder with respect to the mask can be quantified based on color visible through the transparent regions. The color change can be quantified from images acquired with a digital camera *in vitro* or by light measurements with a spectrometer for luminescence detection through tissue **(figure 2.1 a - b)**.

An important application is to non-invasively monitor *in vivo* fracture healing, assess load sharing between fixation devices and healing bone, and monitor hardware fatigue. The paper-thin sensor attaches to the surface of a dynamic compression plate or to bone across an interfragmentary gap. This technology may aid in the prevention of premature weight bearing which can result in re-fracture, nonunion, and joint instability.

The end-point of the fracture healing process is challenging for clinicians to define, with healing periods ranging from 4 to more than 40 weeks and healing rates dependent on several patient characteristics and the mode of fracture.[7] There is currently no "gold standard" for determination of the endpoint of the healing process, however a "healed" fracture is characterized by a restoration of mechanical function and bone stiffness used as a mechanical indicator of bone healing.[6-7] Although it is not possible to measure ultimate strength of a callus without breaking it, the stiffness of the callus can be used as an indirect measure, as it increases linearly with ultimate strength, especially at early to intermediate stages of healing.[7-8, 106-107] During the healing process, the implanted hardware shares load with the fracture callus and strain on the implant decreases as the callus stiffness and strength increases.[7]

There are several existing methods for monitoring fracture healing; most commonly in clinical settings, radiographs are used to image fracture callus geometry and monitor calcification of the fracture callus. However, radiographs are incapable of measuring mechanical properties and have low sensitivity during early stages of healing (typically radiographs do not shows signs of healing within the first 6-8 weeks).[7-8, 10, 108] Computed tomography and ultrasound are also used to assess fracture repair; however computed tomography imaging cannot be performed under physiological loading conditions and soft tissue can interfere with ultrasound measurements.[7-8] Additionally, goniometers, optical marker tracking, and fluoroscopic images, can be acquired for loaded and unloaded bone to assess the fracture stiffness.[7]

It is challenging to measure strain on bone and load sharing between a fractured bone and an implant non-invasively with high accuracy. Efforts to measure strain using wireless telemetry have been conducted; Melik and co-workers have demonstrated strain measurements in a rabbit model using an RF-microelectromechanical system with split ring resonators and Graichen et al. have developed a 9-channel telemetry device for measuring strain on orthopedic implants.[108-110] However, wireless telemetry systems require complex electronic systems.

Bone and implant strain has also been detected with the use of instrumented plates requiring percutaneous wire connections; however this method is not suitable for long time monitoring due to equipment limitations as well as an increase in the possibility for infection.[14-15, 111] However, these bonded electrical resistance wire strain gauges have been a gold standard for measuring bone strain. Within this class of strain sensors, a multitude of studies in which rosette strain sensors have been adhered to the tibia surface have been conducted, allowing for strain to be monitored in several directions. Although electrical resistance strain sensors have measured strain *in vivo*, they are susceptible to error from temperature fluctuations/drift and electromagnetic interferences.[21] A detailed review on *in vivo* strain measurements on bone, including tibial fixation can be found in the literature by Nazer et al., with several highlighted studies in which rosette staple and two staple strain gauges have been attached and measurements acquired under different physical activity conditions.[112]

In the case of external fixation, strain can be measured by movement of the fixator pins upon application of load.[7, 10, 20] Burny and colleagues have measured strain

on external fixation rods on a group of 500 patients over a period of 20 years to monitor the increase in strength of the fracture callus during healing.[18] Studies have also shown that by assessing mechanical stiffness thresholds on external fixation devices for tibia injuries, patients could begin weight bearing on an average of three weeks earlier and have a reduced risk for re-fracture over patients whose healing was monitored using plain radiographs.[19]

2.2 Materials and Methods

Fabrication and Calibration of Spectral Rulers by Digital Photography

Spectral ruler encoders were designed with 20 alternating 500 micron linewidth cyan and magenta lines in Inkscape, a graphics program. Ruler encoders were inkjet printed with an Epson R200 inkjet printer onto Boise Aspen® 30 premium recycled paper. The analyzer mask was patterned to contain 500 micron wide black lines with a 500 micron spacer between each and was printed onto a 3M CG6000 multi-purpose transparency film. To mechanically confine the motion to a single axis, the edges of the encoder substrate were folded over to create an enclosure for the analyzer mask. The encoder was attached to an MTS-50 motorized stage and the analyzer mask was held in a fixed position by a clamp neighboring the motorized stage. Stage displacements were controlled with Thor Labs APT software. The stage step size was set to 50 microns. The stage was displaced a total of 500 microns in the forward direction, before reversal. An image of the sensor at each stage position was captured with a Nikon D90 digital camera (camera settings: ¼ second shutter speed, f/5.6 aperture and an exposure compensation of

0 EV, and zoom of 105); at a distance of 14.9 cm from the sample. All images were analyzed in MATLAB and the mean red, green, and blue pixels over the sensor region in each image was determined. From these values a normalized color ratio was calculated and plotted as a function of stage displacement. (Mathematical equations provided in Appendix A).

Motorized Stage Characterization

To characterize the luminescence displacement sensor response, the analyzer mask was maintained in a fixed position while the encoder strip was attached to a motorized stage (model MTS 50 –Z8, Thorlabs, Newton, NJ, USA). Backlash of the motorized stage was characterized independent of the spectral ratios by monitoring position of the movable stage platform by digital photography. A photograph of the motorized stage and fixture for sensor attachment are provided in Appendix B. Images were acquired for each stage displacement and correlated in MATLAB to determine the physical distance translated by the movable block between each consecutive photograph. Distances were measured in number of pixels and converted to microns. Prior to analysis, a pixel to micron conversion factor was determined using an image of a microscope target. See appendix B for details regarding the backlash correction. It was determined that for large displacements, the backlash was greater than at small displacements; the backlash for 10 micron displacements was 7.6 ± 1.6 µm, for 20 micron displacements, 14.0 ± 0.26 µm, for 25 micron displacements, 10.5 ± 0.7 µm, for 35 microns, 10.7 ± 0.5 µm, for 50 microns, 17.8 ± 0.9 µm, and for 100 microns, 18.7 ± 0.8 µm. All

displacements reported were corrected acorrding to these backlash corrections. The reproducibility of stages displacements in a single direction was also characterized and was shown to be reproducible. For a 100 micron step size, the motor moves 100 ± 6.4 µm, for 50 microns, 49.8 ± 2.7, for 35 microns, 34.5 ± 1.8 µm, and for a 25 micron step size, 24.5 ± 2.9 µm in a single direction.

Fabrication of Fluorescent Spectral Rulers

Solid QPP 645 and QPP 665 CdSeS/ZnS core shell quantum dots were purchased from Ocean NanoTechnology, Ltd. (San Diego, CA, USA). Interdigitated spectral rulers with 950 micron linewdths were designed in Graphtec Studio, and cut from Epson scrapbook photo matte paper using a cutting plotter (CE6000-40, Graphtec Irvine, CA, USA). 1.33 ml of 1 mg/ml QPP 645 in hexane was drop coated onto one sensor half and 700 µl of 1 mg/ml QPP 665 in hexane on the other. Sensor halves were let dry at room temperature before assembling. The interdigitated sensor was sealed in a 3 mil laminating pouch (Enhance 3 mil photo card size laminating pouch, Fellowes, Itasca, IL) and sealed using a laminator (Venus 125, Fellowes, Itasca, IL) to ensure particles would not be removed when in contact with the moving analyzer mask. The analyzer mask was patterned with alternating 950 µm wide black lines and transparent spaces and printed on multipurpose transparency film (Product number 23240, Staples, Framingham, MA) with an HP laserjet 1518ni printer. To mechanically confine the sensor to motion along a single axis, the sensor was inserted inside a prefabricated empty laminating pouch containing rigid guides separated by a distance equal to the width of the analyzer (12.35

mm). The laminating pouch was attached to a sheet of Epson matte paper and the sensor was clamped to a movable block on a Thor Labs MTS 50 Z-8 motorized stage using a fixture built in-house. After inserting the analyzer mask, the mask height was raised at each end to approximately the thickness of the sensor so that the mask would have a flat profile above the encoder. The mask was held in a fixed position at each end.

Fabrication of X-ray Excited Optical Luminescent Sensors

Gd_2O_2S:Eu microparticles with a median diameter of 8.0 μm (UKL63/N-R1) were purchased from Phosphor Technology, Ltd. (Stevenage, UK). A 25 mm x 5 mm microparticle film was prepared on a reflective foil sheet; 280 μL of a 500 mg/ml Gd_2O_2S:Eu solution prepared in 5 mg/ml carobxymethyl cellulose sodium (TCI America, Portland, OR, USA) in water was drop coated onto the foil surface. In order to form a uniform rectangular film, the surrounding area was masked off with double-sided tape (Scotch®, 3M), After drying at room temperature, the film was coated with polydimethylsiloxane (Sylgard 184, Dow Corning, Midland, MI)) mixed in a 10:1 ratio of base to curing agent. After curing at room temperature for approximately 24 hours, the film was heated in an oven at 80 °C for 30 minutes. The sensor encoder was patterned in Inkscape with 800 micron bromocresol purple lines with a 1.2 mm space between each, and a line height of 15 mm. The encoder was printed (14 times over the same pattern) using an Epson R200 inkjet printer loaded with a print cartridge (OPT® Brand) containing a 2.9 mg/ml bromocresol purple solution in a mixture of 71.25 % pH 10 buffer (BDH 5078,VWR,West Chester, PA) and reagent alcohol. The encoder was enclosed

inside an empty laminating pouch with rigid guides as described above. The pouch was then overlaid on top of the microparticle film and the layers adhered with double sided tape. The analyzer mask was prepared with alternating 1 mm wide black lines and 1 mm spaces and printed with an HP colorlaserjet 1518ni printer. After aligning the mask over the encoder, the sensor was clamped to the motorized stage.

Luminescent Measurements

The motorized stage with attached spectral ruler was inverted and placed on the stage of an inverted fluorescence microscope (DMI 5000, Leica Microsystems, Germany), 8.38 mm above a 10 x microscope objective. For fluorescence measurements, a 3 mil laminating pouch was placed between the sample and the objective on the microscope stage. The ruler was irradiated with a 5 mW 632.8 nm He−Ne laser (model HRP050-1, Thorlabs, Newton, NJ); the laser output was filtered with a 633 nm laser line excitation filter (Chroma TechnologyCorp, Bellows Falls, VT). The fluorescence emission was captured by the 10 x objective and the emission passed through a 646 nm long pass filter (Chroma Technology Corp, Bellows Falls, VT). A cylindrical lens was placed after the microscope output to focus the light through the slit of a spectrometer (DNS 300, DeltaNu, Laramie, WY) to increase the optical throughput. Diffracted light was detected with a CCD camera (iDUS-20BV, Andor, South Windsor, CT) cooled to –65 °C. See **figure 2.2** for a schematic of the set-up. The spectrometer was controlled with Andor Solis software and the exposure time set to 0.02 s in the absence of tissue and 3.0 s for signals acquired through tissue. For x-ray excited optical luminescence

measurements, the same inverted microscope and spectrometer/CCD instrument were used for collection with a few set-up modifications. The spectral ruler was excited from above with a mini-X x-ray tube with a Ag target (Amptek Inc. MA, USA) operated at 40 kV and a current of 99 mA. The x-ray exposure through tissue was 0.5 s for generation of the hysteresis curve and 3.0 s for small displacement measurements. The distance between the sample and objective was 19.2 mm. In the absence of tissue, the exposure was 0.5 s and the sample height was 12.2 mm. For all x-ray measurements, a plastic petri dish was placed on the microscope stage between the sample and microscope objective.

For all luminescent measurements, the position of the motorized stage was controlled with ThorLabs APT software and the default backlash correction for the software control was 0.050 mm. At each stage position, a spectrum was recorded. Intensity measurements for small displacements were acquired by advancing the stage position 1 step size before returning to the initial position. This motion was repeated resulting in a total of 25 stage positions; at each position a series of 5 spectra were acquired. Spectra were acquired for programmed step sizes of 50, 35, and 25 microns. For spectral measurements through tissue, 6 mm thick chicken breast tissue was wrapped in cling wrap and placed above and below the spectral ruler.

Mechanical Testing

An x-ray excited optical luminescent sensor (fabrication described above) was attached to a tibia mimic with an interfragmentary gap of 8 mm. The bone mimic was loaded with a Mark-10 (model: ESM303) motorized force testing system (Copiague, NY,

USA) in 5 N increments ranging from 0 to 50 N followed by an unloading cycle. The sample was irradiated with an Amptek mini x-ray tube (40kV, 99 mA) and the luminescence emission captured with a collection lens. The signal was then passed through a liquid lightguide (5 mm diameter, 3 ft long) (ThorLabs, Newton, NJ, USA) which directed the emission onto a 50/50 beam splitter (Chroma Technology Corp., Bellows Falls, VT, USA). The diffracted light was then passed through either a 625/90 nm or 708/75 nm bandpass filter before being measured with two photomultiplier tubes (Sens-Tech P30PC-01 Berkshire, UK). Photon counting was performed using a USB-interfaced data acquisition device (model NI 9402 National Instruments, Austin, TX, USA). The force testing system and spectral acquisition were controlled with custom LabVIEW scripts. The signal was acquired with a sampling frequency of 1 MHz and acquisition time 100 ms. For through tissue measurements, a 6 mm thick slice of chicken breast was attached above the spectral ruler.

2.3 Results and Discussion

We developed a novel tool for measuring position/micron scale displacements through biological tissues by collecting position-dependent luminescent signals. These measurements will allow for biomechanical strain and load sharing between fracture fixation devices and developing bone callus to be evaluated to aid physicians in determining when there has been a sufficient restoration of the bone's mechanical function to allow for safe weight bearing to begin. The sensor design is similar to Moiré fringes, superimposed substrates patterned with a series of lines, for displacement

measurements. However, our sensors do not employ the detection of an optical interference pattern but rather provide a position dependent luminescent signal. We have developed spectral rulers comprised of two essential layers: (1) an encoder and (2) an analyzer mask **(figure 2.1a)**. The encoder is a substrate patterned with alternating colored or luminescent lines that is positioned below the analyzer. The analyzer mask is a transparent substrate patterned with alternating opaque lines and transparent spaces; the transparent regions serve as "windows" that allow a portion of the encoder to be viewed. The sensor components are mechanically confined inside a pouch to restrict the motion of the sensor to a single axis. When the two substrates are displaced relative to one another, a color change is observed through the windows that can be detected by a digital camera *in vitro* or by spectrometer for luminescence detection through tissue **(figure 1b)**. The sensors are patterned with a series of lines to provide a sufficient signal; especially in the case of through tissue measurement where the signal intensity collected decreases with increasing tissue thickness.

By detecting displacement based on spectral color change, our approach is capable of bypassing the scattering limits of light associated with imaging of a surface especially through thick tissue. In optical micrscopy, much of the light is scattered by the tissue with a typical mean free scattering path length of ~100 μm. This scattering limits the utility of optical microscopy based upon unscattered ballistic photons for measurements through >~1 mm of tissue, much less than the clinically relevant depth for tibial fixation, due to poor resolution.[57, 113-115] Although the point spread function of scattered light acquired through tissue is on the order of mm to cm, by measuring spectra

instead of using image tracking, our approach is capable of detecting displacements on the micron scale. Although, collecting the luminescent signal through tissue poses several challeneges including spectral distortion and background variations. Selection of closely spaced red or near infrared luminescence peaks can minimize background variation and spectral distortion from wavelength-dependent optical attenuation in the tissue.

We demonstrated proof of concept for our sensor design with calibration of cyan and magenta inkjet printed spectral rulers using digital photography. An encoder patterned with alternating 500 micron wide cyan and magenta stripes was aligned below an analyzer mask printed with black ink. The ruler encoder was attached to a computer controlled motorized stage and the analyzer mask held in a fixed position **(figure 2.1c)**. The position of the encoder relative to the mask was modulated. The stage step size was programmed to 50 microns and the encoder position was increased until reaching a displacement of 500 microns. To demonstrate the reproducibility of the measurements, the stage direction was then reversed. At each stage position the ruler was imaged with a Nikon D90 digital camera. MATLAB scripts loaded each photograph and calculated the mean red, green, and blue intensity over the sensor region. The inset graph in **(figure 2.1d)** is representative of the pixel count for each image as a function of stage displacement. From the mean color values a normalized color ratio was calculated. The normalized ratio as a function of displacement can be seen in **(figure 2.1d)**. Minimal hysteresis (a maximum of 10 microns) between the forward and reverse directions was observed as a result of experimental set-up. The motorized stage has an inherent backlash associated with directional changes. A linear regression fit over the displacement range of

85 to 252 µm was performed to assess systematic error. A root-mean-square (RMS) noise in displacement of ± 2 µm, 0.40% of the dynamic range, was calculated over this displacement range. The noise level for the 500 µm linewidth ruler corresponds to 200 µstrains over a gauge length of 1 cm. This study shows the feasibility of using color change to determine displacement on the micron scale using a simple spectral ruler.

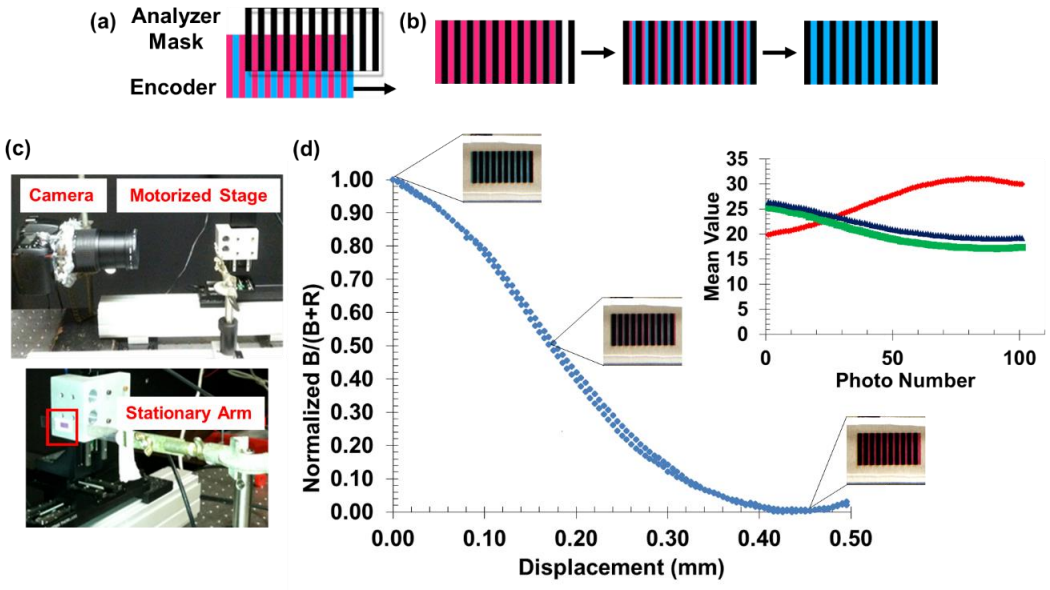

Figure 2.1 (a) Schematic of a spectral ruler showing a dye patterned encoder overlaid with an analyzer mask containing transparent windows that allow a portion of the encoder below to be viewed. (b) As the encoder is moved with the respect to the analyzer mask, the color visible through the windows changes from magenta to cyan. (c) Photograph of the experimental set-up for proof of concept for spectral ruler calibration, highlighting the position of the ruler attached to the motorized stage (red square). (d) Normalized color ratio plotted versus motorized stage displacement for a ruler patterned with 500 micron wide colored lines with photographs of the sensor at select positions.

The inset graph displays the mean color value for each image as determined by a MATLAB algorithm; each consecutive image corresponds to a 50 micron stage displacement. Mean color values were used to calculate the normalized color ratio.

Fluorescent Spectral Rulers

In order to extend this methodology to non-invasively measure displacement/strain through tissue, we replaced the dyed lines in the encoder with luminescent materials. We chose fluorescence as our mode of detection as fluoresence emission has been utilized extensivley through biological tissues and does not require the use of an ionizing radiation source.[116-117] Additionally, fluorescence offers a wide range of options for sensor patterning ranging from organic to inorganic fluorophores as well as fluorescent nanoparticles and quantum dots.

Fluorescent spectral rulers with luminescence emission between 600 – 700 nm were prepared; the sensor encoder was fabricated with two types of spectrally distinct CdSeS/ZnS core shell quantum dots. The encoder was patterned with alternating 950 micron wide stripes of QPP 645 and QPP 665 quantum dots. Quantum dots were selected due to their photostability and chemically stability, especially when encapsulated in a polymeric material, and their relatively narrow spectral emission. Additionally, quantum dots have a broad excitation profile allowing for quantum dots of various sizes to be excited with the same excitation source.[116-117]

The emission spectra of the quantum dots excited by 633 nm laser light are shown in (**figure 2.2 b).** A schematic of the experimental set-up is shown in (**figure 2.2 c**). A

ratio of the fluorescence emission intensity at 660 nm to 683 nm was calculated and used to determine position when the ruler components are displaced relative to one another. We selected closely spaced spectral peaks to minimize spectral distortion associated with a non-uniform background as a result of tissue autofluorescence and wavelength dependent tissue attenuation. For closely spaced peaks, the optical distortion through tissue increases with difference in peak wavelength.

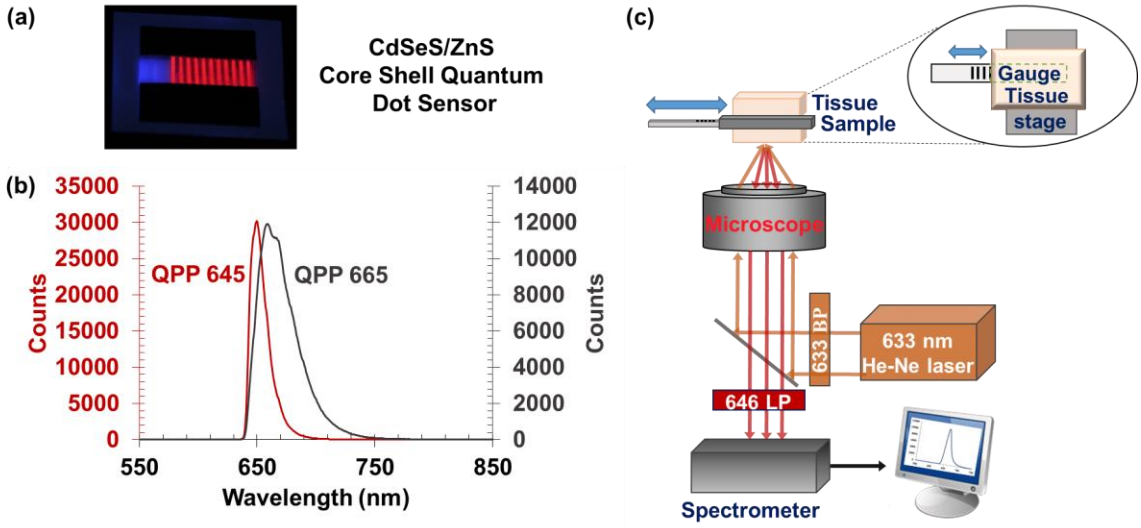

Figure 2.2 (a) Photograph of an interdigitated QPP 645/ QPP 665 quantum dot sensor under a UV lamp (365 nm). (b) Overlaid emission spectra of the particles under 633 nm excitation. (c) Schematic of the experimental set-up illustrating the light path of the 633 nm laser as it is directed towards the sample and the collection of fluorescence emission of the sample by the same microscope objective.

To generate a calibration curve, luminescence measurements were acquired for a series of 40 consecutive 50 micron displacements in one direction. A total displacement of 2.0 mm was performed, corresponding to a full change in the calculated ratio. To determine sensor hysteresis, the displacement direction was then reversed. **Figure 2.3b** shows the ratio of 660 nm to 683 nm fluorescence emission intensity at each sensor position; a log scale is used to show the magnitude of the overall ratio change. Highlighted points, A, B, and C represent the individual spectra displayed in **(figure 2.3a)**; masking of the QPP 665 and unmasking of the QPP 645 particles is evident by the change in the luminescence signal. Additionally, the sensor was evaluated for its ability to measure small fluctuations **(figure 2.3c).** The motorized stage was repeatedly advanced and reversed a single step size; 5 spectra were acquired at each position. In the absence of tissue, we measured 14.5 µm displacements with a noise level (standard deviation of the ratio at a single position) of approximately ~ 0.7 µm. We except that we can measure a displacement of 0.7 µm in the absence of tissue but are limited by the backlash of the motorized stage. The noise level on the signal (in photelectrons) was determined to be an average 0.25 % for 14.5, 24.3, and 32.2 µm displacements in comparison with an expected shot noise level of 0.16 %. Percentage shot noise can be represented as

$$\%N = \sqrt{\frac{1}{I_1} + \frac{1}{I_2}}$$

where I_1 and I_2 represent the number of photoelectrons at each position.

When there was no motion of the stage, the noise level was 0.20 %, corresponding to a 0.51 µm error in position. We attribute the difference between values for no displacement and stage displacements to error in the motion mechanism of the stage. Although there is a slight increase between expected shot noise and noise observed in the absence of motion, we conclude that the main noise contribution is shot noise. Additionally, there may be contribution for read noise, and alignment errors of the sensor. The read noise for the CCD is 12 photelectrons per pixel for a readout rate of 100 kHz. In our measurements, I_1 and I_2 represent the average photoelectrons over a width of 11 pixels. This corresponds to a low read noise of ~ 40 photoelectrons.

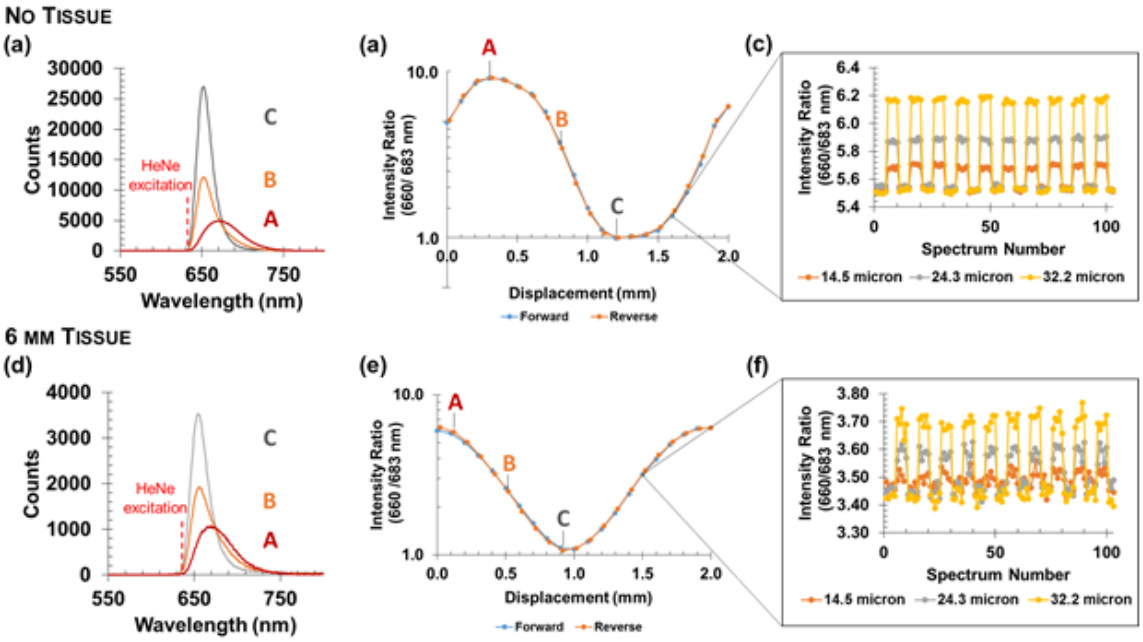

Figure 2.3 (a) and (d) show fluorescence spectra at 3 different stage positions in the absence of tissue and through 6 mm thick chicken breast tissue respectively. (b) and (e) show the fluorescence intensity ratio (660 / 715 nm) plotted on a log scale vs.

displacement of the motorized stage. The stage was advanced in 100 micron increments until a maximum displacement of 2.0 mm was reached. The direction of the stage was then reversed and the displacements repeated in the opposite direction. (c) and (f) show reproducible measurements for small displacements in the forward and reverse directions. 24.3 microns can be seen through 6 mm of tissue. Displacements were corrected for backlash of the motorized stage.

All measurements were repeated through chicken breast tissue. With an initial target of measuring strain on the surface of dynamic compression plates for tibial fixation or strain across the interfragmentary gap for tibial injuries, we selected a tissue thickness of 6 mm. On average, the clinically relevant depth for tibial fixation is aprroximately 5 mm.[115] The results of the luminescence study are shown in **(figure 2.3d-f)**. To ensure a sufficiently strong signal through tissue, the exposure time was increased from 0.02 to 3.0 seconds. An autofluorescent background was observed as a result of excitation of endogenous fluorescent species within the tissue (e.g. amino acids, melanin, collagen, elastin, nicotinamide adenine dinucleotide (NADH) and flavins among other naturally present fluorophores can contribute).[77] We fit the spectra to a linear combination of three base spectra to remove the autofluorescent background (**figure 2.3d**). See **figure 2.4**, for spectra before and after background removal. Alternatively, in order to account for the background, a spectral reference region can be added to the sensor to assess the tissue contribution to the overall luminescnece signal or tissue autofluorescence may be reduced by patterning sensors with quantum dots that emit in the near-infrared spectral range or

with single-walled carbon nanotubes. Single walled carbon nanotubes have been utitilzed for fluorescence imaging through tissue beacuse they have tunable emission in the 900 – 1,600 nm spectral range.[78, 118-122] Studies have shown that light in the 1,100 nm – 1,400 nm has low absorption and scattering and biological tissue generate very low autofluorescence in this region.[78, 118-119] Additionally, SWCNT provide narrow spectral peaks; the use of closely spaced narrow peaks would improve possible tissue distortion.

Comparison of the calibration curves in the presence and absence of tissue reveals a change in the overall shape of the curve. In both cases, the sensor lines are out of focus. We would expect in the absence of tissue with optimal focus that the curve would appear flat until reaching a sharp transition between the two luminescent materials. However, although **figure 2.3b** reveals that the magnitude of the spectral ratio changes near the transition point are less in magnitude, the curve does not become flat; the change is gradual. When tissue is added to the sample, we see an even further deviation. The illuminated area of the sensor increases and roughly approximates the tissue thickness (6 mm). As the illuminated spot size increases we expect the transition from one luminescent line to another to become less sharp. This phenomenon is observed in **figure 2.3e**.

Additionally, the shape of the calibration curve can be explained by considering the physical transition from one material to the other. The transition is not sharp, resulting in a rounding of the calibration curve. For an out of focus sample, with a sharp tranistion between material types, we would expect the shape of the curve to be saw-tooth.

In this study, after removal of the tissue autofluorescent signal, spectral ratios for small displacement measurements showed that reproducible 24.3 µm displacements could be observed through 6 mm thick chicken breast with a noise level of 2.6 µm. Similar to our measurements in the absence of tissue, our observed noise level on the signal was greater than the expected shot noise, 0.64 % and 0.36 % respectively. In the absence of stage motion, the percentage noise was 0.55 %, corresponding to a 2.1 µm error in position. In order to improve our observed noise level, we must consider several parameters including sensor area, particle film thickness/particle concentration, and depth at which our sensor is implanted. The overall signal intensity scales with tissue depth, as the illuminated area is approximately proportional to the tissue thickness.

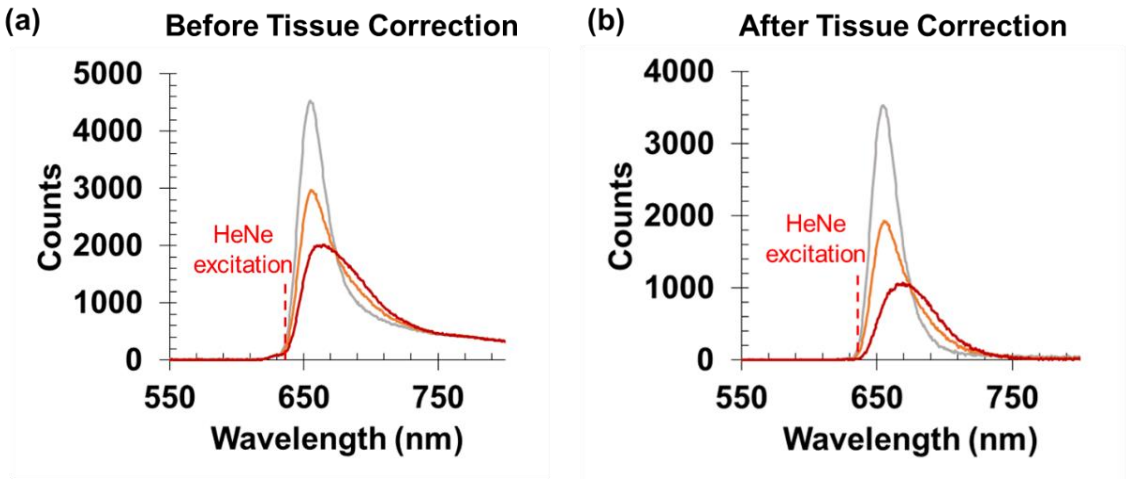

Figure 2.4 (a) Fluorescence emission at three different stage positions before the removal of the autofluorescence background from the chicken. (b) Fluorescence emission spectra of the same three positions after linear algebra was used to subtract out the background resulting in a flat baseline at wavelengths greater than ~ 725 nm.

The resolution and dynamic range of our sensors can be tuned during the fabrication process and is defined by the sensor linewidth and precision. Currently, by inkjet printing, we are limited to a linewidth of approximately 250 microns due to the printer specifications of our conventional desktop printer as well as ink spreading as a result of capillary action in the cellulose substrate. The linewidth of the interdigitated spectral rulers, as described for the fluorescent measurements, is defined by the susbtrate; a crucial factor in determining the resolution in xurography. Using a similar Graphtec cutting instrument (FC5100A-75) to our CE6000 model, Bartholomeusz et. al have shown that micron sized channels may be achieved in a variety of materials including polyester, vinyl, aluminum, and thermal laminate.[123] By careful selection of the substrate material, we may be able to significantly reduce our sensor size. Additionally, we may use one of the many lithography techniques available such as photolithography, imprint lithogrpahy, dip-pen lithography, and micro-contact printing to reduce the sensor linewidth.[124-126]

X-ray Excited Optical Luminescent Spectral Rulers

As an alternate method to fluorescence measurements, which suffer from interference by tissue autoflourescence backgrounds, we prepared low-background x-ray excited optical luminescent (XEOL) spectral rulers. When irradiated by an x-ray beam, x-ray scintillators generate visible light, and an indicator dye is used to modulate the spectral signal. We selected rare earth oxysulfide particles as the scintillators because they have large x-ray to visible light conversion efficiencies (~15% by energy), low

cytotoxicity (studies have shown that the LD_{50} for intravenous injection for rare earth scintillators doped with Gd^{3+} and Eu^{3+} is 10 – 100 mg/kg), and are chemically stable.[127] Although particles are generally less toxic than free ions, the sensors will be protected from bodily fluids by encapsulating in polydimethylsiloxane (PDMS), a biocompatible polymer. We have found that Gd_2O_2S particles encapsulated in PDMS and immersed in a 1M solution of H_2SO_4 were not dissolved after a period of 5 days.[128]

Our group has previously demonstrated the utility of XEOL by measuring the modulation of a luminescenct Gd_2O_2S:Tb particle film signal through methyl red dyed pH paper. Additionally, we have shown that Gd_2O_2S:Eu emission signals can be modulated by altering the pH of bromocresol green dye for pH sensing/infection detection on the surface of medically implanted devices.[62, 64] Analogous to the XEOL spectral ruler described here, spectral ratios of the emission peaks were calculated as the luminescent signal from the scintillators was passed through a dye layer.[62] We have also demostrated that the dissolution of silver particles deposited onto a scinitillator particle film can be monitored through 1 cm of porcine tissue.[63]

For our XEOL experiments, we patterned the encoder with a dye that absorbs red light. The dye patterned encoder is attached to a luminescent particle film below that serves as a light source for the sensor. The light emitted by the phosphors is absorbed by the encoder in a position dependent manner **(figure 2.5)**. As our model system, we have selected bromocresol purple and Gd_2O_2S microparticles doped with Eu^{3+}; the emission spectrum of the microparticles with overlapping dye extinction spectrum is shown in **(figure 2.6a)**. Upon x-ray excitation of the phosphors, the bromocresol purple dye

selectively absorbs the 625 nm particle emission peak more strongly than the emission at 700 nm. By varying the percentage of dye visible through the analyzer mask (0 - 100 %), the intensity of the 625 nm peak can be modulated while the emission at 700 nm remains essentially constant. The simulation in **(figure 2.6b-c)** demonstrates this principle; the luminescence for 10 different encoder positions was calculated. Each position corresponds to a 100 micron displacement for an encoder patterned with 1 mm wide bromocresol purple lines. As the percentage of dye uncovered by the mask is increased, the 625 nm peak emission intensity is drastically decreased. In order to relate the luminescent signal to displacement, a ratio of the signal intensity at 625/ 700 nm (I_{625}/I_{700}) was calculated and a calibration curve constructed.

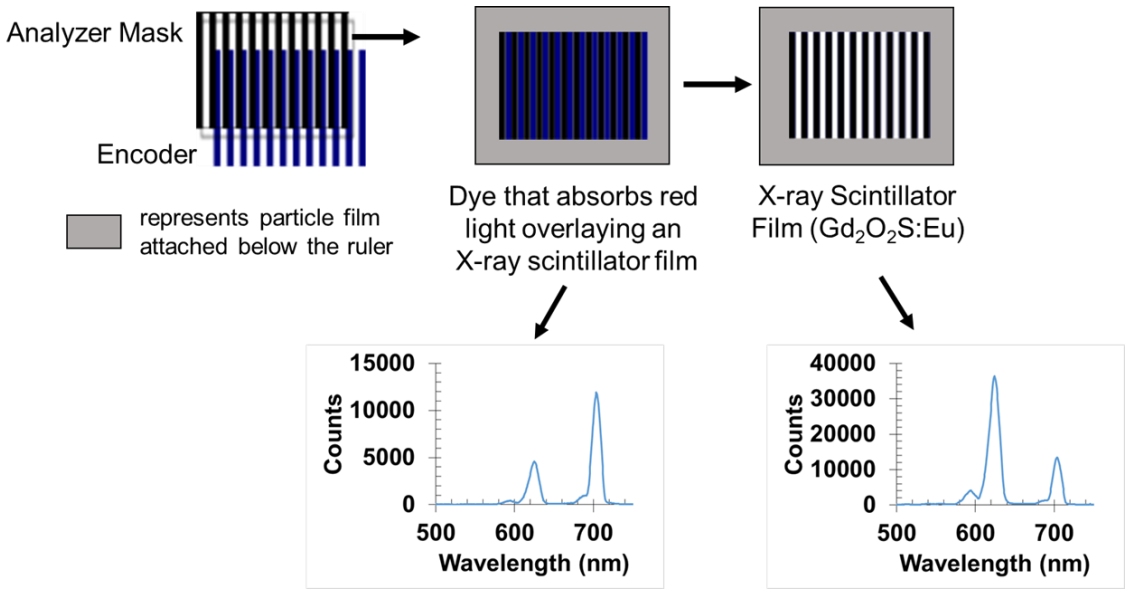

Figure 2.5 Schematic of an XEOL sensor encoder attached to an x-ray scintillator film with an overlaid analyzer mask. Relative motion of the components results in a spectral shift as shown. When dye is primarily viewed through the transparent spaces of the mask,

the 625 nm peak is partially absorbed. The signal at 625 nm increases when the nanoparticle film is viewed while the emission at 700 nm remains constant due to low absorption by the dye in this spectral region.

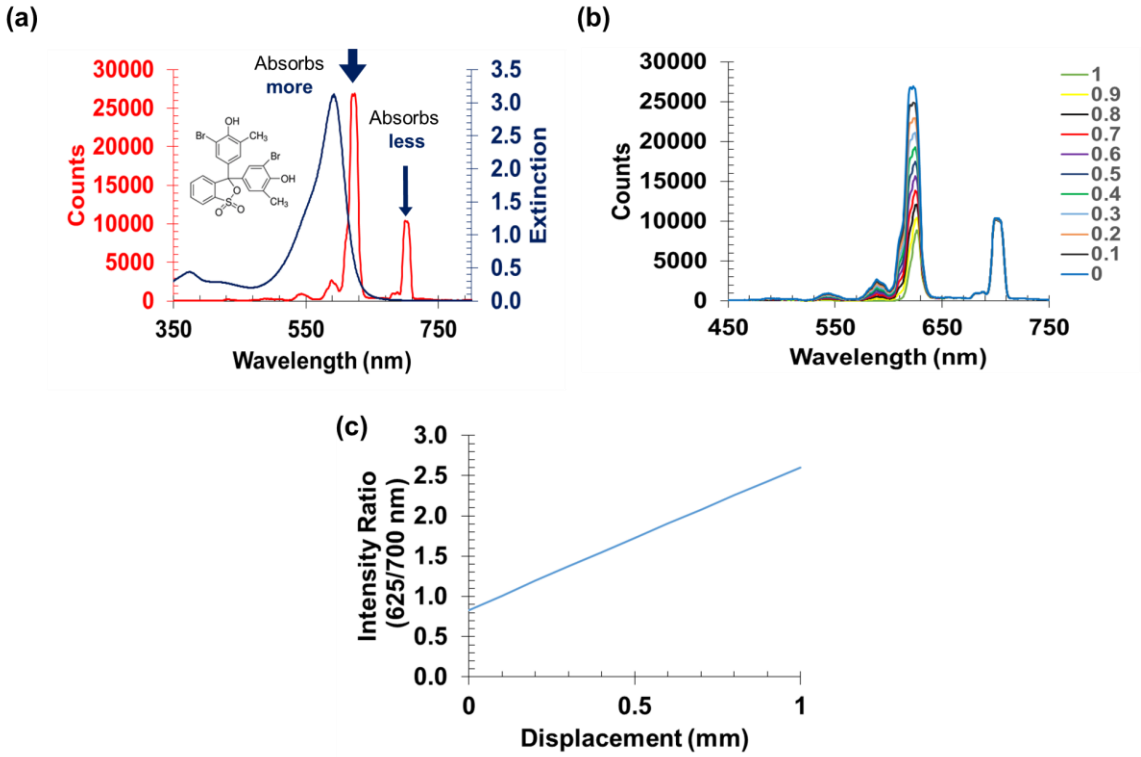

Figure 2.6 (a) Emission spectrum of Gd_2O_2S:Eu microparticles under x-ray excitation with overlaid extinction spectrum of bromocresol purple dye (pH 10). (b) Simulation of the spectral shift expected as the ruler is transitioned from 0 to 100 % dye visible through the mask. (c) represents the calculated intensity ratios (I_{625}/I_{700}) for the simulated data.

XEOL sensors patterned with 800 micron wide bromocresol purple dye lines and a 1.2 mm space between each were prepared by inkjet printing. The analyzer mask was printed on transparency with 1 mm apertures; dye lines on the encoder were printed

thinner than these apertures due to ink spreading in the cellulose substrate. Luminescent measurements in the presence and absence of tissue are displayed in **(figure 2.7a -d)**. Similar to the fluorescent measurements, a unique spectral ratio was measured for each 50 micron stage displacement. However, dissimilar to the fluorescent ruler, there is essentially no background from the tissue, as seen in **(figure 2.7d)**. A reproducible displacement of 14.5 microns was measured in the absence and presence of 6 mm thick chicken breast with a noise level of ~ 0.79 µm and 1.5 µm respectively. The percentage noise calculated for spectral ratios through tissue (0.35 %) agrees reasonably well with the expected shot noise of (0.32 %), as does the observed noise level in the absence of tissue (0.17 % with an expected percentage shot noise of 0.16 %). In the absence of stage motion, the noise level was 0.28 % through tissue and 0.18 % in the absence of tissue, corresponding to an error in displacement of 1.2 µm and 0.66 µm respectively. The read noise specifications for the detector operating at 33 kHz is 8 photoelectrons per pixel; I_1 and I_2 for XEOL measurements were an average of 35 pixels. The read noise for binning 35 pixels is equivalent to ~ 47 photoelectrons (the square root of 35 multiplied by 8 photoelectrons) and is small in comparison with the shot noise.

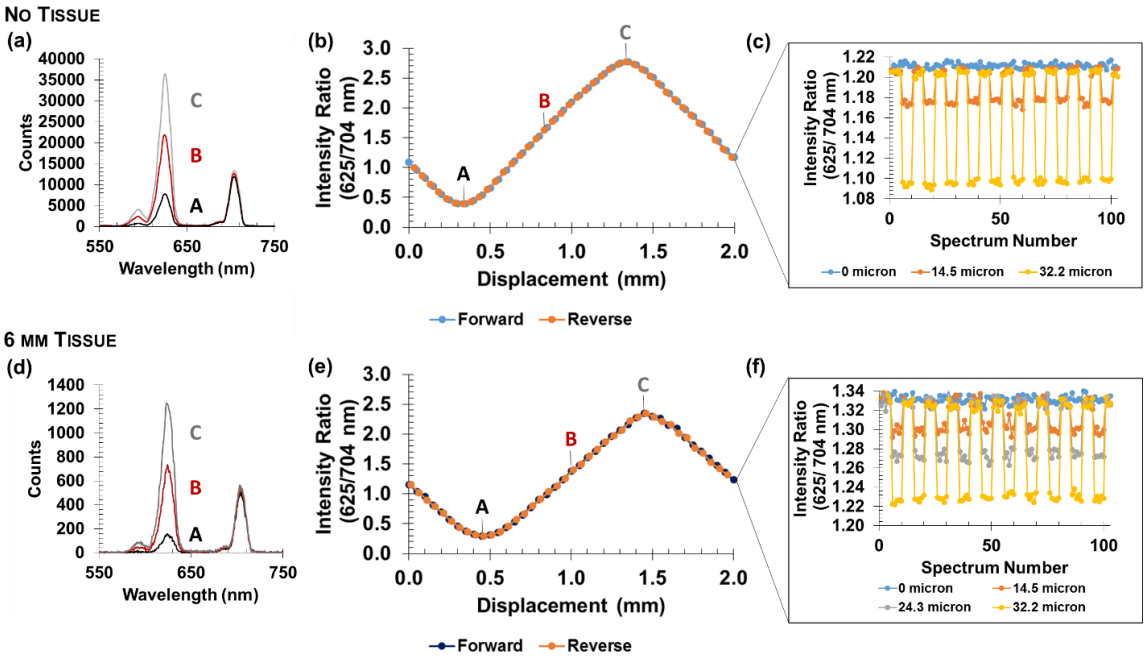

Figure 2.7 (a) and (d) show x-ray excited optical luminescence spectra at 3 different stage positions in the absence of tissue and through 6 mm thick chicken breast tissue respectively. (b) and (e) show the luminescence intensity ratio (625 / 704 nm) vs. displacement of the motorized stage. The stage was advanced in 50 micron increments until a maximum displacement of 2.0 mm was reached. The direction of the stage was then reversed and the displacements repeated in the opposite direction. (c) and (f) show reproducible measurements for small displacements in the forward and reverse directions. A reproducible 14.5 micron change can be detected through 6 mm of tissue. All Displacements were corrected for backlash of the motorized stage.

As with the fluorescent ruler, the addition of a spectral reference region can be incorporated to assess tissue effects; however, measurements in the presence and absence of tissue are in good agreement. In our previous work using XEOL through porcine tissue

to determine pH on implant surfaces, we effectively demonstrated the use of an *in situ* reference to account for tissue absorbing more strongly at 620 nm than at 700 nm.[62] Additionally, although we have selected to use only one particle type (Gd_2O_2S:Eu) for our measurement, we could also employ the use of 2 distinct scintillators (Gd_2O_2S:Eu and Gd_2O_2S:Tb) and prepare our sensor in the same manner as the fluorescent counterpart. This would allow for the ratio of two more closely spaced peaks to be calculated to ensure there is minimal spectral distortion.

As a demonstration of the intended sensor application, to measure tibial strain, an x-ray excited optical luminescent ruler was attached across the interfragmentary gap (~8 mm) of a fractured tibia mimic. The intact tibia mimic (Sawbones, Vashon Island, Washington, USA) for biomechanical testing has equivalent mechanical properties to human bone. The tibia mimic was loaded using a materials testing instrument to demonstrate the functionality of the sensor and reproducibility during a loading and unloading cycle. Spectral ratios were monitored as a function of applied load; **figure 2.8c** displays the resulting ratios from measurements acquired through 6 mm thick tissue. Variation in spectral ratios from sensor calibration **(figure 2.7)** was observed and can be attributed to a change in the collection system. The collection system was changed to allow for portability and to mimic a system appropriate for use in a clinical setting. Further characterization of the sensor including sensor calibration with the portable collection system will be performed in future studies.

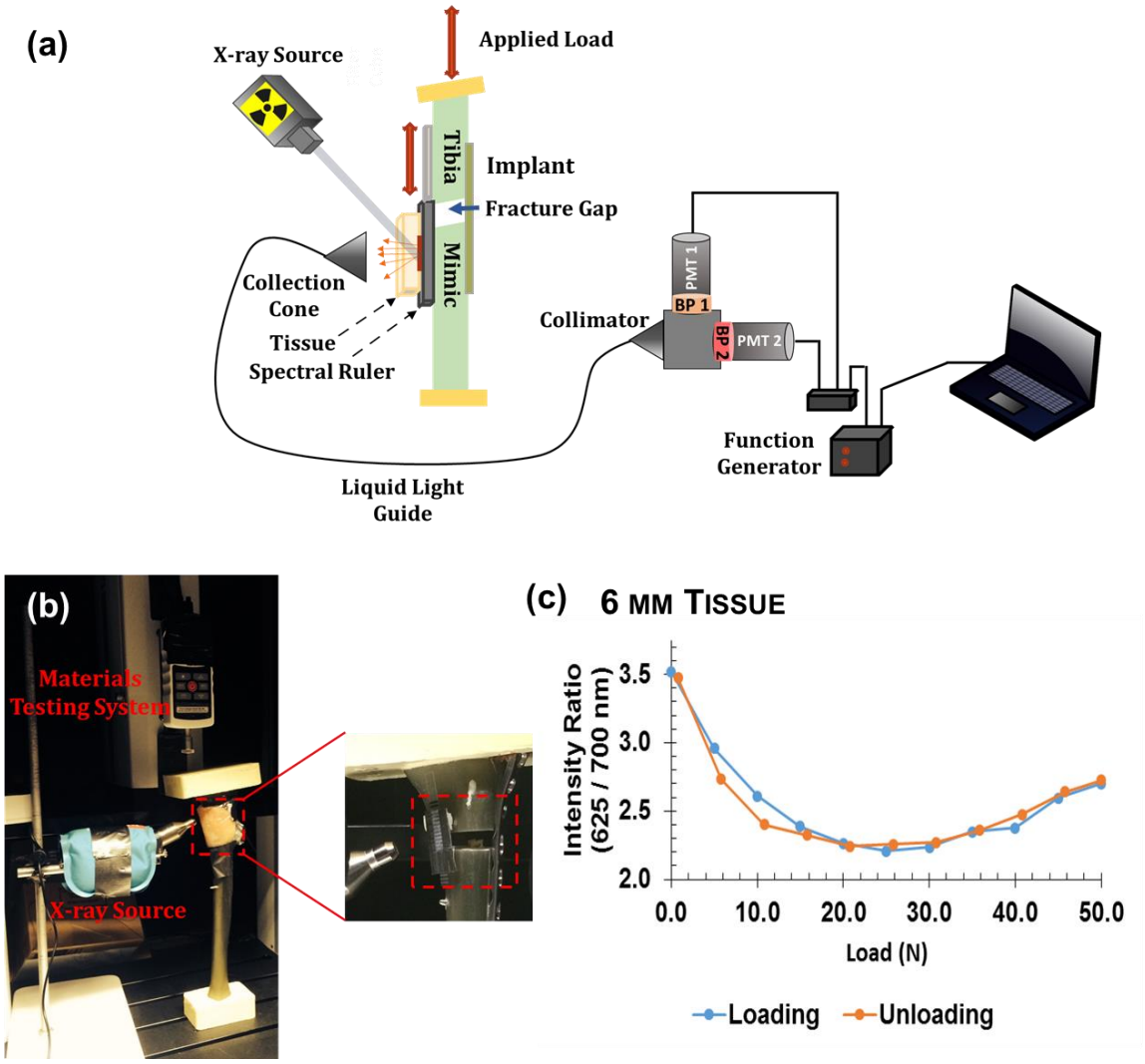

Figure 2.8 (a) Schematic of the experimental set-up for mechanical testing showing the portable collection system used to collect luminescence data. (b) Photograph of an x-ray excited optical luminescent spectral ruler attached across the interfragmentary gap (8.0 mm) of a tibia mimic. The sensor was overlaid with a piece of 6 mm thick chicken breast tissue and the tibia mimic was positioned under a materials testing system. Upon load application, the sensor was excited with an x-ray and signal collected with photomultiplier tubes (not shown in image). (b) Spectral ratio vs applied load is shown

for a loading cycle followed by an unloading cycle demonstrating the utility of the sensor to measure strain.

For the mechanical testing, the signal was collected by 2 photomultiplier tubes simultaneously at 625 nm (90 nm GMBW) and 708 nm (75 nm GMBW) after emission was passed through a 50/50 beam splitter and 2 bandpass filters providing an easily positioned collection system with high collection efficiency. A schematic of the experimental set-up is provided in **figure 2.8a**. Spectral ratios were calculated over a much narrower wavelength range (~ 20 nm) for calibration curves generated using the microscope collection optics. **Figure 2.8** shows a typical XEOL emission spectrum for the sensor overlaid with transmission data provided on the Semrock company website for each bandpass filter.[129]

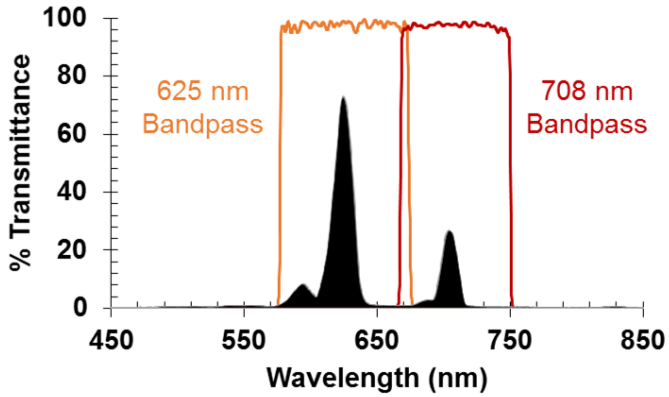

Figure 2.9 Emission spectrum of a Gd_2O_2S:Eu film (shaded in black). Overlaid regions show the bandwidth of the emission filters used in conjunction with the photomultiplier tubes for luminescent measurements associated with the mechanical testing experiments.

The 625 nm filter has a 90 nm bandwidth and the filter with a collection maximum located at 708 nm has a bandwidth of 75 nm.

2.4 Conclusions and Future Work

We have demonstrated a non-invasive method for determining position through tissue with fluorescent and XEOL spectral rulers. Our approach has successfully measured micron scale displacements based upon position-dependent luminescence. The approach is remarkable as it does not require micron scale features to be resolved through tissue (overcoming scattering limitations often associated with through tissue measurements). Micron scale displacements are monitored as a result of color change (spectral ratios). Additionally, the sensors are thin and flexible, measurements can be acquired by non-invasive means, and the sensor read-out can be easily interpreted. In comparison with existing spectral ruler technologies, our sensor provides the advantage of measuring displacements greater than the nanometer scale. The sensor linewidth can be tuned to accommodate a variation of displacement ranges or can be modified to contain a secondary measurement scale (similar to a Vernier scale).

Utilizing our fluorescent sensors patterned with quantum dots, we have measured 24.3 ± 0.5 μm displacements and 14.5 ± 0.7 μm displacements with a bromocresol purple patterned encoder overlaid on an x-ray scintillator film. These through tissue (6 mm thickness) measurements along with the preliminary demonstration of mechanical testing on a tibia mimic suggest that this technique will be promising for *in vivo* measurements on an implanted fixation device.

Future work will include improvement of the sensor design to incorporate a more rigid enclosure to ensure uniaxial displacement when implanted on an orthopedic device. Although, our current design has provided adequate motion restriction thus far, proper pattern alignment is critical for obtaining accurate displacement measurements. With the use of biocompatible 3D printable polymers, we can manufacture a rigid enclosure for our rulers.

Additionally, fabrication of spectral rulers that utilize non-ionizing radiation for excitation, 980 nm light, and have a very low background emission with both excitation and emission within the near-IR spectral region will be performed. Our approach will be analogous to our XEOL sensor but will utilize upconverting particles. Upconversion particles excited with infrared light exhibit sharp emission lines (1 – 20 nm FWHM) in the visible light/ near IR region from f-f orbital transitions, exhibit low cytotoxicity, and have long lifetimes and high photostability making them excellent candidates for spectral ruler fabrication.[67, 71, 130-131] Our group has demonstrated that luminescence from a pH sensor fabricated with a Y_2O_2S: Yb^{3+}, Er^{3+} upconversion nanoparticle film layer can be detected through porcine tissue ranging from 0 to 7 mm in thickness, suggesting the feasibility of fabricating a similar sensor that functions as a spectral ruler through tissue.[128]

CHAPTER THREE

UPCONVERSION SPECTRAL RULERS

3.1 Introduction

Measuring micron scale displacements is a challenging feat when collecting measurements through absorbing/ scattering media including biological tissues. However, these measurements may reveal pertinent information to clinicians regarding bone/tendon healing processes or may serve as an indication of failure of implanted medical devices.

Displacements of this nature have been assessed through tissue using tantalum beads or markers. Relative position between implanted beads and bone or implanted medical devices are measured by position tracking with a series of radiographs (Roentgen Stereo Analysis).[132-135] This method has been used routinely to explore the kinematics of knee-joints [132-136] and to study tendon healing.[137-138] For example, Schepull et al. have measured Achilles tendon strain in an experimental test group (10 patients) at various time points after rupture repair (6 weeks to 1 year). RSA measurements were recorded after loading the tendon with a 25 -200 N load during the first 18 weeks of healing. A decrease in tendon strain was observed as the healing process progressed; however, their results showed a large standard deviation that the author's attribute to patient dependent biological variations.[139] Although RSA is successful, it has limited use because it requires ionizing radiation to collect x-ray radiographs, is unable to collect measurements during normal motion/activities, and requires marker implantation which has proven challenging in soft tissue/tendon studies.[137] Alternatively, displacement measurements through tissue may be acquired using goniometers, computed tomography, fiber optic sensors, or

ultrasound. Ultrasound provides non-invasive measurement, tracking endogenous anatomical structures rather than implanted beads or markers.[140-142] Although these advantages are attractive, further studies investigating measurement accuracy must be conducted for *in vivo* trials.[142-143]

Generally, measuring displacement using an optical approach is advantageous because the measurements can be performed non-invasively. However, mapping or imaging of a surface with micron sized features becomes challenging when the tissue thickness is greater than ~ 1 mm in depth.[57, 113-114] To overcome this limitation, we have developed an approach for measuring micron scale displacements by collecting position-dependent luminescent signals. Using our methodology small features do not need to be resolved, rather position can be correlated with a change in color/ wavelength of light emitted by a sensor film. The technique offers the advantage of non-invasive measurements, simplicity in data processing and interpretation of the signal read-out, and the ability to measure position changes that would normally be un-resolvable as a result of optical scattering limitations. Our approach also eliminates the need for an ionizing radiation source.

The sensors described within this work have tremendous potential to assess biomechanical strain in the human body as we have demonstrated their ability to measure micron scale displacements through tissue. As a target, we have developed sensors to monitor ligament and tendon strain. We have selected this target because there is a high prevalence of tendon injuries in the sports industry and among the aging population. These injuries include rotator cuff tears, Achilles tendon tears and ruptures, and anterior

cruciate ligament (ACL) injuries. Although these injuries are common, with more than half the population over 60 years in age experiencing a rotator cuff injury and approximately 47 out of every 100,000 males between the ages of 10 and 19 requiring an ACL surgery each year, direct measurement of the mechanical properties of tendon and ligaments remain elusive.[137, 144-145]

There is a need for clinicians to better understand strain on tendons and ligaments not only to assess healing processes and aid in the development of treatment methods and therapies for such injuries, but also as a preventative tool against these injuries.[137, 146] Similar to the work presented in chapter 2, attachment of spectral rulers to their surface may provide a measure of when a patient may begin safe-weight bearing during the healing process. This will aid in prevention of pre-mature weight bearing, which can lead to re-injury, or extended recovery periods where motion of the area surrounding the healing tendon/ligament is restricted.

Tendon strain is challenging to monitor *in vivo* in part because of location, either the sensor may obstruct the function of the ligament/tendon, surrounding tissue and bone may press against the sensor leading to false readings, or the ligament/tendon is not in an easily accessible region.[146-147] Additionally, the strain distribution varies with position and some studies have shown that using currently available sensors and techniques the measurements were affected by loading rate and sensor rotation.[137] For ACL injuries it is common to predict forces acting on the ligament with mathematical computations.[137, 146] This approach requires the scientist to make assumptions when carrying out the mathematical model. With our sensor, we will be able to monitor the local strain and with

miniaturization of the sensor there should be little to no interference with surrounding tissue. Implantation of a series of miniaturized sensors could reveal the strain distribution along the length of the healing tendon/ligament.

Strain measurements have been performed on cadavers and excised tendons and ligaments to try and gain an understanding of their mechanical function. Pichorim et al. have measured strain in excised pig tendons by injection of an LC circuit containing a capacitor, an inductive transducer, and a mobile ferrite core housed within a silicon rubber tube. The tube contained Ni-Cr barbs to anchor the sensor to the tendon after insertion with a hypodermic needle. Using this innovative methodology, the authors were able to generate a stress strain curve and determine Young's modulus. This technique is advantageous due to the small size of the sensor, ease of insertion, and the ability to record measurements without the use of percutaneous wires. However, *in vivo* measuring ability has not yet been assessed.[148]

Tendon strain has also been monitored *in vivo* with the use of buckle transducers,[149-150] liquid metal strain gauges,[151] force and pressure transducers,[152-155] and fiber optic sensors.[138] Differential variable reluctance transducers (DVRT) have been used to measure forces acting on the ACL because of their small size and ease of calibration. These transducers have a measurement range of 1.75 mm and exhibit an error of 0.1 % strain.[146] These sensors are not realistic for long-time use because they require that the knee remains in a bent position; complete straightening of the leg causes the transducer to come into contact with the intercondylar notch. While buckle transducers

reduces error associated with non-uniform loading because they extend along the entire tendon cross section, they are bulky.[146]

Measurements of tendon strain have been demonstrated in *in vivo* animal models, including a study by Meyer et al. for the measurement of strain on the infraspinatus tendon, located in shoulder of Swiss Alpine sheep. Strain was measured daily during a two week long experiment using a flexion-sensitive force transducer. Although this sensor was able to measure strain *in vivo*, the sensor required connection to external measurement devices (including a signal amplifier and power source) with wiring through the neck of the sheep. Introduction of percutaneous connections may lead to an increase in probability of infection. Additionally, the mode of sensor connection to the tendon using sutures limited the operating range of the strain measuring device.[147]

Tendon measurements have also been conducted in human trials. Pourcelot et al. have reported a study measuring *in vivo* tendon strain in a 40 year old male test subject using an ultrasonic wave propagation sensor device. In this device signal velocity is measured between a series of transducers and correlated with applied load.[156]

Herein, we show proof-of concept for our sensor design and discuss reproducibility of sensor readout, controlled by the mode of spectral acquisition and functionality of the motorized stage.

3.2 Materials and Methods

Chemicals and Materials

Gadolinium oxysulfide upconversion phosphors doped with Ytterbium and Erbium (4.0 micron PTIR660/F) were purchased from Phosphor Technology Ltd. Sensors were coated with polydimethylsiloxane prepared from a Dow Corning Sylgard 184® silicone elastomer kit. Bromocresol green dye (Alfa Aesar), reagent alcohol (BDH), dibasic sodium phosphate/ monobasic potassium phosphate (BDH) buffer (pH 8) were purchased from VWR. Boise Aspen® 300 92 bright copy paper (Boise Paper Holdings, L.L.C, Boise, ID, USA) was used for sensor fabrication and 3 and 5 mil Fellowes laminating pouches (Enhance 3 mil photo card size laminating pouch and 5 mil business card size thermal laminating pouch, Fellowes, Itasca, IL) were used to create the sensor housing. Multi-purpose transparency sheets were purchased from Staples (Product number 23240, Staples, Framingham, MA). Bandpass filters were purchased from Semrock and a 50/50 beam splitter was purchased from Chroma Technology.

Synthetic ligaments, Trevira (Kosa) artificial edge ligaments, were provided as a gift from Edge Medical Biologics (Manchester, UK).

Sensor Fabrication

Spectral encoders were designed in Inkscape, a freeware graphics program to contain 800 micron wide dye stripes with a 1.2 mm wide space between each. Bromocresol green was prepared at a concentration of 1.1 mg/ml in a 50/50 solution of pH 8 buffer (sodium and potassium phosphate) and reagent alcohol. The dye solution was

added to a refillable ink cartridge and inserted into an Epson stylus R200 printer. For experiments performed using the collection optics of a fluorescent microscope, bromocresol green patterns were inkjet printed onto copy paper using the CD tray insert. All patterns were printed a series of 9 times over the original pattern in order to increase the amount of dye transferred to the paper. Sensors were cut using a Graphtec CE6000 desktop cutter (Graphtec Irvine, CA, USA) to a sensor size of 15 X 60 mm. The sensor housing was constructed from 5 mil laminating pouches using a Fellowes laminator (Venus 125, Fellowes, Itasca, IL) on the 4 mil heat setting. The analyzer mask pattern was designed in Inkscape to contain 1 mm wide opaque stripes with a 1 mm wide space between each. The analyzer was printed on the smooth (non-polymer coated) side of a Staples transparency sheet using an HP colorlaserjet 1518ni printer in black ink. The opaque stripes were printed 200 microns wider than the dye stripes on the encoder to accommodate for the ink spreading observed on paper substrates with the inkjet printer. The sensor housing was attached using double sided tape to an upconversion microparticle film prepared on a foil sheet. The film dimensions were 25 x 5 mm and contained 260 µl of a PTIR660/F solution (0.17 g/ml PTIR660/F in an aqueous solution containing 5 mg/ml carboxymethyl cellulose sodium). The particle film was prepared by drop-coating and was allowed to dry at room temperature overnight.

For samples with luminescence measured using photomultiplier tubes, the sample preparation was modified. An interdigitated sensor pattern was designed in Inkscape containing interlocking 950 micron wide stripes. In place of copy paper, a block of bromocresol green was printed onto a transparency sheet using the CD tray insert. The

block was printed over an additional 9 times. The interdigitated design was cut from the dye printed transparency as well as a from a blank transparency sheet. A blank and a dye containing sensor half was fit together and laminated inside a 3 mil laminating pouch. The sensors dimensions were then cut to 12.4 mm x 21.02 mm, double-sided tape was attached to one side, and the encoder was fit inside an empty encoder housing prepared from a 5 mil laminating pouch. The analyzer mask was printed with an HP colorlaserjet 1518ni printer to contain alternating black dye and transparent spaces of equal width (950 microns). The sensor was overlaid upon a 6 mm x 18 mm upconversion particle film containing 250 µl of 0.72 mg/ml PTIR 660/F in an aqueous solution containing 5 mg/ml carboxymethyl cellulose sodium

Luminescent Measurements

For all luminescent measurements, the spectral encoder housing was clamped to a mechanical stage with a machined fixture prepared to fit an MTS 50-Z8 stage. The analyzer mask was fixed at both ends to maintain the substrate in a stationary position (see **figure 3.2**). The backlash correction of the software program, ThorLabs APT user, was 0.05 mm. The functionality and reproducible motion of the stage was previously characterized. Briefly, the backlash for 25, 35, 50, and 100 micron displacements was determined to be 10.5 ± 0.7 µm, 10.7 ± 0.5 µm, 17.8 ± 0.9 µm, and 18.7 ± 0.8 µm respectively. Displacements were adjusted accordingly for changes in stage direction.

For luminescent measurements for sensors prepared on copy paper, the mechanical stage was inverted and placed over a 10 x microscope objective of an

inverted fluorescence microscope (DMI 5000, Leica Microsystems, Germany). A 3 mil laminating pouch was placed between the sensor and the microscope objective. The sensor was positioned above the collection optics and the objective height set to 8.60 mm (the minimum distance allowable between the objective lens and sample plane). The spectral ruler was excited from below with a 500 mW 980 nm laser (Changchun New Industries Optoelectronics Technology, Changchun, China) after the laser emission was filtered through a 980/15 nm bandpass filter (Chroma Technology Corp, Bellows Falls, VT). Sensor luminescence was passed through a 960 nm short pass emission filter (Chroma Technology Corp, Bellows Falls, VT) prior to being sent to a CCD camera (iDUS-20BV, Andor, South Windsor, CT, USA) in a DeltaNu spectrometer (DNS 300, DeltaNu, Laramie, WY). The efficiency of the light collection was improved with the addition of a cylindrical lens between the microscope and spectrometer. Spectra were collected with either a 150 line/mm grating centered at 600 nm or a 1,200 line/mm grating centered at a value of 1290. For the grating with finer spacing, the pixel number read-out of the spectrometer was calibrated using room light to convert the values into nanometers. Using Andor Solis software, the collection exposure time was set to 0.30 seconds for the 150 lines/mm grating and 0.050 seconds for the 1200 lines/mm grating. Spectra were recorded at a read-out rate of 100 kHz @ 16-bit corresponding to a signal output to photoelectron conversion of 15 photoelectrons per count.

Luminescence measurements were acquired using a portable collection system for the interdigitated sensors. The spectral ruler was attached to the motorized stage and placed on the reflective surface of a lab jack to adjust sensor height. An optical fiber with

attached lens was positioned to illuminate the spectral ruler from above with a portable 500 mW 980 nm laser filtered through a 980/15 nm bandpass filter (Chroma Technology Corp, Bellows Falls, VT). A collection lens was centered above the ruler and illuminated area. At the exit of the lens, a 3 ft long, 5 mm diameter liquid lightguide was attached to transfer the signal to a collimator at the entrance of a filter cube. The light was passed through an 842 nm short pass filter to ensure no bleedthrough from the laser (if not properly excluded by the 980 nm filter) would be collected and influence calculated spectral ratios. The light was then redirected by a 50/50 beam splitter and passed through either a 661/11 nm bandwith or 680/13 nm bandwidth emission filter. At the exit of each lens was a photomultiplier tube (Sens-Tech P30PC-01 Berkshire, UK) with a 25 mm collection area. Photon counting was performed using a USB-interfaced data acquisition device (model NI 9402 National Instruments, Austin, TX, USA). Spectral acquisition settings were controlled with a custom LabView program. The signal was acquired with a sampling frequency of 1 MHz and acquisition time of 100 milliseconds. In order to ensure the luminescent signal did not saturate the number of counts that could be processed by the data acquisition device, a sheet of white paper was placed between the sample and the excitation source and collection optics to reduce the signal. A total of 100 measurements were acquired at each stage position and the intensity read-outs were averaged for each location. The same motorized stage used for the microscope measurements was used for the portable set-up and controlled with ThorLabs APT software. Motorized stage step sizes were programmed to be either 100, 50, 35, or 25 microns. Backslash corrected measurements correspond to actual distances of 81.3 ± 0.8

μm, 32.2 ± 0.9 μm, 24.3 ± 0.5 μm, and 14.5 ± 0.7 μm respectively upon change in direction of stage motion. For luminescent measurements acquired through tissue, a 1.0 second exposure was used and the sample was placed below a 6 mm slice of chicken breast tissue wrapped in cling wrap. Spectral ratios (I_{661}/I_{680}) were calculated after subtraction of a background (dark counts of the collection system).

3.3 Results and Discussion

The sensors evaluate position by monitoring a luminescent signal generated from upconversion microparticles below an encoder strip. The encoder strip contains alternating lines printed with a dye that absorbs red light. The encoder is overlaid with a mask, referred to as the analyzer. The analyzer is a transparent film patterned with a black dye with line spacing equal to the lines on the encoder. The black dye does not transmit light produced by the microparticle film. Both the encoder and the analyzer's motion is confined to a single axis by entrapping the encoder strip inside a semi-rigid laminate pouch containing guiding rails that restrict the motion of the overlaid analyzer. **Figure 3.1a** depicts a schematic of the sensor design, showing the microparticle film below the housing of the encoder strip. A luminescent signal is generated by the sample when irradiated with a 980 nm laser, exciting the microparticle film. The luminescent signal passes through the encoder layer of the sensor before exiting through the analyzer mask and traveling to the detector (spectrometer). The signal output is modulated based on analyzer position; when the blackened regions of the analyzer overlay the dye on the encoder, the spectrum collected represents that of the upconversion microparticles.

Alternatively, when the dye region of the encoder is fully revealed through the analyzer, a portion of the luminescent signal from the upconversion particles is absorbed by the dye. Luminescence observed at three distinct alignments of the analyzer over the encoder strip are shown in **figure 3.1c** along with the absorbance profile of the dye overlaid upon the emission spectrum of the microparticle film (**figure 3.1b**). When the analyzer is in an intermediate position between the two extremes described, the spectrum observed is a linear combination of the start and end positions.

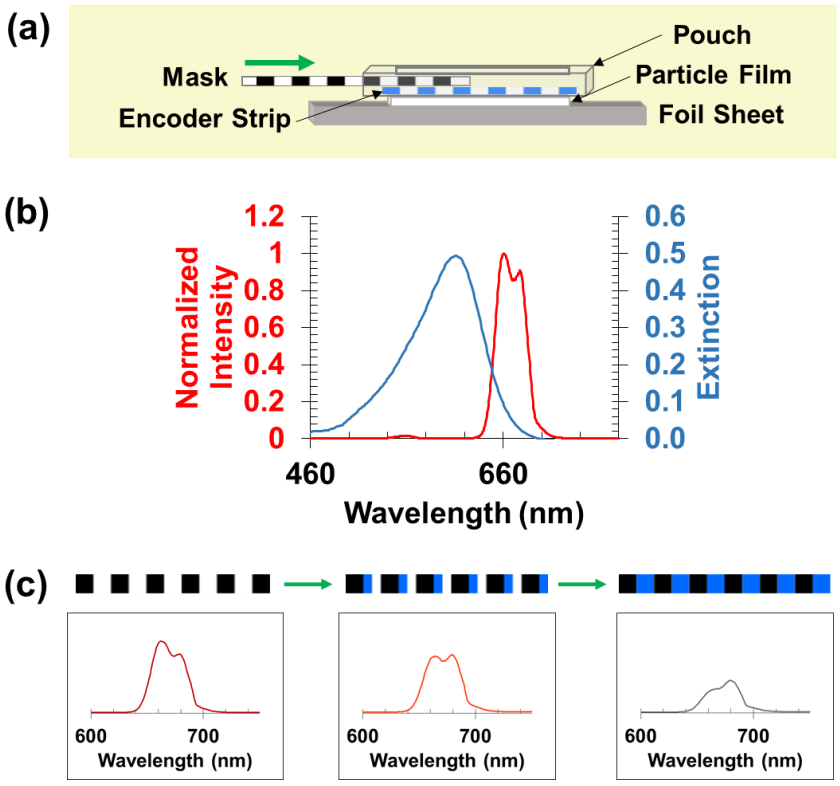

Figure 3.1 (a) Schematic of the spectral ruler sensor design showing assembly of the sensor inside a semi-rigid laminating pouch. The sensor assembly overlays an

upconversion microparticle film. (b) Absorbance spectrum of bromocresol green (pH 8) in solution overlaid upon the emission spectrum of a Gd_2O_2S:Yb, Er film excited with 980 nm light. (a) Three distinct positions of the encoder with respect to the analyzer mask are shown with their corresponding emission spectra. As the amount of dye revealed through the transparent windows of the analyzer is increased, the signal from the left side of the emission peak decreases relative to the right side of the emission peak.

For the rulers described within this work, the spectral encoder contains a series of bromocresol green lines with a 950 micron space between each. We have selected Gd_2O_2S:Yb, Er upconversion microparticles as the sensor excitation source and have fabricated a thin particle film coated with polydimethylsiloxane on a reflective foil sheet attached below the housing of the spectral encoder. Bromocresol green is a pH sensitive dye; at a basic pH, the absorbance spectrum of the dye has a sufficient overlap with the emission spectrum of the Gd_2O_2S:Yb, Er particles, as seen in **figure 3.1b**. The bromocresol green dye was prepared in a mixture of reagent alcohol and phosphate buffer (pH 8). At this pH value, when the microparticle film below the dye is excited, the BG dye will absorb more strongly the left side of the Gd_2O_2S:Yb, Er emission peak than the right. Since the luminescence from a single spectral peak is being monitored a spectral ratio can be calculated and correlated with position of the analyzer mask. For calibration purposes, we have attached our encoder housing to a motorized stage with the analyzer mask attached separately to the apparatus. The mask is clamped on either end and remains in a fixed position. An image of the sensor set-up is provided below in **figure**

3.2. Advancement of the motorized stage position is controlled electronically with ThorLabs APT software.

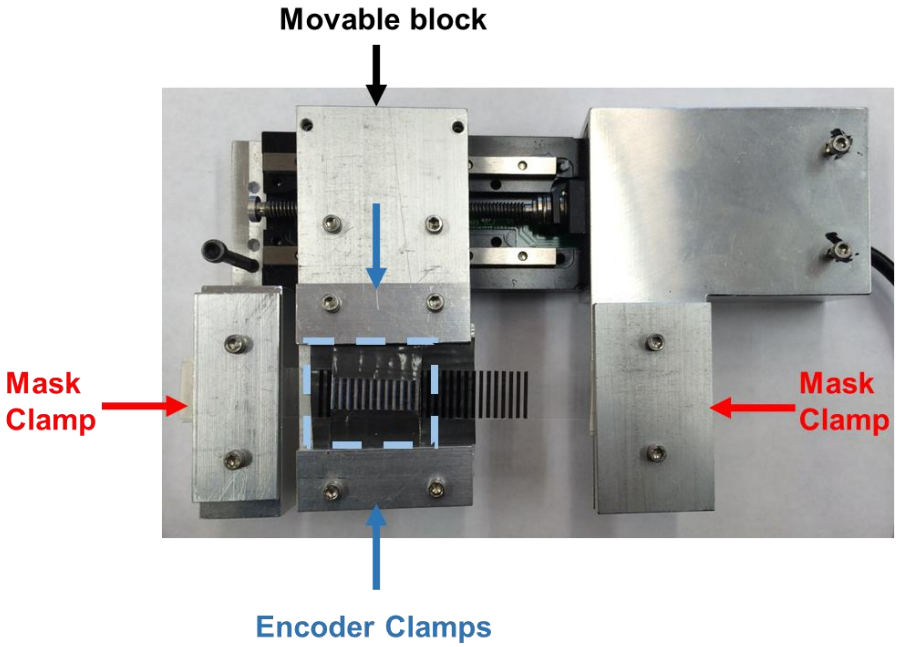

Figure 3.2 Photograph of an upconversion spectral ruler held by the motorized stage fixture. The analyzer mask is held in a fixed position, clamped on either end. The encoder and particle film are attached to a metal extension screwed into the movable portion of the motorized stage. The encoder is highlighted in the light blue dashed box.

Upconversion particles offer several advantages over conventional fluorescence approaches for generating a luminescent signal to be collected through tissue. Upconversion nanoparticles are typically excited with lasers with output in the infrared, such as 980 nm light. In the infrared, tissue scattering is reduced and long penetration depths can be achieved through tissue. This wavelength (980 nm) is optimal for tissue studies because the absorption coefficient of tissue is lower between ~ 650 nm and 1,000

nm; below 600 nm both hemoglobin and melanin have significant absorption and above 1,000 nm there is significant absorption due to water.[55, 78, 157-158] Additionally, this excitation wavelength results in less excitation of naturally occurring fluorophores within tissue (e.g. NADH has maximum light absorption at 340 nm and FAD at 450 nm with maximum emission at 460 nm and 525 nm respectively).[55] Other naturally occurring fluorophores include lipo-pigments which excite between 300 and 500 nm with emission between ~ 450 nm and ~ 650 nm and porphyrins that have an excitation maximum around 400 nm with emission in the 600 – 700 nm range.[55] Billinton et al. provide an extensive list of other naturally occurring fluorophores along with their excitation and emission maxima in a review discussing endogenous autofluorescence.[159] Most importantly, the upconversion signal has very low background because upconversion particles work by sequential absorption of excitation light which provides a much higher cross-section at the excitation powers used than fluorescent dyes, which require essentially simultaneous absorption of two photons.[160]

Previously we have demonstrated the concept of absorbance of luminescence from an Er^{3+} doped upconversion film by bromocresol green with the development of a pH sensor capable of effectively measuring pH between pH 5 and 10. At low pH values, there is minimal overlap of the dye absorbance with the particle emission peak above ~ 650 nm. Spectral ratios were calculated for emission intensities at 661 nm and 671 nm after excitation with 980 nm light. A power dependence study for the emission wavelengths revealed that ratios calculated from these closely spaced peaks would not be affected by laser intensity. With this study, luminescent signals were collected through ~

6 -7 mm of porcine tissue and pH monitored during the growth of *S. epidermidis* bacteria.[128]

We have also demonstrated a similar principle with spectral rulers patterned with bromocresol purple overlaying a Gd_2O_2S:Eu x-ray scintillator film and with an extension of the pH sensors described above.[62] With the XEOL version of the spectral ruler we demonstrated that 14.5 micron changes in position could be detected through a tissue depth of 6 mm. Signals were collected through chicken breast tissue and were shot noise limited.

Initial experiments involving our upconversion sensor were conducted on the stage of an inverted fluorescence microscope using a 10 x microscope objective to collect the luminescent signal, mimicking our results presented in the previous chapter for XEOL and fluorescent spectral rulers. With this set-up (**figure 3.3**), there is significant light loss resulting in a low collection efficiency as a result of the small collection angle of the microscope objective and the dimensions of the spectrometer slit width.

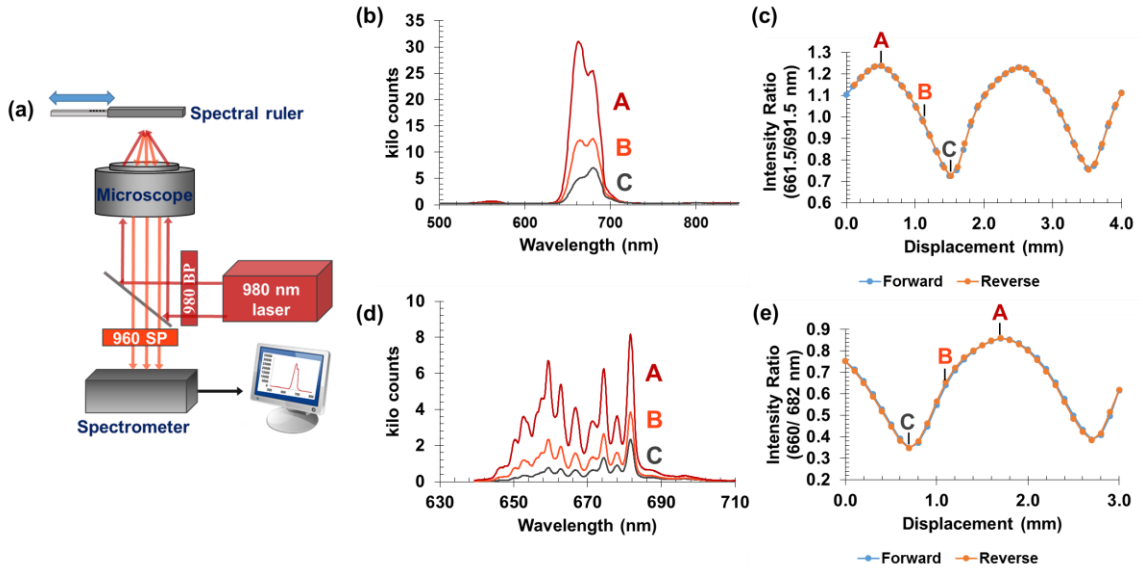

Figure 3.3 (a) Schematic of the experimental set-up. The spectral ruler is attached to a motorized stage and positioned above the collection optics (microscope objective). The sample is excited from below with a 980 nm laser and the luminescent signal generated is captured by a CCD camera. (b) and (d) show luminescent spectra acquired at three distinct positions of the encoder relative to the mask. Spectra in (b) were acquired with a spectrometer grating with 150 lines/mm and spectra in (d) using a grating with finer spacing (1200 lines/ mm). Spectral ratios corresponding to the selected spectra (A-C) are denoted in (c) and (e). (c) and (e) show calibration curves for the sensor as the spectral encoder transitions from position A (no BG showing through the mask) to C (maximum BG showing through the mask).

Experimental results from these measurements demonstrate proof of concept for the intended sensor. **Figure 3.3b** shows the luminescent signal acquired with a 0.30 s exposure and a spectrometer grating with a spacing of 150 lines per mm. The luminescent

spectral ratios were corrected for the inherent backlash of the motorized stage. Experimentally derived backlash corrections for various software input step sizes are provided in the experimental section. Details of the backlash characterization are provided in Appendix B. As expected, an increase in the amount of bromocresol green dye visible through the transparent windows of the analyzer mask resulted in a greater absorption of the luminescent signal at 661 nm in comparison with luminescence at ~ 691 nm (left to right side of the emission peak). We calculated spectral ratios for each unique encoder position; each data point represents a 100 micron displacement of the encoder. Finer spectral details were observed by repeating the calibration with a grating containing 1,200 grooves per mm. The spectra in **figure 3.3d** show the luminescent signal for the finer grating spacing and the calibration curve can be seen in **figure 3.3e**.

To improve collection efficiency of our instrumentation and make our system portable for use in a clinical setting, we used photomultiplier tubes in place of the microscope optics and CCD camera. The modified set-up also offers the advantages of being cheaper and simpler and provides the possibility for increased data collection speed. A schematic of the new collection system is provided in **figure 3.4**. No modifications were made to spectral ruler attachment to the mechanical stage (pictured in **figure 3.2**) and the operation of the computerized control software. The ruler was illuminated from above with a 980 nm laser and the microparticle emission was captured with a collection lens (focal length 40 mm ± 5 %, a numerical aperture of 0.554, and a lens diameter of 50 mm) before traveling through a 3 ft long liquid light guide (5 mm diameter) to a collimator attached to the entrance of a filter cube. The emission was first

passed through an 842 nm short pass filter to ensure no excitation light would reach the detectors. After passing through the short pass filter the emission was directed to a 50/50 beam splitter. Beyond the beam splitter were two separate band pass filters (emission maxima at 661 or 680 nm) and a photomultiplier tube for each.

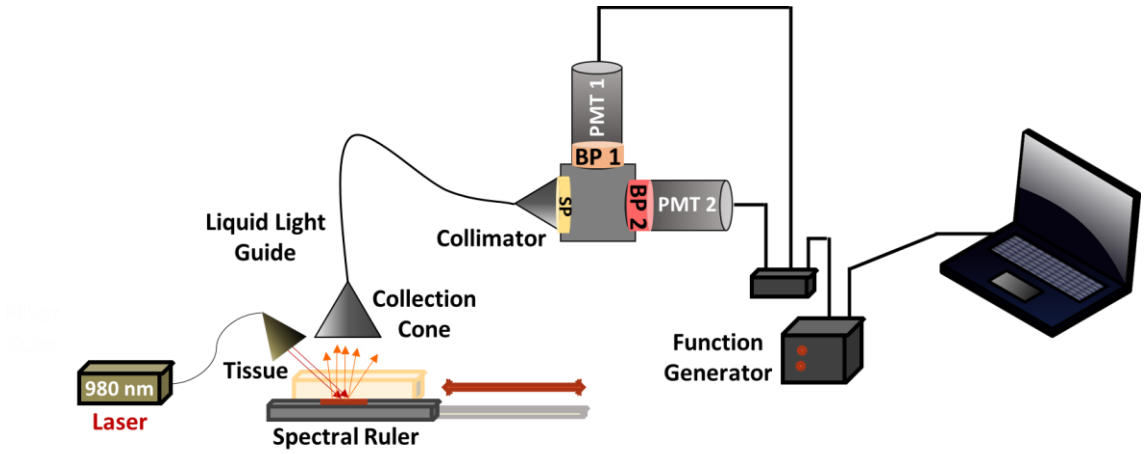

Figure 3.4 (a) Schematic of the experimental set-up showing the collection system (dual PMTs). The sensor is excited with 980 nm light and the emission is passed through an 842 nm short pass filter before passing through a 50/50 beam splitter housed within a filter cube. The light is then directed through either a 661 nm bandpass or 680 nm bandpass filter before reaching a PMT.

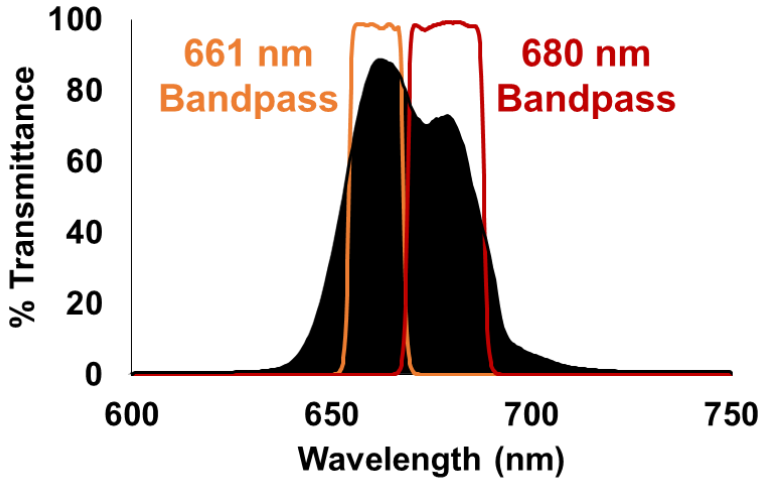

Figure 3.5 Emission spectrum of the sensor overlaid with transmission data provided by Semrock for each bandpass filter.[129] The 661 nm bandpass filter has a bandwidth of 11 nm and the 680 nm filter has a bandwidth of 13 nm.

Although we expected an increased collection efficiency with the photomultiplier tubes, we modified the sensor preparation in order to increase the low signal output we observed for measurements through tissue using the initial set-up. For the preliminary microscope experiments, the encoder strip was prepared on white copy paper with a thickness of ~ 100 microns. White paper is a highly scattering medium and therefore was replaced with a transparent film in order to decrease signal scattering and increase the amount of light detected. With paper as the encoder substrate coupled with the small collection angle of the microscope objective, it was challenging to achieve a sufficient signal through tissue. This modification was made for all sensors prepared for measurements using the PMT collection system reported here.

A calibration curve for sensor displacement in the absence of tissue was generated using the new collection system. Due to an intensified signal, white paper was placed on top of the spectral encoder so that the excitation source passed through the scattering medium as well as the resultant luminescence before the signal was detected. This set-up modification prevented saturation of the photon counting device. Each data point on the calibration curve represents the average of 100 spectra acquired at a single position. Average intensities vs. encoder position for each bandpass filter are provided in **figure 3.6** and the calibration curve for the corresponding measurements presented in **figure 3.7a**. Spectral ratios (I_{661}/I_{680}) were calculated from the average intensity values.

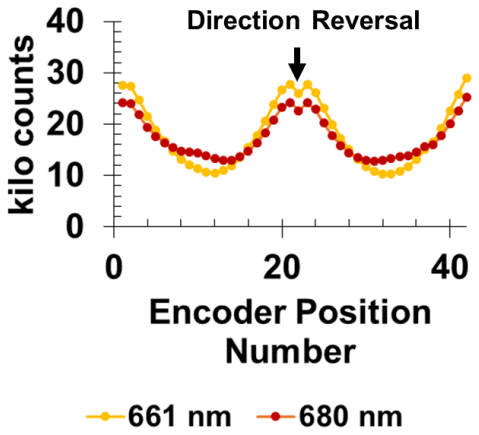

Figure 3.6 Average intensity vs. encoder position (a 100 micron encoder displacement was performed between each position). Each data point represents the average of 100 measurements. Direction of the motorized stage was reversed after 2.0 mm of travel.

As an extension of this study, we have demonstrated the sensor's ability to measure reproducible displacements on the tens of microns scale. Single forward and

reverse motions of the mechanical stage revealed that 14.5 micron displacements could be measured in the absence of tissue. Similar to the calibration curve, each data point represents the average of 100 measurements at that position. By averaging over 100 spectra for each data point we have reduced the shot noise by a factor of ~ 8 for this data set.

The average percentage error (shot noise) for all step sizes excluding 0 microns (no motion) was calculated to be 0.18 %. We converted the noise level on the signal to an error in displacement using the average difference in spectral ratio for a 32.2 micron displacement divided by the stage step size. A change in ratio of 9.93×10^{-4} at this stage position corresponds to a displacement change of 1 micron. For measurements acquired in the absence of motion (0 micron step size), the percentage error agreed with the average error for the three steps sizes reported, 0.18 %, and suggests the data is shot noise limited. There is negligible error in the stage/sensor position. This percentage error corresponds to a 1.69 micron error in displacement. Although, measurements for step sizes less than 14.5 microns were not attempted due to backlash limitations of the motorized stage, we expect that we can detect displacements of smaller magnitude based on our error calculations.

We repeated the calibration curve measurements through tissue; 6 mm of chicken breast tissue was placed above the sample. To ensure a significantly bright signal was acquired, we increased the exposure time from 100 milliseconds (in the absence of tissue) to 1.0 second. The calibration curve is in good agreement with our previous measurements in the absence of tissue. A single displacement study was performed

through tissue using the same programmed motorized stage step sizes as shown in **figure 3.7b**. Although, the signal intensity was decreased through tissue, we measured 14.5 micron displacements with low position error. The calculated noise associated with error in position was determined to be 0.73 microns when there was no stage displacement and an average of 2.0 microns for measurements acquired for the 14.5, 24.3, and 32.2 micron displacements. We attribute the increase in error to buckling of the analyzer mask and imprecision in motion of the encoder.

In addition to showing proof of principle for through tissue displacement measurements, we have also shown that we can monitor displacements at a less sensitive region of the calibration curve. The small displacement study was conducted at the steepest slope of the linear portion of the curve, while the through tissue measurements were collected close to a sensor position extreme (almost 100 % of the region below the transparent window containing bromocresol green dye).

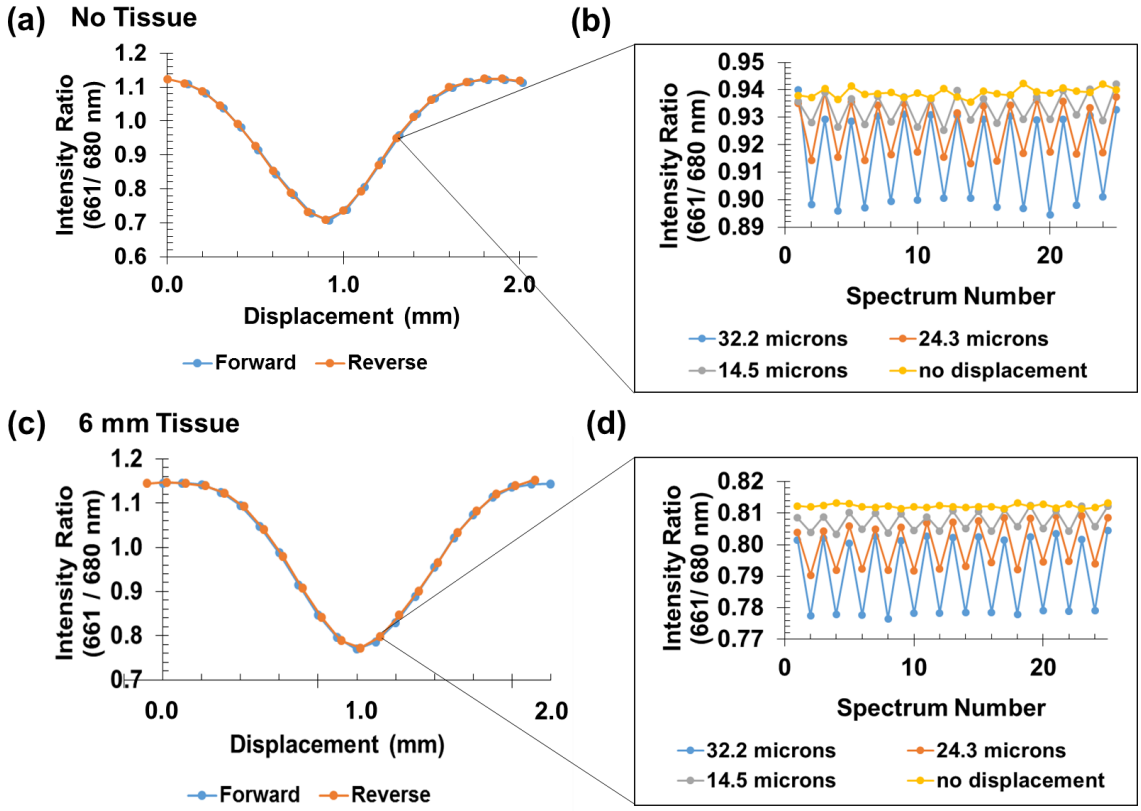

Figure 3.7 (a) and (c) show spectral ratio (I_{661}/ I_{680}) vs. sensor displacement for a travel distance of 2.0 mm. Each point represents a 100 micron displacement. (c) and (d) show reproducible spectral ratios for a single position (single forward displacement followed by a return to the initial position). All displacement measurements in (c) – (f) were corrected for backlash of the motorized stage.

Conclusions and Future Work

We have successfully demonstrated proof-of- concept for measuring reproducible micron scale displacements through tissue using a novel upconversion spectral ruler. The rulers provide a low noise, low background signal through tissue without the use of

ionizing radiation. We have measured displacements ranging from 100 microns down to 14.5 microns with signals limited primarily by shot noise and displacement step size limited by the backlash of the motorized stage. We expect that we can measure displacements as small as ~ 2.0 microns through tissue. By detecting a change in wavelength/ color, the method does not require small features to be resolved through a biological medium. We have also demonstrated the ability to collect measurements with a cheap, simple and portable collection system that would allow the technique to be performed in a clinical setting.

Future work will include miniaturization of the sensors to be applied in the measurement of strain on tendons/ligaments in animal models. We will approach the miniaturization by the use of photolithography or 3D printing with custom filaments prepared by our lab containing luminescent materials.

Along with sensor miniaturization, we will further our study by attaching the spectral ruler to a 10 mm wide cruciate ligament mimic. A photograph of the ligament with attached sensor is provided below, **figure 3.8**. The initial gauge length (distance between points of attachment) will be measured. We will apply known forces to elongate the ligament using a force testing system. The luminescent signal generated by the ruler will be collected at each force reading. We expect that we will be able to determine the amount of ligament elongation by monitoring the change in spectral ratio. This experiment will provide proof of concept for measuring forces acting on ligaments and tendons during the healing of sports related injuries.

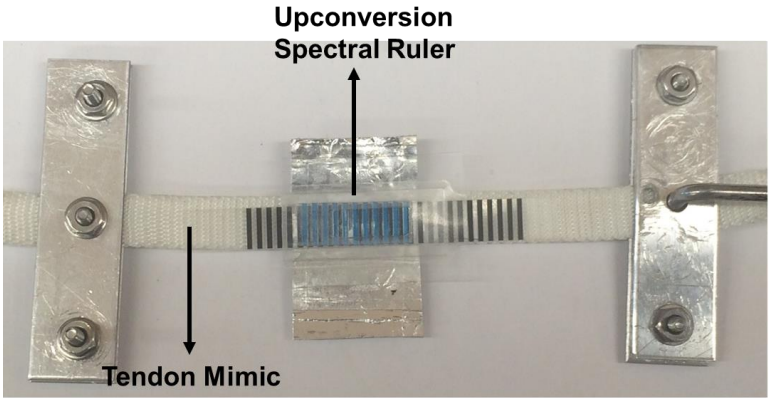

Figure 3.8 Photograph of an upconversion spectral ruler attached to a 10 mm wide cruciate ligament mimic.

CHAPTER FOUR

MAGNETICALLY MODULATED SENSORS FOR IN VIVO pH MONITORING

In chapters two and three we demonstrated the use of position-dependent luminescent sensors to measure displacement through tissue as a result of relative motion between the analyzer mask and encoder strip. Motion was controlled by attachment of the ruler to a motorized stage. Alternatively, position can be controlled by an external magnetic field. As a demonstration of magnetic modulation, we have attached our spectral ruler to a neoprene rubber strip containing magnetic material at one end. A secondary magnet was placed a set distance from the end of the magnetic strip. Motion of this magnet towards and away from the sensor resulted in a color change visible through the transparent windows as the rubber strip was stretched. Sensor images and a calibration curve are shown below in **figure 4.1**. Hysteresis between the forward and reverse measurements is a result of mechanical and magnetic effects. Hysteresis can be minimized by improvement of sensor design.

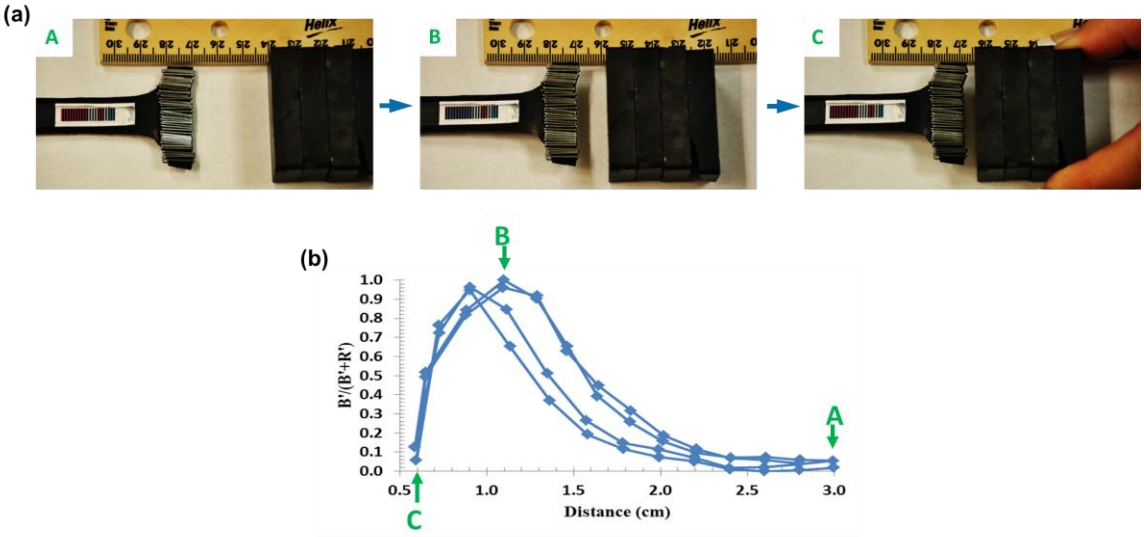

Figure 4.1 (a) Spectral ruler attached to a neoprene rubber strip containing iron staples stretched under magnetically applied forces. (b) Normalized color ratio (Blue/ (Blue +Red)) as a function of distance between the magnet and end of rubber strip modified with magnetic material. The position of the magnet was moved in 0.2 cm increments. The hysteresis can be attributed to a combination of both mechanical and magnetic effects.

Using the principle of magnetic modulation to control sensor position, we have developed a chemical sensor (pH) for conducting measurements through tissue. We have modified the sensor design to contain a single substrate with both a sensing region and mask for preliminary experiments. Details of the preliminary sensor and its application are provided in the chapter below.

4.1 Introduction

Fluorescene imaging and spectral analysis has widespread use in the biological community due to bright signals emitted from fluorophores, the availability and tunability of fluorophores to fit a wide array of experimental conditions, and the ability to acquire measurements with high sensitivity. When *in vivo* fluorescent signals from exogenous species are acquired through tissue, the signal collected is a combination of luminescence from exogeneous species and from endogeneous species within the tissue sample. These endogeneous species include flavins, amino acids, melanin, collagen, elastin, and NADH among others.[77, 159] The autofluorescence from these species is typically broad, ranging over several hundred nanometers. When the luminescence signal of the exogenous species is weak or has a strong overlap with the tissue autofluorescence, it is necessary to remove the background signal in order to increase the signal-to-noise ratio.

Several approaches to autofluorescence removal and experimental designs that minimize tissue autofluorescence have been cited throughout the literature including fluorescence time-gating, digital image processing, and mathematical algorithms such as principle components analysis.[159, 161-166] In simple cases, with the correct selection of the excitation source in combination with the use of emission filters, the autofluorescence signal may be blocked allowing for luminescence from the exogeneous species to be easily detected. Pushing the excitation into the near-infrared decreases absorption and scattering by the tissue and results in less tissue autofluorescence. In cases when it is difficult to separate the autofluorscence from the overlapping fluorophore signal or the origin of the autofluorescence is unknown, fluorescence time-gating can be used.

Fluorescence time-gating is an effective subtraction method when the fluorescent life-time of the exogenous species is greater than ~ 1 - 10 ns, the lifetime range of many naturally occuring fluorophores. In this instance, the signal from the exogenous species may be acquired after a delay period greater than 10 ns. The use of quantum dots, lanthanide chelates, and porous silicon nanoparticles for fluorescence gating has been demonstrated.[162-163, 167] Although successful, this methodology is limited in its utility because there are a limited number of biocompatible fluorophores that fit this criteria.[163] Removal of autofluorescence by the use of two excitation sources, one that excites both the exogenous and endogenous components and a secondary laser that excites only the endogenous species have been investigated. In this approach, collection of the two signals allows for background subtraction to be performed however, requires the availability of two closely spaced excitation lines. The shift in excitation wavelength must be minimal in order to ensure that the autofluorescence from the tissue from both lasers is comparable.[159, 164] Lastly, tissue autofluorscence may be removed post-measurement by mathematical algortihms or image correlation techniques.[165] Often these mathematical corrections require *a priori* knowledge of the tissue autofluorescence, which is not always readily available since autofluorescence varies by tissue type and is affected by the excitation source selected.

The Kopelman group at the University of Michigan has developed an innovative method for separating autofluorescence signals from desired sensor signals. The group has developed MagMOONs, **mag**netically **mo**dulated **o**ptical **n**anoprobes, a novel type of fluorescent sensor that is capable of background signal subtraction.[168-172] These sensors

consist of a nanoparticle loaded with a fluorescent dye and magnetic material. One hemisphere of the particles is coated with a metal such as aluminum. The purpose of the metallic coating is to block fluorescence excitation and emission from one half of the particle. The particles are magnetized in a single direction so that the particles will uniformly orient themselves in a rotaing magnetic field. When the direction of the external field is modulated, the particles "blink" in response. Fluorescence emission from the particle is collected when the non-coated hemisphere faces towards the collection optics and no fluorescence is detected when the metallic coating is oriented towards the optics. They have demnstrated the use of these particles to remove background signals from the excitation source,[171] background autofluorescence in media such as ovine albumin,[168] and have measured the particle signal for a sample on the surface of a leaf.[169] Additionally, they have demonstrated the ability to combine the MagMOONs with chemical sensing including pH sensing.[169, 171] In all cases, successful removal of background signals were achieved.

Our group has developed a MagMOON probe for studying de-gelation processes through tissue that may be useful for applications in drug delivery. MagMOON probes were incorporated into alginate gels. MagMOON position was fixed during the gelation process. After the addition of alginate lyase to the sample, the gel began to break-down resulting in an increase in particle "blinking"/rotation as the particles became "free" in the matrix. Blinking of the particles was observed through 4 mm of chicken breast tissue.[173-174] Additionally, we have demonstrated the tracking of MagMOONs in live cells.[174]

In this chapter, we will present the development of an orientation dependent implantable fluorescent sensor for monitoring local pH changes of the surface of medical devices. The novelty of the sensors lies in their ability to discriminate between sensor signal and autofluorescence produced by biological tissues by a simple subtraction method. The sensor are comprised of three essential components: a sensor strip containing a pH sensitive dye and quantum dots which are insensitive to changes in H^+ concentration, an opaque mask, and a tube magnet (magnetized across its diameter). The sensor strip is wrapped around one side of the magnet, while the mask is positioned directly opposing the sensor. After assembly, the sensor is positioned between a spectrometer and a secondary magnet; this secondary magnet is attached to a stepper motor used to control rotation of the sensor. When the sensor is illuminated with a red-light source, the pH sensitive dye emits a fluorescent signal that is captured by spectrometer when the sensor strip is oriented towards the collection system. Alternatively, when the external magnet is rotated resulting in a re-orientation of the tube magnet (mask towards the collection system), the signal acquired can be attributed to background luminenscence. The background luminescence may be of several origins including tissue autofluorescence and bleedthrough of the laser excitation source.

We have selected to monitor pH, as local *in vivo* pH monitoring is essential for the detection of bacterial infections on the surface of implanted medical devices. Orthopedic implants including fracture fixation devices are susceptible to infection and the formation of biofilms on the surface. Approximately 5 – 10 % of the 2 million fixations performed each year result in implant infection, resulting in an approximate US

expenditure of $15,000 per patient.[5-6] The frequency of infection of implanted devices is particularly high for soldiers with battlefield injuries; approximately 40 % of these internal fixation cases result in infection.[175]

Implant infections are often difficult to eradicate due to the formation of biofilms on the device surface.[6, 176] Biofilms are colonies of bacteria that exhibit hypoxic regions and heterogeneous pH, are highly resistant to antibiotic treatment, and often contain dormant bacteria.[2, 5, 177] The microbes contained in biofilms are approximately 10 – 1000 times less prone to antimicrobials than planktonic microbes.[5-6, 177-178] Biofilms are nutrient deficient causing them to become slow or non-growing. A large majority of biofilms that form on implanted medical devices are staphylococcal, with approximately two-thirds of the infections caused by *Staphylococcus aureus* or coagulase-negative staphylococci.[4-5] Other common microorganisms associated with implant infection include gram-negative bacilli, anaerobes, enterococci, and polymicrobial microorganisms.[5]

Our aim is to incorporate the magnetically modulated sensor onto the surface of implanted biomedical devices to provide a non-invasive method for pH monitoring. Although several methods of measuring pH are widely available including litmus paper, pH electrodes, and a variety of pH indicating dyes and stains, measuring pH through tissue remains challenging. pH monitoring through biological tissues has been previously demonstrated by the use of NMR, ion sensitive field effect transistors (ISFET), optical fibers and the development of a radiotelemetric pH device (BRAVO™). Each technique is associated with inherent limitations such as the need for compartmentalization of the

electrical components from biological fluids for ISFETs.[179] Additionally, some of the named techniques are impractical for *in vivo* monitoring as a result of long response times, sensor integrity, and the need for frequent calibration.

Our group has demonstrated pH detection through tissue with the use of upconversion luminescent and x-ray excited optical luminescent sensors that detect pH by capturing a luminescent signal generated from a particle film modulated by absorption from a pH sesnitive dye. As the pH in close proximity to the sensor increases, the pH sensitive dye absorbs more strongly the luminescence from the particle film. Using a ratiometric approach, where a portion of the luminescence signal from the particle film remains unaltered by the change in absorption of the dye, pH was determined by calculating a spectral ratio of the unmodulated to modulated portion of the curve. This approach has shown great promise and has been applied to the detection and treatment of bacterial growth (*Staphylococcus epidermidis*) using ciprofloxacin.[62, 128] Although this approach has been successful, it has a few limitations including the use of ionizing radiation in the case of the XEOL sensor. The measurements also require the inclusion of an internal reference region to assess effects from the tissue sample. When upconversion is used as the light source, it is expected that the background will be low. Although this was observed, upconversion is a less efficient process than XEOL and fluorescence. The sensor described in this chapter utilizes the collection of fluorescence emission from two luminescent materials – one which is pH dependent and the other pH independent. The luminescent measurements in combination with magnetic modulation allows for background subtraction to be performed.

Herein we report the results of our preliminary studies for pH measurements through tissue using our prototyoe sensor design.

4.2 Materials and Methods

Fabrication of pH Sensor Strips

pH sensor strips were prepared on qualitative 413 filter paper sheets (VWR) cut into 12 mm x 6.7 mm rectangles. Water dispersible quantum dots, QSH 645, (Ocean Nanotechnology, San Diego, CA, USA) were diluted in a 1:2 ratio. QSH 645 quantum dots have a CdSSe core and a ZnS shell; the particle shell is functionalized with carboxylic acid moities. To each filter paper strip, 40 µl of the quantum dot solution was drop-coated in 10 µl additions, allowing the filter paper to dry and the particles to absorb into the substrate between subsequent additions. After air drying, a 15 µl aliquot of 5(6)-carboxynaphthofluorescein (1.56 mg/ml in reagent alcohol) was added to each strip and air dryed. Reagent alcohol was purchased from VWR and 5(6)-carboxynaphthofluorescein from Marker Gene Technologies, Inc. (Eugene, OR, USA). The pH of each strip was then modified with the addition of 60 µl of buffer (pH values 4 – 10). All buffers used were commercially available and were purchased from VWR. pH values below 4 were not investigated due to the instability of the quantum dots at low pH, pH <5. Sensors were stored in the dark to minimize photobleaching during air drying of the sensors.

Spectral Ratio Calibration Curve

After complete drying of the pH sensor strips, a fluorescence emission spectrum of each sensor was acquired. For each sample, the sensor strip was contained in a petri dish for cell culturing (35 x 10 mm sterile petri dish, Electron Microscopy Sciences, Hatfield, PA, USA). The petri dish was placed on a glass slide on the stage of an inverted fluorescence microscope, Leica DMI 5000 (Leica Microsystems, Germany). All fluorescence emission measurements for calibration were collected with a 10 x microscope objective and a collection distance of 3.02 mm between the bottom plane of the glass slide and the objective lens. Samples were irradiated from below with a 632.8 nm HeNe laser (laser power 5 mW) filtered through a 633 nm laser line excitation filter (Chroma Technology Corp, Bellows Falls, VT, USA) before reaching the sample. The red laser (model HRP050-1) was purchased from ThorLabs in Newton, NJ, USA. Fluorescence emission captured by the objective lens was filtered through a 646 nm longpass filter (Chroma Technology Corp, Bellows Falls, VT, USA) housed within a filter cube. The filtered emission was passed through a cylindrical lens at the exit of the microscope to increase collection efficiency before it was directed into the slit of a DeltaNu spectrometer (DNS 300, DeltaNu, Laramie, WY). A grating with 1,200 lines per mm was used to diffract the incoming light and the dispersed signal was collected by a cooled (- 65 °C) iDUS-20BV CCD camera (Andor, South Windsor, CT, USA). The spectrometer and CCD settings were controlled with Andor Solis software. For calibration measurements, the exposure time was set to 0.01s, the read-out rate 100 kHz @ 16-bit, the shift speed 8.25, the pre-amplifier gain was set to 1x, and full vertical

binning was selected. Under these conditions, the spectrometer read-out reported in counts is equivalent to 15 photoelectrons per count. From each spectrum, intensity measurements were averaged over a width of 11 pixels (wavelength regions 697.3 nm – 702.8 nm and 657.9 nm – 663.5 nm). A ratio of the average intensities was calculated (I_{700}/I_{660}) and plotted versus the pH of the buffer solution used for preparation. Each ratio is reported as the average and standard deviation of 3 independent trials performed with 3 different sensors constructed with the same pH buffer.

Fabrication of Magnetic pH Sensors

After calibration measurements were recorded, double-sided tape was added to the back side of each strip used for magnet studies (pH 7 and pH 10 sensor strips). The sensor strip was wrapped around the length of a cylindrical tube magnet (magnetized across its diameter) purchased from SuperMagnetMan. The magnets were 12 mm long with and outer diameter of 4 mm and an inner diameter of 1.5 mm. The remaining uncoated half of the magnet was masked off with black electrical tape. Slight overlap of the electrical tape on top of the sensor strip allowed for insurance that the sensor strip would not dettach from the magnet due to friction between the rotating magnet and tissue sample to be placed above and below. Electrical wire was run through the inner hole of the tube magnet to allow for an axis for the tube magnet to rotate about upon application of an external magnetic field. On either side of the tube magnet, electrical tape was wound around the electrical wire to prevent translation of the magnet along the wire during rotation.

Luminescent Measurements during Magnetic Modulation

To conduct luminescent measurements during magnet rotation, the prepared pH tube sensor was positioned above the 10 x objective of the inverted fluorescence miroscope and the electrical wire was attached to the microscope stage on either side. Below the sensor, a petri dish (Greiner bio-one petri dish, 94 x 16, VWR) was placed on the stage to hold the tissue sample; for consistency an empty petri dish was present below the sample in studies conducted in the absence of tissue. A NdFeB magnet (magnetic material grade N45H) was positioned above the microscope stage/tube sensor. The external magnet was attached to a stepper motor (1.8 degree hybrid stepper motor, Applied Motion Products, CA, USA) controlled with SI programmer (Applied Motion Products, Inc., Watsonville, CA, USA). Details of the modulation are provided in appendix D. Briefly, the magnet was rotated 1,000 steps forward and the position maintained for a set time (2.5 s in the absence of tissue and 16.0 s in the presence of tissue). After the wait time, the magnet was rotated another 1,000 steps and the wait time repeated. The cycle was repeated for the duration of the luminescent measurements.

All luminescent measurements were collected with the system described above for calibration measurements with slight modifications in focal length and program settings. For trials performed in the absence of tissue, a kinetic series was programmed in the Andor Solis software to collect spectra with a 0.25 s exposure, a kinetic cycle time of 0.26326 s, and a kinetic series length of 200. Approximately 10 spectra were collected at each magnet position in accordance with the 2.5 s motor wait time between each rotation. The focal length between the petri dish on the microscope stage and the objective lens

was set to a maximum (z = 0 mm). For through tissue measurements, Tyson all natural chicken breast was purchased, sliced with a meat slicer (Edgecraft Corporation, Chef'sChoice International™ Gourmet Electric Food Slicer Model 630, Avondale, PA, USA) to a thickness of 6 mm, and wrapped in Glad® clear cling wrap (The Glad Products Company, Oakland, CA, USA). One chicken breast slice was placed below the sensor in the petri dish and the other layed directly on top of the sensor to sandwhich it. A kinetic series was programmed in Andor Solis with an exposure time of 4.00 s, a kinetic cycle time of 4.01325 s and a kinetic series length of 100 spectra. Approximately 4 spectra were recorded at each position of the magnet. The objective was set to a maximum height of 8.63 mm below the sample. For all measurements, the sample was irradiated from below. No further modifications were made in the readout settings of the spectrometer.

To determine pH from the spectral data, intensity averages were calculated (I_{700} and $I_{660)}$ for all spectra and plotted versus spectrum number. The ratios were then seperated into two different classes; the "on" and "off" positions of the sensor, where "on" corresponds to measurements recorded when the pH sensitive dye was facing towards the objective lens and the "off" spectra where the masked side of the tube magnet was facing towards the objective. All intensity averages falling between the two extremes were disregarded during calculations. These intermediate positions are a result of differences between the cycle time of the spectral acquisition system and the wait time of the magnet. The average intensity of the "on" and "off" positions for the wavelength regions 697.3 nm – 702.8 nm and 657.9 nm – 663.5 nm were calculated. The "off"

average for each wavelength range was subtracted from the corresponding "on" position. A ratio of the resulting intensity measurements was determined (($I_{700\ (\text{"ON-OFF"})}$)/($I_{660\ (\text{"ON-OFF"})}$) and compared with the calibration curve.

4.3 Results and Discussion

We have developed a position-dependent luminescent sensor to effectively discriminate between fluorescence from an exogenous fluorescent sensor (i.e fluorescent pH sensor) and endogenoues fluorescent moities within biological tissue samples. The fluorescent sensing strip contains a pH sensitive fluorescent dye and pH insensitive quantum dots that serve as a spectral reference. Our approach to background subtraction is similar to work in the Kopelman lab at the University of Michigan for the development of a pH sensing magnetic microdrill. Their sensor design contained a drill bit with a polymer coating (poly(methylmethacrylate) or polyvinyl chloride) containing pH sensitive dye (5(6)-carboxynaphthofluorescein or ETH5350) and a NdFeB magnet attached to the head of the drill bit. One side of the drill bit was darkened to block fluorescence emission. Rotation of the drill bit, controlled with an external magnetic field resulted in emission spectra in "on" and "off" positions. The "on" position corresponding to signal from the pH dye and the "off" corresponding to background when the darkened coating was oriented towards the collection system. With their magnetic modulation experiments they were able to reduce the contribution of background to their overall signal by a factor of 100 when luminescent measurements were recorded for the drill rotating through a gelatin medium.[180]

We have extended the work of the Kopelman group (MagMOONs and the magnetic microdrill) with the construction of a rotating sensor for pH measurements **through tissue** to be made on the surface of orthopedic implants. A schematic of our experimental design and collection system for luminescent measurements is provided in **figure 4.2.** As our pH indicator, we have selected 5(6)-carboxynaphthofluorescein (CNF), with a pKa of 7.6. Fluorescence emission spectra of CNF prepared in solution (reagent alcohol) with pH modified with commercially available buffers are shown in **figure 4.3**. These measurements indicate that location of the fluorescence emssion maximum (~ 673 nm) remains unaltered as a funtion of pH. However fluorescence emission intensity decreases as the pH is decreased. At acidic and neutral pH values, the excitation maximum for the dye is 512 nm, while at basic pH the λ_{max} red shifts and is reported as 598 nm. Meier et al. have devleoped a FRET-based pH sensor that takes advantge of this red-shift.[167] In our experiments, as the pH of the dye is increased, the dye more effectively absorbs the 633 nm light that was used as the excitation source.

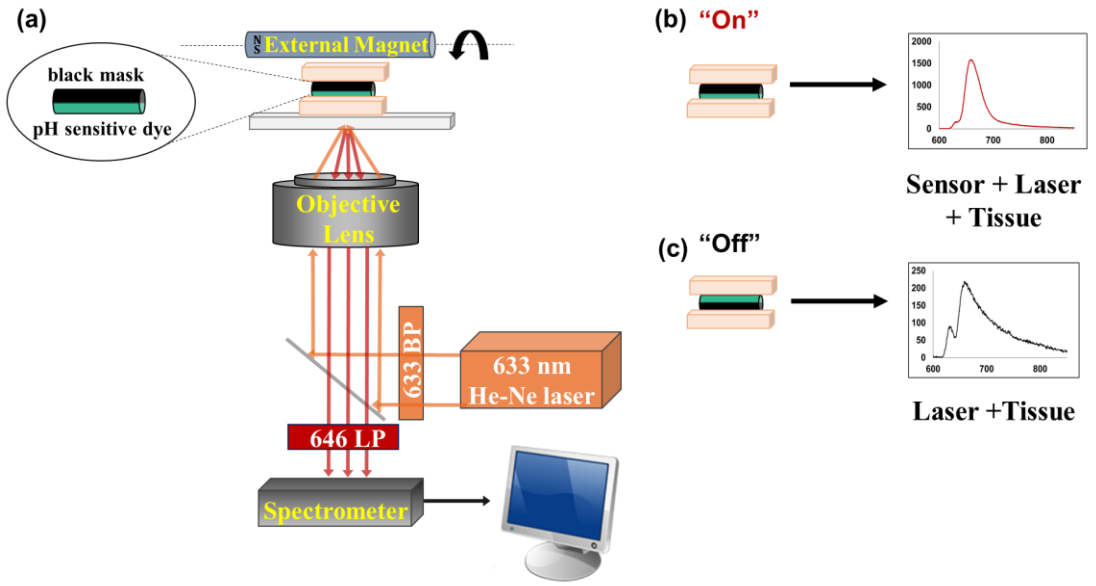

Figure 4.2 Schematic of experimental set-up showing a magnetic pH sensor sandwiched between two pieces of chicken breast tissue on the stage of an inverted fluorescence microscope. Position of the sensor is modulated by rotation of an external magnet above the microscope stage. The sensor is composed of a magnetic cylinder, magnetized along its length, and coated anisotropically. One half of the sensor contains a pH sensitive dye and a quantum dot particle reference material and the other side of the sensor is masked with black electrical tape. The sensor is excited with 633 nm light and the fluorescence emission is collected with a 10 x microscope objective before wavelengths < 646 nm are rejected. The remaining fluorescence emission signal travels to a CCD camera. (b) shows the collected signal for the "on" position of the sensor (dye oriented towards the objective lens). The total signal is comprised of fluorescence emission from the sensor, background from the tissue, and unfiltered laser emission reaching the detector. (c) shows the sensor in the "off" position (masked region of the sensor facing the objective) resulting in signal

collection from the laser and the background from the tissue. In this position luminescence is not collected from the pH sensitive dye.

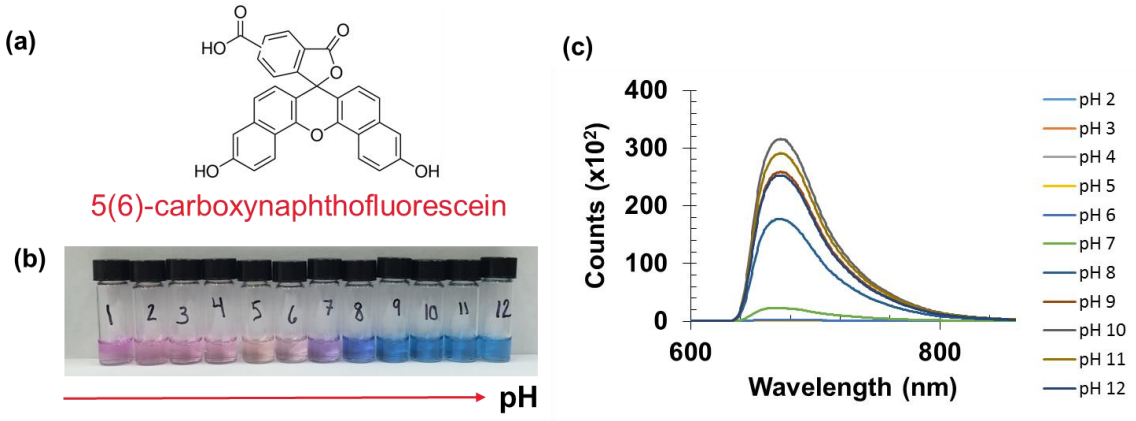

Figure 4.3 (a) Chemical structure of 5(6)-carboxynaphthofluorescein. (b) 5(6)-carboxynaphthofluorescein dissolved in reagent alcohol (0.39 mg/ml) and mixed with buffers ranging from pH 1 – pH 12 in a 2:100 dye solution to buffer ratio showing the change in solution color from pale pink at acidic pH to blue at basic pH. (c) Fluorescence emission spectra of dye solutions depicted in (b) under 633 nm excitation. The dye emission maximum is located at ~ 673 nm for solutions prepared in reagent alcohol.

Although CNF is a ratiometric pH dye, exhibiting an isosbetic point at ~ 640 nm in phosphate buffers, we have selected to calculate spectral ratios for pH determination with the addition of a secondary luminescent material. We have made this selection in order to utilize red light as our excitation source. Red light was chosen because as the wavelength of visible light increases there is a decrease in the amount of tissue autofluorescence observed.[55] The optimal window for tissue imaging is considered to be

~ 600 – 1,000 nm and has been coined the "therapeutic window." [158] In addition to a decrease in autofluorescence, increasing the excitation wavelength results in lower absorption and scattering coefficients. Below 600 nm, the tissue absorption coefficient (cm^{-1}) is greater than 1, however drops to less than 0.1 by 650 nm. However, if excitation and emission are pushed above this region, >1000 nm, water absorption becomes increasingly prevalent.[55, 78, 158] Utilizing CNF alone to calculate spectral ratios would necessitate the use of either ~ 488 nm or ~515 nm light as the excitation source. This would result in increased autofluorescence in the tissue as well as greater absorption and scattering of the excitation wavelength.

As the secondary luminescent material, water dispersible quantum dots with a maximum emission at 645 nanometers were incorporated into the sensor strips. The quantum dots were selected because they are photostable, have narrow emission, and have good spectral overlap with CNF. By selecting closely spaced or in this case overlapping peaks, spectral distortion when passing through tissue is minimized. Overlaid emission spectra of the quantum dots and CNF (pH 7) are shown in **figure 4.4**.

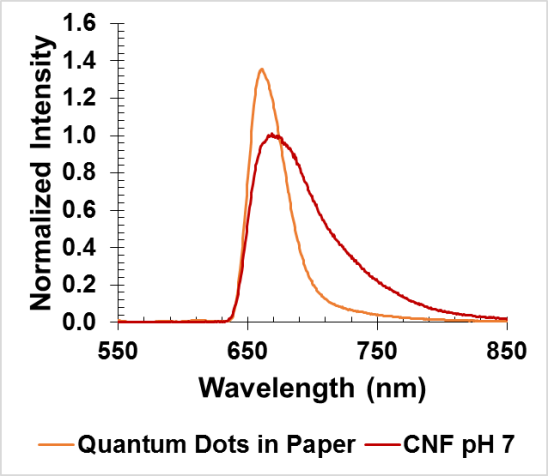

Figure 4.4 Overlaid quantum dot and CNF dye (pH 7) emission spectra excited with a 633 nm laser.

When CNF is added to the filter paper strips along with quantum dots, the luminescence emission from 633 nm excitation is a combination of the two spectra presented in **figure 4.4**. A calibration curve was constructed for sensors strips with pH values ranging between pH 5 and pH 10. The luminescent emission spectra are presented in **figure 4.5**. The shift in λ_{max} agrees with the expected trend; the emssion maximum is red-shifted as basicity is increased due to the red-shifted absorption maximum of CNF. At low pH values, luminescence from the quantum dots dominates the overall emission signal collected. However, as pH of the sensor strip is increased, the emission collected is predominantly from the CNF dye.

pH values below 5 were not investigated due to the pH stability range reported for the quantum dots. Luminescence ratios for pH sensor strips prepared with pH 9 buffer were excluded from the sample set as the data points were outliers. It is hypothesized that

boric acid, a component of the pH 9 buffer reacts adversely with either the filter paper medium or the fluorescent materials. Further invesitgation of this observation needs to be conducted. Alternatively, future sensors will be prepared with a pH 9 buffer with a different chemical composition.

From the luminescence data collected, spectral intensity values were averaged from 697.3 nm to 702.8 nm and from 657.9 nm to 663.5 nm. A ratio of the luminescnece average was calculated (I_{700}/I_{661}) and plotted versus pH of the buffer. Each point in the calibration curve represents the average of three independent measurements from unique samples. Error bars indicate standard deviation among the three samples. **Table 4.1** reports the spectral ratio for each sensor measured. It is evident that there is greater variation in spectral ratios calculated at higher pH values (e.g ± 0.025 for pH 5 and ± 0.080 for pH 10). During sample preparation, it was noted that there was more dye leaching at higher pH, which supports the evidence of statistical variations. Future investigations will include the quantification of dye leaching.

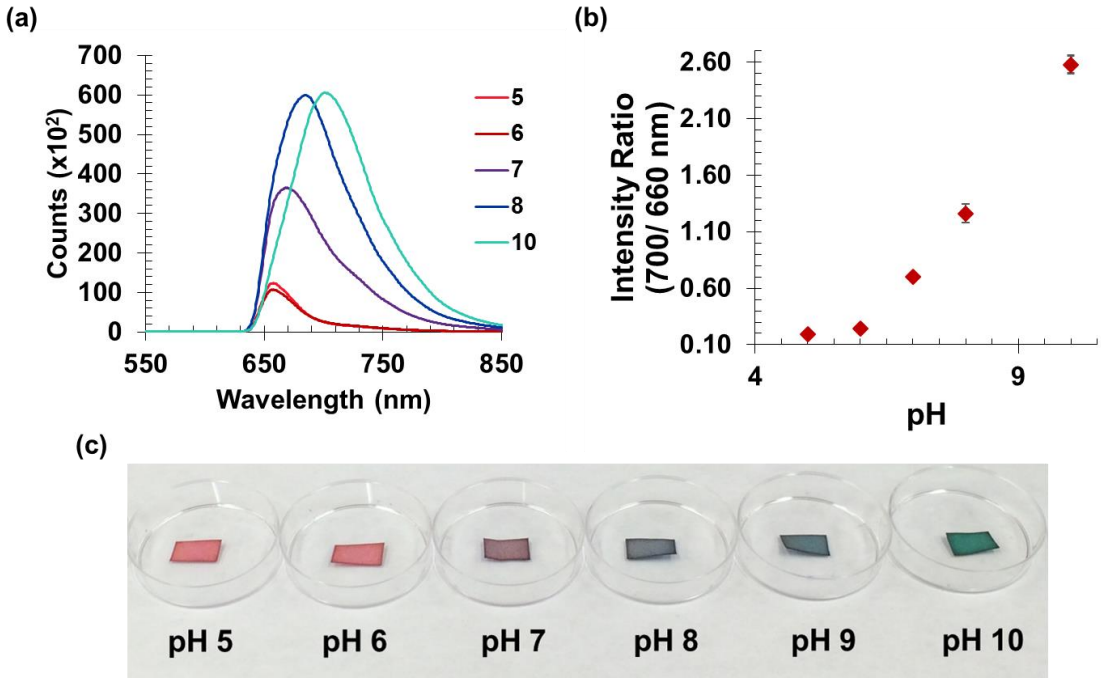

Figure 4.5 (a) Fluorescence emission of sensor strips containing CNF dye and CdSSe/ZnS core shell quantum dots at pH values 5 – 10. As the basicity is increased, the emission maximum red shifts due to the increased absorption of 633 nm light by CNF. Quantum dot fluorescence emission is independent of pH. (b) pH sensor calibration curve for the sensor strips before attachment to a cylindrical magnet. Greater deviation is observed at higher pH due to increased dye leaching during sensor preparation. (c) Photograph of prepared sensor strips.

	Spectral Ratio				
pH	**5**	**6**	**7**	**8**	**10**
Sample 1	0.21	0.25	0.68	1.20	2.67
Sample 2	0.17	0.22	0.73	1.36	2.53
Sample 3	0.20	0.25	0.69	1.23	2.53
Average	0.19	0.24	0.70	1.26	2.58
Standard Deviation	± 0.025	± 0.020	± 0.028	± 0.083	± 0.080

Table 4.1 Spectral ratios (I_{700}/I_{660}) for sensor strips prepared with pH buffers 5,6,7,8 and 10 as shown in the calibration curve (**figure 4.4**). pH 9 was omitted as the spectral ratio values were found to be outliers. The average and standard deviation are reported for 3 separate samples prepared under the same conditions.

Prior to luminescence measurements through tissue, a spectrum of the chicken breast used in the reported trials was acquired with the same acquisition settings as the magnetically modulated pH sensors. The characteristic chicken breast spectrum with 633 nm excitation is provided below.

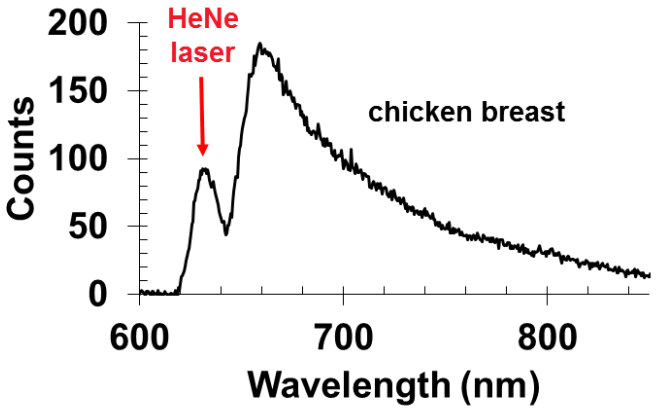

Figure 4.6 Fluorescence emission spectrum of 12 mm of chicken breast excited with a He-Ne laser (633 nm) with an exposure time of 5.0 s. Bleed-through of excitation light not blocked by the 633 nm short pass filter is observed at long exposures. The tissue has an autofluorescence maximum at ~ 660 nm, and emission within the same wavelength range as the emission of the pH sensitive dye and quantum dot reference.

pH sensor strips (pH 7 and pH 10) were further investigated and spectral ratio values were determined in the absence and presence of tissue in combination with our design for magnetically modulated sensing. Each sensor strip used for calibration was attached to one side of a cylindrical tube magnet and the opposite side blackened with electrical tape. The tube magnet contained a hole through its center; an electrical wire was fit through the opening. The purpose of the wire was to provide an axis for the magnet to rotate about and allowed the position of the magnet to be fixed to the microscope stage. Rotation of the magnet was controlled by a NdFeB magnet attached to a stepper motor controlled with SI programmer. In the absence of tissue, the excitation exposure time was set to 0.25 s and approximately 10 spectra were recorded before

rotation of the magnet by 180 °. When the sensor was sandwiched between 2 pieces of 6 mm thick chicken breast, the exposure was increased to 4.0 s to achieve a sufficiently bright signal through tissue. Signal intensity is significantly reduced through tissue as a result of absorption and scattering. Approximately 4 spectra were recorded at each position of the magnet before rotation. The number of acquisitions was reduced for through tissue measurements to prevent bleaching of CNF over time.

Spectra for "on" and "off" positions for pH 10 sensors are presented in **figure 4.7** below. Inset graphs in (b) and (d) highlight the signal for the "off" position. In the absence of tissue, minimal signal is collected in the "off" position. Counts collected can be attributed to room light or the capture of scattered excitation, however, the signal is negligible. **Figure 4.6c** and **4.6e** show average intensities at 700 and 661 nm. At pH 10, luminescence from CNF dominates the spectrum, which is evident by the more intense signal averages at 700 nm than at 661 nm. For the trial highlighted below, there was an average background signal of 125 counts (1,875 photoelectrons) at 700 nm and 82 counts (1,230 photoelectrons) at 661 nm through tissue. These "off" values were subtracted from the average of the "on" intensities. A spectral ratio as calculated from the corrected values.

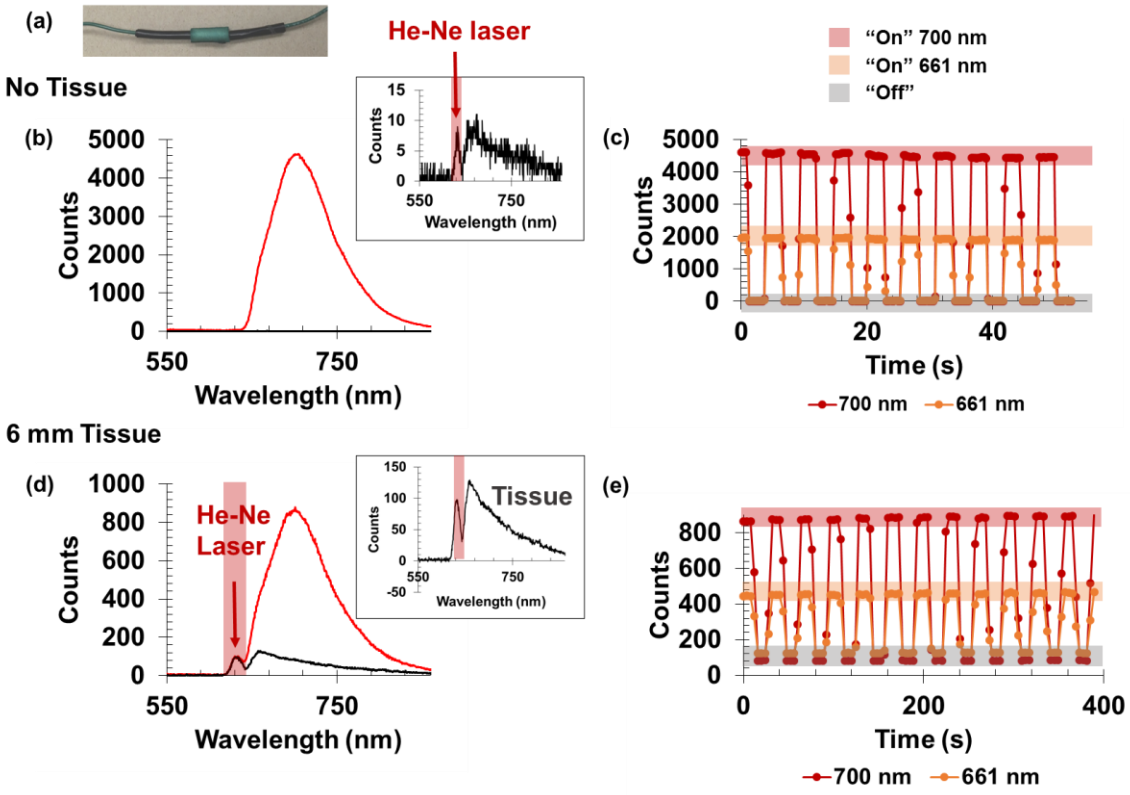

Figure 4.7 (a) Photograph of assembled pH 10 sensor. (b) pH 10 sensor strip (sample 1) fluorescence emission spectrum in the "on" position where the pH sensor is oriented towards the microscope objective. Inset graph shows the signal from the sensor in the "off" orientation. (b) Plot of luminescence intensity vs. time as the external magnet is rotated (the external magnet was rotated every 2.5 seconds). Shaded regions highlight "on" and "off" positions of the sensor. Intermediary values were discarded in determination of sensor pH. (c) Fluorescence emission from pH 10 sensor strip (sample 3) attached to a tube magnet and sandwiched between 2 slices of 6 mm thick chicken breast wrapped in cling wrap. Due to an increased exposure time, luminescence from the 633 nm laser can be seen in the spectrum as it was not efficiently blocked by the 646 nm long pass filter. Inset graph shows the fluorescence signal from the chicken breast tissue.

(d) Intensity measurements for the through tissue sample as a result of magnetic modulation. The external magnet was rotated every 16 seconds; a total of 100 spectra were acquired.

	No Tissue		Tissue	
	Spectral Ratio	**Calculated pH**	**Spectral Ratio**	**Calculated pH**
Sample 1	2.34^{+}	9.64	2.42	9.77
Sample 2	2.75	10.26	2.79	10.32
Sample 3	2.12	9.30	2.41	9.74
Average	2.40	**9.73**	2.54	**9.94**
Standard Deviation	0.320	**0.486**	0.217	**0.329**

Table 4.2 Summary of spectral ratios for pH 10 sensor strips with luminescent signals modulated by an external magnetic field. Average and standard deviation of spectral ratios were calculated for the same 3 sensor strips used to generate the calibration curve. Table value denoted with a ($^{+}$) represents the average of 2 trials. pH was determined by interpolation using pH 8 and pH 10 calibration values to calculate slope. The calculated pH agrees within less than half a pH unit from the expected pH (pH of the buffer).

Spectral ratios for all pH 10 sensor trials are reported in **table 4.2**. In the absence of tissue, the sensor reads an average spectral ratio of 2.40 ± 0.320 and 2.54 ± 0.217 through tissue. Observed spectral ratios were converted into pH values by interpolation using pH 8 and pH 10 to calculate slope. In the absence of tissue, the pH read by the sensor was 9.73 ± 0.486 pH units. We hypothesize that variations in the pH measurements may be a result of heterogeneity across the sensor surface. From measurements acquired for the calibration curve, the spectral ratios ranged from 2.53 to

2.67, with an average and standard deviation of 2.58 ± 0.080, showing ~ 3 times the variation of the pH 7 sensors also investigated.

The average pH value calculated from measurements conducted through 6 mm chicken breast was 9.94 ± 0.329, showing better agreement with the calibration curve than the measurements without tissue. This variation may also be a result of heterogeneity. In the presence of the tissue sample, the laser spot has spread approximately 6 mm more than in the absence of tissue, assuming the laser spot size increases 1 mm per millimeter of chicken breast tissue. The increased illumination area may provide a better estimation of the overall composition of the sensor.

In addition to pH 10 we have verified the accuracy of the sensor using pH 7 sensor strips. Spectra and average intensity measurements are shown in **figure 4.8**. At pH 7, evidence of the quantum dot emission is more apparent. The emission from the quantum dots is not affected by the pH of the buffer, however, CNF does not absorb the excitation wavelength as strongly at pH 7 in comparison with pH 10. In the absence of tissue the average calculated pH value (6.97 ± 0.081 units) agrees well with the expected pH of the buffer. Average and standard deviation values are reported in **table 4.3**. Values calculated for through tissue measurements are on average lower than expected, with an average pH of 6.79 ± 0.089. The pH 7 sensor strips can estimate pH with a precision of approximately 0.09 pH units.

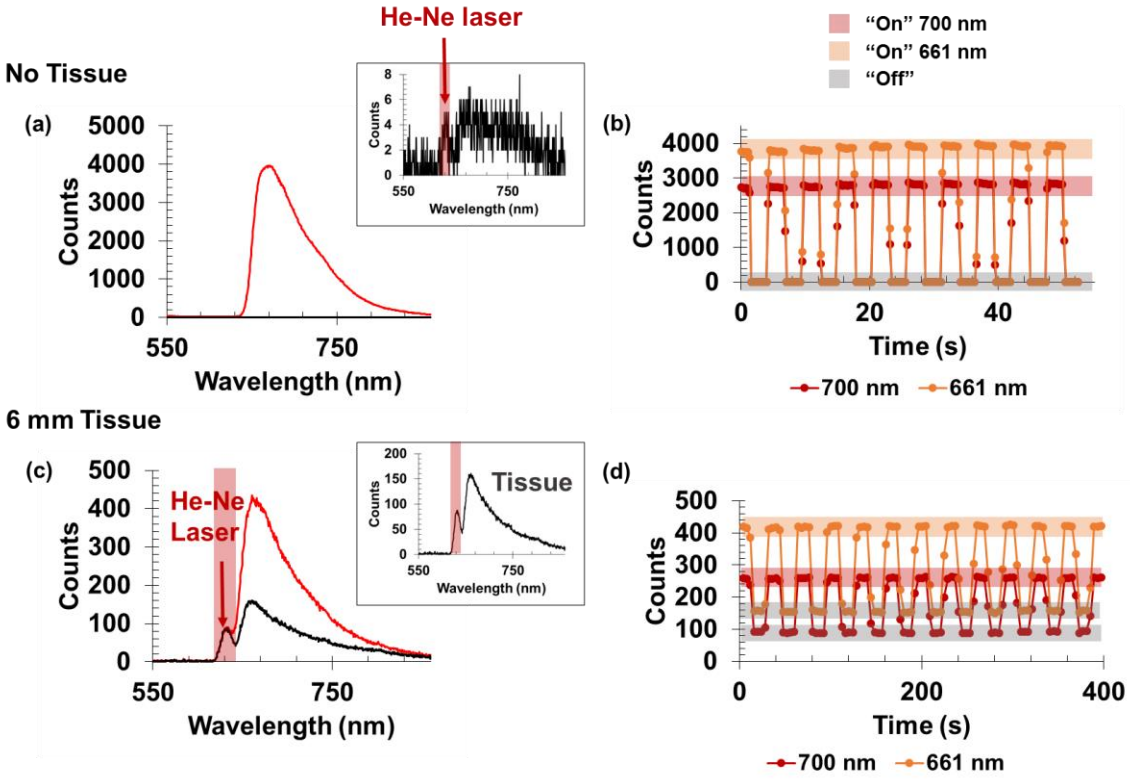

Figure 4.8 (a) pH 7 sensor strip (sample 1) fluorescence emission spectrum in the "on" position where the pH sensor is oriented towards the microscope objective. Inset graph shows the low number of counts collected (< ~ 7 counts) from the sensor in the "off" orientation. (b) Plot of luminescence intensity vs. time as the external magnet is rotated. Shaded regions highlight "on" and "off" positions of the sensor. Intermediary values were discarded in determination of sensor pH. (c) Fluorescence emission from pH 7 sensor strip (sample 2) attached to a tube magnet and sandwiched between 2 slices of 6 mm thick chicken breast wrapped in cling wrap. Inset graph shows the fluorescence signal from the chicken breast tissue (maximum of ~ 150 counts at ~ 662 nm). (d) Intensity measurements for the through tissue sample as a result of magnetic modulation.

	No Tissue		Tissue	
	Spectral Ratio	**Calculated pH**	**Spectral Ratio**	**Calculated pH**
Sample 1	0.72	7.04	0.55	6.72
Sample 2	0.70^{+}	7.00	0.64	6.89
Sample 3	0.63^{+}	6.88	0.56	6.75
Average	0.68	**6.97**	0.58	**6.79**
Standard Deviation	0.046	**0.081**	0.050	**0.089**

Table 4.3 Summary of spectral ratios for pH 7 sensor strips with luminescent signals modulated by an external magnetic field. Average and standard deviation of spectral ratios were calculated for the same 3 sensor strips used to generate the calibration curve. Table values denoted with a ($^{+}$) represent the average of 2 trials. pH was calculated by interpolation using pH 7 and 8 ratios from the calibration curve. The calculated pH agrees within ~ 0.30 pH units with the expected pH (pH of the buffer).

Although we have demonstrated proof of principle with our pH sensors, in order to improve the accuracy of the pH value read, several challenges must be addressed including uniformity of the pH sensitive strip, leaching of the pH sensitive dye, and bleaching of the fluorescent materials. Below each limitation is briefly addressed.

Sensor uniformity is essential for reproducible measurements between sample sets as well as for measurements collected across the surface of a single sensor. Currently, the uniformity of the sensors is limited by the pore size and distribution in the filter paper substrate. Sensors described in this work were prepared by sequential additions of luminescent materials; quantum dots were added followed by CNF dye. To improve uniformity, the pH sensitive dye and QD particles should be mixed to produce a

homogenoues solution that will then be transferred to the sensing strip. In order to prepare sensors in this fashion, it will be necessary to functionalize the surface of the quantum dots. Under current experimental conditions, when filter paper is dipped into a vial containing the dye/particle mixture, the quantum dots precipitate out. Alternatively, the paper substrate may be replaced with a biocompatible polymer that allows for the transfer of H^+ ions across its membrane. A homogenoues mixture of the luminescent materials and the polymer may be coated onto the magnet by either spin coating or dip coating rather than drop-coating (as was performed in the studies shown here).

Although our studies were able to determine an average pH of 9.94 ± 0.329 for the dry pH 10 sensors strips and a pH of 6.79 ± 0.089 for dry pH 7 sensors attached to the tube magnet, we have not successfully measured pH change in time as the CNF dye added to the sensors leaches under the current conditions. CNF readily leaches from the paper upon addition of buffer solutions, with increased leaching observed as the basicity of the buffer is increased. As a prelimiary attempt at controlling the leaching, we have coated the sensor strip with a PEG diacrylate coating. Briefly, we have prepared a PEG-DA solution containing 89.2 % 700 mW PEG diacrylate (Sigma Aldrich), 9.91 % of a 50/50 glycerol/ H_2O, and 0.89 % photoinitiator (2,2-dimethoxy-2phenylacetophenone). The pH sensor strips were coated with the polymer solution and irradiated with 356 nm light for periods ranging between ~ 3 to 15 minutes. Long photopolymerization times led to bleaching of the CNF dye. With shorter irradiation times, there appeared to be no noticeable change in the amount of leaching when the sensor was soaked in buffer, however a quantitaive assessment has not been performed.

CNF has been utilized in the literature for pH sensing and dye leaching controlled by several different approaches.[167, 181-186] For example, Kopelman et al. have incorporated CNF into acrylamide PEBBLES (probes encapsulated by biologically localized embedding).[181-183, 187] PEBBLES use a polymer matrix to encapsulate dye molecules. In their experiments, CNF was encapsulated in an acrylamide matrix by addition of a N,N-methylenebisacrylamide and acrylamide polymerization solution into an organic phase Polymerization was initiated with either sodium bisulfite solution or ammonium persulfate (APS) and N,N,N,N-tetramethylethylenediamine (TEMED). As part of their experimental work, they also investigated the interaction of CNF with albumin and have reported that CNF-albumin interactions greatly alter pH readings calculated for the ratiometric dye.[182] For this reason, as well as to control leaching, we will pursue the fabrication of CNF pebbles. Alternative encapsulation methods include conjugation with bovine serum albumin (BSA) or immobilization in an aminoethyl-cellulose matrix.[185-186] Immobilization with BSA was not effective at controlling the dye leaching, the authors report a leaching percentage of 22 % after one day. In addition to poorly resolving problems with leaching, binding with BSA would not be appropriate for long term studies using our sensors as the authors reported an increase in fluorescence intensity after storage of the BSA conjugated sensors (10 days). This would skew spectral ratios as the luminescence of the quantum dots would remain unchanged during storage.[186]

Although photobleaching did not hinder the results of the experiments reported here, the exposure time for signal collection must be considered. Fortunately, Clark et al. report that from a variety of dye containing PEBBLES synthesized in their work,

PEBBLES containing CNF showed less photobleaching. The authors attribute this observation to the low quantum efficiency of the dye.[183] On the contrary, Bidmanova et al. observed significant photobleaching of free CNF in solution illuminated with a 150-W xenon lamp (7 % fluorescence intensity reduction over a period of 3 hours).[186] Illumination times for our sensor will be much shorter than the exposure reported by Bidmanova.

Conclusions and Future Work

We demonstrated proof-of-principle for measuring pH through tissue and effectively discriminating between the sensor signal and autofluorescence of the biological tissues. The sensor has a precision of ± 0.089 at pH 7 and ± 0.329 at pH 10.

Future work will include encapsulation of the pH sensitive dye in acrylamide PEBBLES to prevent leaching. Once leaching is controlled, real-time pH measurements will be recorded as the pH of the surrounding medium is changed/ cycled.

Additionally, we will use multiplexing to increase the overall signal upon miniaturization of the device. We envision covering a section of the implanted device surface with an array of these magnetic sensors. This will not only increase luminescence emission, but will allow the pH of a large region to be investigated for heterogeneity. As an example of this idea, we show images of 2 magnetic pH sensors responding in parallel with one another as a magnet is rotated below the sensors (see **figure 4.9**). The sensors are held in a fixed position under clamps on each end.

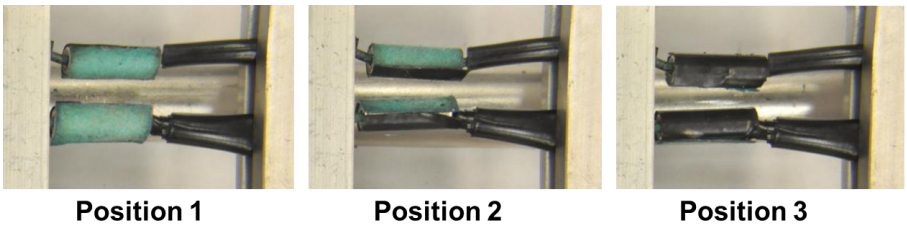

Figure 4.9 Photographs of two closely spaced magnetic pH sensors responding to a rotating magnetic field.

We will also investigate other design concepts for magnetic modulation. For example, magnetic shutters similar in design to the spectral rulers can be 3D printed from filaments containing magnetic material. Example shutters are pictured in **figure 4.10.** In this system, with the use of an external magnet, position of two overlaid shutters can be controlled. The shutters will align themselves in the position with minimum repulsion energy. In the "open" position of the shutter, luminescence from the sensor and background will be collected and in the "off" or closed position of the shutter the background signal will be obtained.

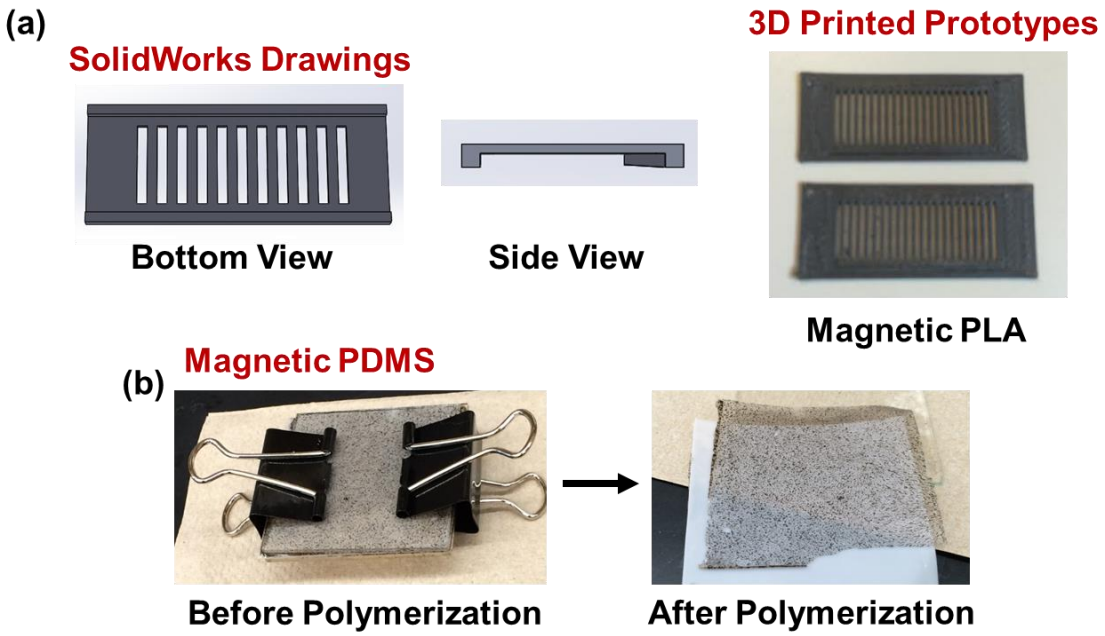

Figure 4.10 Alternative approaches for the design of a magnetically actuated pH sensor. (a) Solidworks drawings depicting a magnetic shutter. The shutter contains lines of magnetic material with a through hole between each; magnetic stripes and holes are of equal width. Overlaying two interlocking pieces results in the ability to open and close the holes as the layers are moved with respect to one another. In the presence of an external field, the shutter layers will "hop" in order to align in the position that has the minimum repulsion energy. 3D printed prototype shutters are shown. The shutters were printed with iron impregnated PLA. (b) Shutters may also be cut from thin magnetic polymer films. (b) shows polydimethylsiloxane (PDMS) mixed with iron filings sandwiched between a Teflon and transparent sheet. The system was clamped shut between two glass plates and polymerized in air.

CHAPTER FIVE

CONCLUSIONS AND FUTURE WORK

This dissertation has presented 4 variations of luminescent sensors for signal detection through biological tissues. These sensors include fluorescent, XEOL, and upconversion spectral rulers as well as a magnetically modulated fluorescent pH sensor. We have successfully demonstrated the use of position-dependent luminescence through spectral acquisition to reveal physical and chemical properties of a system. Below, we briefly summarize and compare the sensors as well as discuss future directions and applications.

5.1 Spectral Ruler Conclusions

With the development of 3 variations of spectral rulers, we have demonstrated that micron-scale displacements can be measured through tissue without the need to resolve micron-scale features. We have achieved this by acquiring luminescent spectra rather than luminescent images. The first ruler presented, the fluorescence spectral ruler, was able to provide luminescent measurements with a 2.6 μm position error through 6 mm of chicken breast tissue. By acquiring spectra using fluorescence detection, we can choose from a wide selection of luminescent materials that generate bright signals. The fluorescence sensor design allowed for luminescent signals to be generated using red-light as the excitation source. Although, this light source is desirable because red light can easily pass through tissue and is a source of non-ionizing radiation, the sensor measurements required background subtraction prior to calculating spectral ratios. The

red light excitation results in excitation of endogenous fluorophores within the tissue sample. This background can either be mathematically subtracted if the spectrum of the tissue sample and both luminescent materials is known or may be accounted for with the use of a spectral reference region. Ideally, selecting fluorophores with a large stokes-shift so that the emission is within a spectral region containing low background, would be preferable.

We overcame the autofluorescence limitation of the fluorescent ruler with the fabrication of XEOL sensors. The sensors offer essentially background-free measurements through tissue. Additionally, due to the large penetration depth of x-rays the sensor can be implanted underneath thick tissue. However, x-rays are a form of ionizing radiation, therefore x-ray dose must be considered. For the measurements reported in this work, we estimate an x-ray dose of ~ 8 cGy for a period of 3 seconds assuming constant x-ray power, a distance of 3 cm from the source of x-ray generation to the sample, and operating parameters of 50 kV and 4 watts, however, this is an overestimation of our operating voltage (40 kV). According to specifications for the x-ray source, the approximate x-ray dose rate for the sample is 1 Sv/hr at a distance of 30 cm.[188] Conversion of the x-ray dose to Sieverts, the x-ray exposure integrated by tissue type, and assuming all tissue is equivalent for a 1 cm^2 tissue area at a depth of 1 cm for a 70 kg person, the equivalent x-ray dose would be approximately 1 µSv. Although, the x-ray dose leading to an increase in cancer risk is debated, the x-ray exposure for our sensor is approximately $1/8^{th}$ of the radiation (background radiation) that a typical person is exposed to on a daily basis.[189] On average humans are exposed to ~ 8.5 µSv of radiation

each day, 310 mSv per year. Based upon data collected from atomic bomb survivors, it is believed that there is a 5 % increase risk in cancer per Sv of radiation. However, the data used to predict this increase is from patients exposed to 0.1 to 2.5 Gy. The risk above and below these values on the % cancer risk vs. exposure (Sv) curve has a linear response.[190] We hypothesize that we can decrease the x-ray dose further by increasing collection efficiency of the system. Decreasing the x-ray exposure, would decrease the sensitivity of the technique, however, this could be combatted with increased collection efficiency as well as a decrease in sensor linewidth. Current sensors contain linewidths of ~ 1 mm.

With the XEOL sensor, we achieved reproducible 14.5 μm displacements through 6 mm of chicken breast tissue. We determined a position error of 1.5 μm for this sensor for measurements through tissue and 0.7 μm in the absence of tissue.

Finally, we developed upconversion luminescent spectral rulers which combine the advantages of both the fluorescence and XEOL spectral rulers. By selecting upconversion microparticles as our luminescent material/light source, we were able to excite the sample with 980 nm light. This wavelength is optimal because it falls within a region of low absorption and scattering by the tissue and is non-ionizing. Additionally, the excitation wavelength does not excite endogenous fluorophores in the tissue resulting in a very low background signal. Using our upconversion sensor we have measured displacements with a 0.7 μm position error through tissue.

5.2 Spectral Ruler Future Directions

Future work for all variations of the spectral rulers will include miniaturization of the sensors to achieve the overall goal of implantation in the human body. We will also work to increase measurement sensitivity by reducing sensor linewidth. In order to achieve this goal, one of several approaches may be utilized. These include photolithography, nano-scale printing, laser cutting, and preparation of sensors with 3D printing. **Figure 5.1** below, demonstrates the use of nano-scale printing in our laboratory for particles and dyes on a glass surface. Closely spaced droplets or lines with equal spacing can be prepared using a benchtop printer capable of transferring attoliter to femtoliter volumes to a surface by capillary action.[191] Alternatively, spectral ruler patterns can be 3D printed with luminescent filaments prepared in-house. Using a Filabot, filament maker, we can impregnate PLA or ABS polymers with dyes that absorb red light, or x-ray scintillators, upconversion particles, quantum dots, or other luminescent materials as desired.

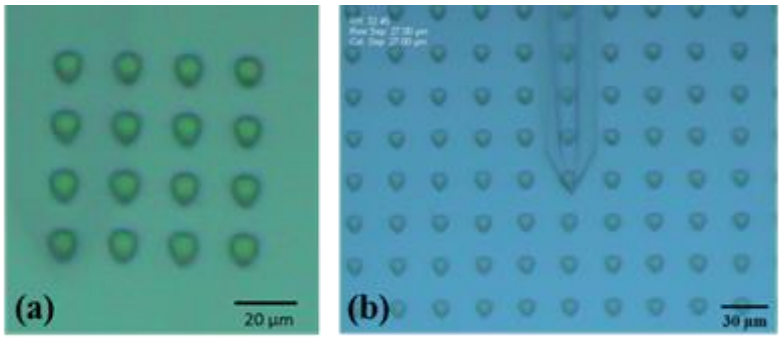

Figure 5.1 Example of an alternative way to "print" small features on a surface using a BioForce Nano eNabler™ benchtop printer. (a) An array of Gd_2O_2S:Tb x-ray scintillator particles (100 nm) in a 90 % glycerol solution[52] and (b) Nile red fluorescent nanospheres (0.054 µm) in a 90 % glycerol solution with a droplet size of ~ 8 µm showing the feasibility of preparing spectral rulers with linewidths on the order of tens of microns.

We have also demonstrated miniaturization of the sensor lines using an Epilog Engraver laser cutter with a power of 15 % and a speed of 20 %. Holes with an opening of 250 microns were fabricated.

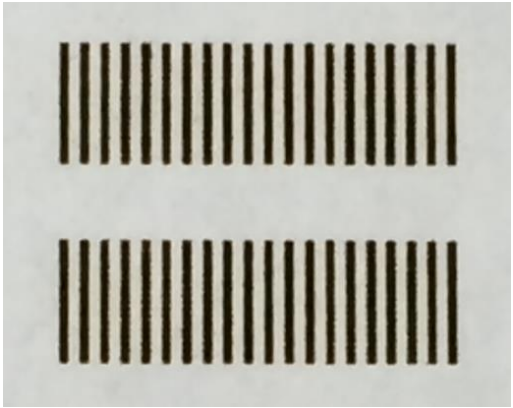

Figure 5.2 Photograph of 250 micron linewidth cuts (zoomed in) in plain copy paper made using a laser cutter.

Miniaturization of the sensor will not only help with monitoring strain on fracture fixation plates, but can aid in a secondary medical use – incorporation of the sensor into the head of a tension indicating orthopedic screw. The screw is designed to aid in monitoring hardware fatigue. Due to the size of orthopedic devices, miniaturization is necessary. The data presented in chapters 2 and 3 is for spectral rulers with linewidths of ~ 1 mm. This would significantly limit the number of pattern repetitions incorporated into the device. The orthopedic screw design, concept and preliminary luminescent measurements are provided in Appendix E.

Although the focus of the work presented here has been primarily the measurement of displacement through tissue, the spectral rulers are extremely versatile and may be applied to non-biological systems. For example, the sensor design has potential to be used in the packaging industry as a heat sensor on plastic packaging for consumer products that must be stored within a controlled temperature environment. As a demonstration of this potential application we have fabricated a spectral ruler containing an encoder that spells the word “hot” as position of the analyzer mask is altered. We have attached the analyzer mask to a piece of heat shrinkable plastic (Shrinky Dinks®) and have controlled shrinking of the plastic with the use of a heat gun. **Figure 5.3** shows photographs of the sensor before and after heating. The design of this system allowed for irreversible shrinking. This design would inform the consumer the product has reached a temperature outside the usable range for the product.

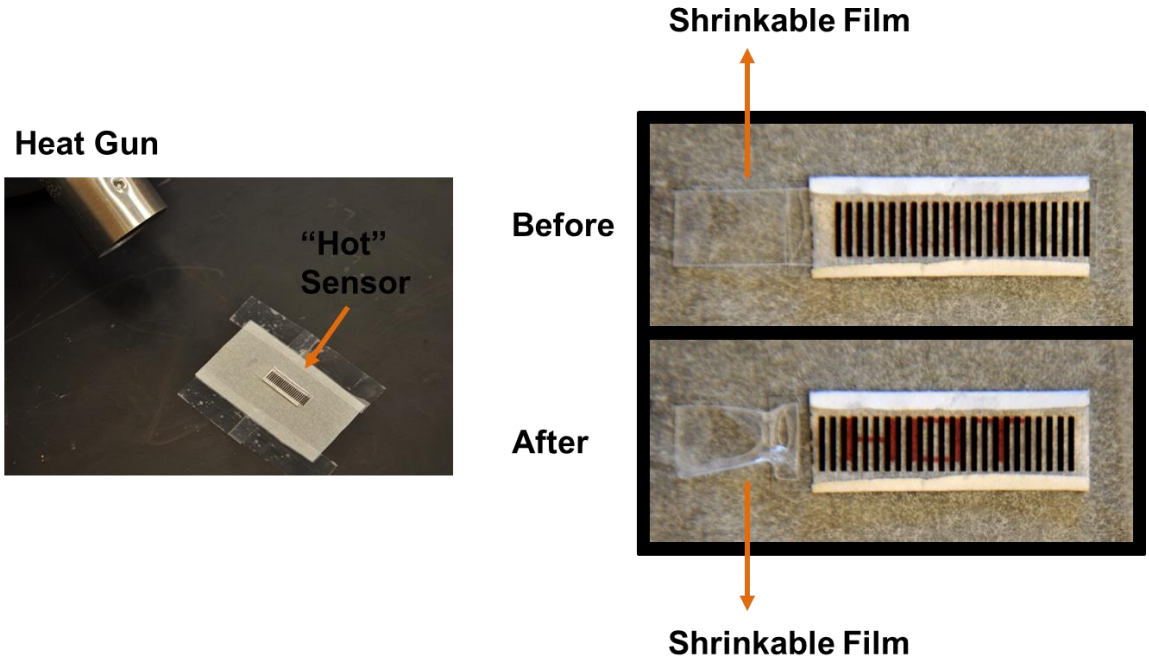

Figure 5.3 Strain sensor attached to a heat shrinkable polymer film. The image on the left shows the experimental set-up. The encoder strip is patterned with the word "hot" in red. Before heating, the words are masked, however upon heating of the polymer film, the position of the mask is shifted and the word "hot" is revealed below.

Additionally the sensor may be useful to monitor swelling of polymers. We have demonstrated this concept with the attachment of the sensor to an agarose gel. The gel was allowed to de-swell by evaporation of water at room temperature. Images of the sensor were acquired every 5 minutes over a period of 20 hours. Similar to the spectral rulers shown in chapter 2, **figure 2.1**, the images were analyzed in MATLAB (code for image processing provided in appendix A). The images tracked the change in color visible through the transparent regions of the mask from red to blue.

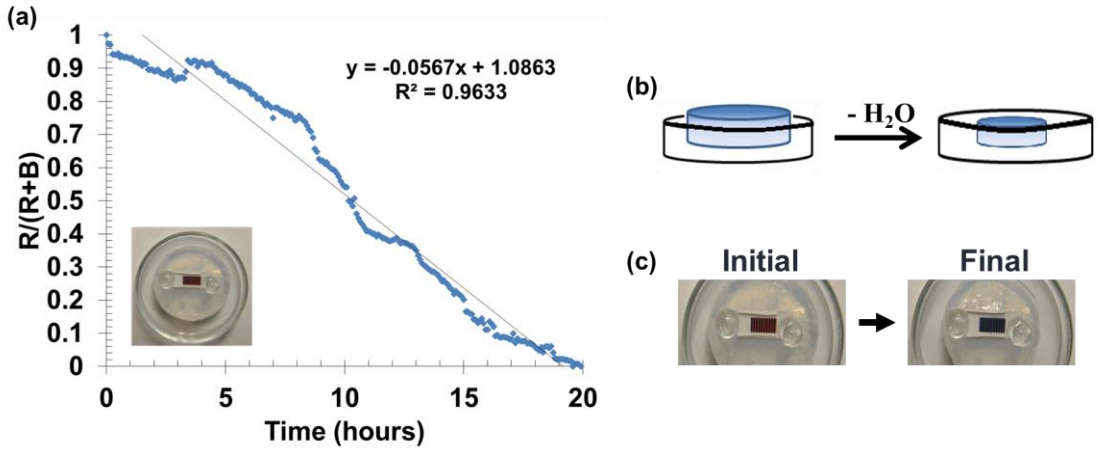

Figure 5.4 Strain detection on an agarose gel undergoing de-swelling due to evaporation. (a) Normalized color change (R/(R+B)) as a function of time showing an inset image of the gel with attached spectral ruler in the initial position before the start of position monitoring. De-swelling was monitored by acquiring an image every 5 minutes for a period of 20 hours. (b) Schematic of gel de-swelling as a result of the loss of water. (c) Initial and final positions of the spectral ruler over the imaging period showing the color change from red to blue.

Tracking the swelling of polymers may be useful for the development of *in vivo* sensors for monitoring chemical changes on the surface of orthopedic devices. Several smart hydrogel materials have been developed and their applications demonstrated in the literature. The polymers respond to one or more external stimuli including pH, temperature, ion concentration, electric fields, solvent composition and light.[192-199] These smart materials undergo a change in volume (hydrogel swelling or shrinking) that can be detected optically (by fluorescence, interferometry, refractometry, etc.),

conductimetrically, amperometrically or by mechanical means (strain gauges, magnetoelastic elements, or pressure sensors).[192, 200] These swelling sensors have been utilized to measure analytes such as glucose, to monitor changes in pH, for drug delivery and bioseparations, and to detect dissolved ions, antigens, enzymes and gases.[192, 194-195, 197-199, 201-204]

The above examples are only a few additional applications where measuring small displacements with and without tissue based on color change would be advantageous. Our proposed spectral ruler is extremely versatile, can be easily read, and has a simple straightforward design.

5.3 Magnetically Modulated pH Sensor Conclusions

We have shown that position-dependent luminescence can also be utilized for chemical sensing and using our approach we were able to overcome a major limitation of fluorescence measurements through tissue, autofluorescence. Interference from autofluorescence is shown in chapter 2, with fluorescence emission data from our spectral ruler containing quantum dots excited with red light and the autofluorescence spectrum of chicken breast tissue is highlighted in chapter 4, where we introduce our pH sensor.

By modulating the position of our pH sensor, we were able to record spectral measurements of our sensor in two different orientations. In the "on" orientation we collected luminescence of our pH sensing film, tissue autofluorescence, and bleed-through from the excitation source. In the "off" position we recorded luminescent measurements that contained only autofluorescence from the tissue and laser bleed-

through. By performing subtraction of the “on” minus “off” signals we were able to calculate a spectral ratio that could be correlated with pH based on our calibration curve for the sensor strips. Using this approach we have measured pH with a precision of ± 0.09 pH units for pH 7 and ± 0.329 for pH 10 through 6 mm of chicken breast tissue. The sensors measure pH in the range of 5 -10, difference in spectral ratio are inconclusive below pH 5 and stability of the quantum dots limits use of the sensor above pH 10.

5.4 Magnetically Modulated pH Sensor Future Work

Future work for these sensors will include optimization of the pH sensitive dye/ pH insensitive quantum dot pair as well as miniaturization of the sensor size to allow for a series of sensors to be attached along the length of an implanted medical device. By selecting a different dye/particle pair we will be able to target low pH, an indication of biofilm formation. Our current sensor is most effective in the pH range of 7 – 10. After careful selection of this pairing, we will encapsulate our sensor in a biocompatible polymer and study dye leaching.

APPENDICES

Appendix A

MATLAB Code for Determination of Color Ratio

for Spectral Rulers using Digital Photography

```
function[III, I, R, G,
B,Rm,Gm,Bm]=imageanalloadarevised(S,x_range,y_range)

% This function loads all files in a specified directory, sequentially
by time,
cd(uigetdir);
Fst=dir;
Fst=Fst(3:end);
if nargin<1,
    S=1:size(Fst,1);
end;
if nargin<3,
    x_range=1029:2564;
    y_range=495:1940;
end;

display('loading file')
for f=S,
    %display(f);
    disp(Fst(f).name);
   I=imread(Fst(f).name);
%   Iall(:,:,:,f)=I;
   Isub=I(y_range,x_range,:);
    III(:,:,:,f)=Isub;

   clear Isub;
 end;

R(:,:,:)=III(:,:,1,:);
G(:,:,:)=III(:,:,2,:);
B(:,:,:)=III(:,:,3,:);

for i=S, Rm(i)=mean(mean(R(:,:,i))); end;
for i=S, Gm(i)=mean(mean(G(:,:,i))); end;
for i=S, Bm(i)=mean(mean(B(:,:,i))); end;
figure; plot(Rm,'r'); hold; plot(Gm,'g');plot(Bm,'b');
```

Figure A-1: MATLAB script for the analysis of photographs for preliminary experiments shown in chapter 2 (**Figure 2.1**) This file determines the mean red, green, and blue contribution to the image over a specified pixel region input for the y - range and x - range.

Similar code to figure A-1 is presented in theses by Joshua Lake and Nakul Ravikumar at Clemson University on the development of strain indicating screws.[205-206]

From the above MATLAB script, the following equations were used to calculate color ratios:

$$B' = \frac{Blue - Blue_{min.}}{Blue_{max.} - Blue_{min.}} \qquad \text{Equation (1)}$$

$$R' = \frac{Red - Red_{min.}}{Red_{max.} - Red_{min.}} \qquad \text{Equation (2)}$$

$$Color\ Ratio = \frac{B'}{(R' + B')} \qquad \text{Equation (3)}$$

Appendix B

Design of Motorized Stage Fixture and Characterization of Stage Backlash

In order to attach the spectral rulers to the motorized stage used to control the position of the encoder strip, a metal fixture was designed to clamp to the motorized stage. Dimensions of the fixture are provided in the drawings below. The fixture contains seven pieces machined in aluminum. The assembled fixtures is photographed in **figure B -1,** with each design piece indicated.

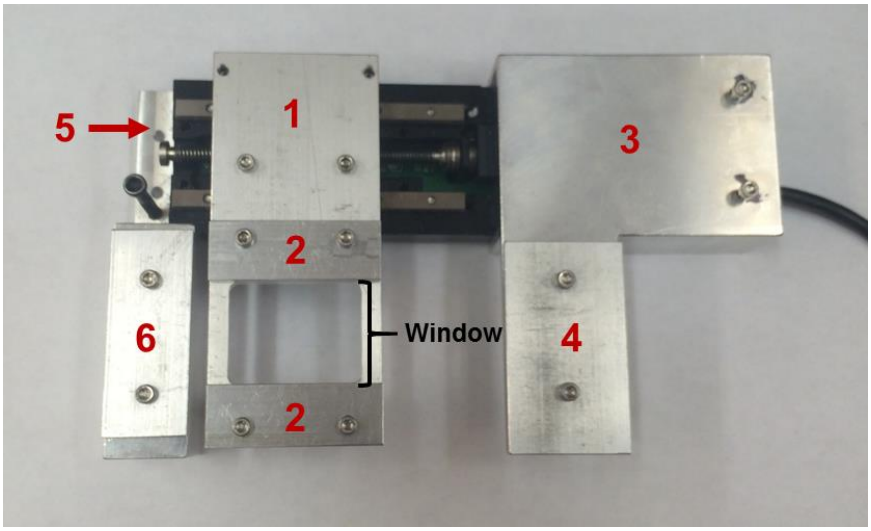

Figure B-1: Photograph of the motorized stage fixture for spectral ruler attachment. The encoder strip is placed across the window in piece 1 and is held in place on either side by piece 2. The window allows for the excitation source to illuminate the sensor, and the resultant emission to be collected by the microscope objective. The analyzer mask extends out of the spectral ruler housing on each end and is held in a stationary position under clamps 4 and 6.

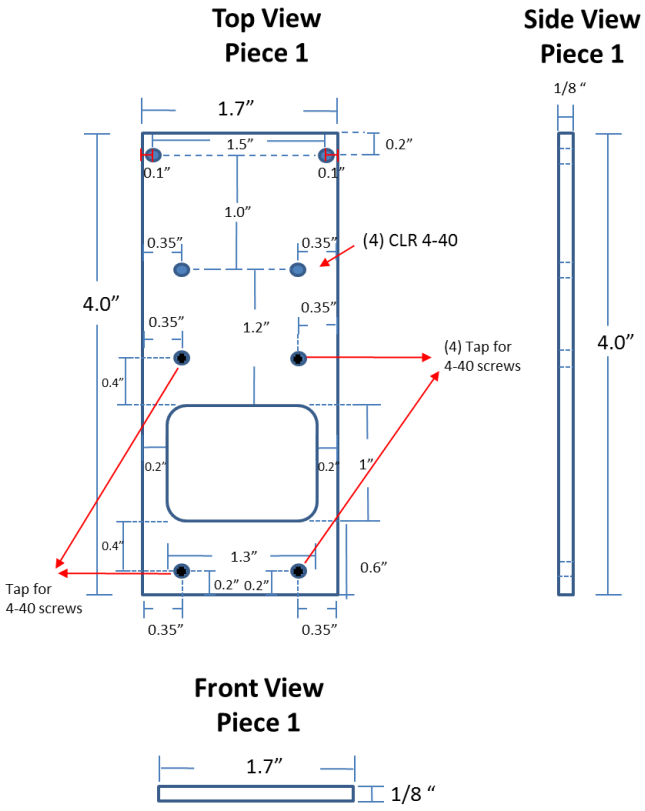

Figure B-2: Schematic of piece 1 for motorized stage fixture.

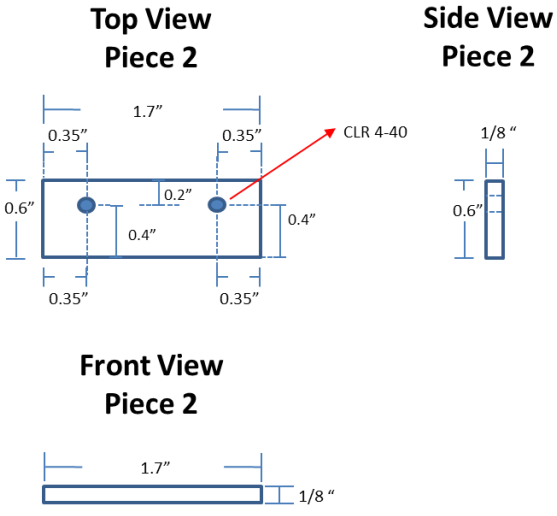

Figure B-3: Schematic of piece 2 for motorized stage fixture. Two of piece 2 are required for assembly.

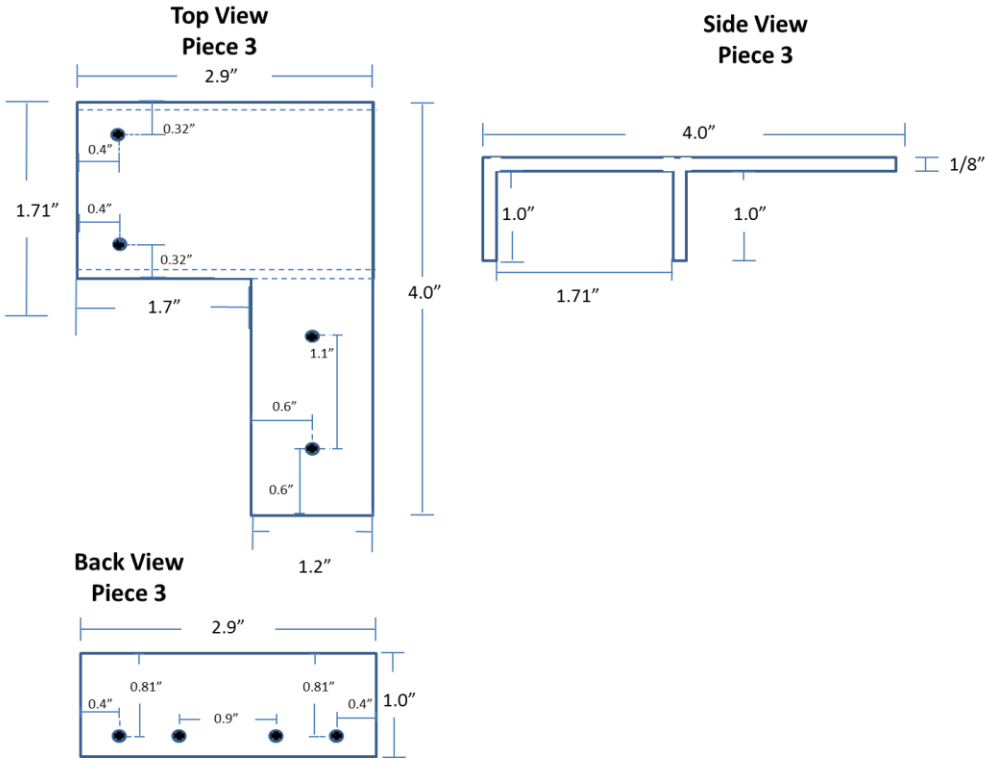

Figure B-4: Schematic of piece 3 for motorized stage fixture.

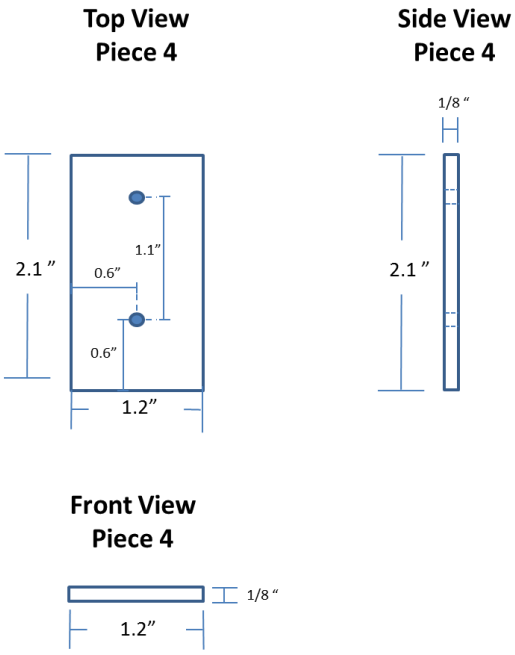

Figure B-5: Schematic of piece 4 for motorized stage fixture.

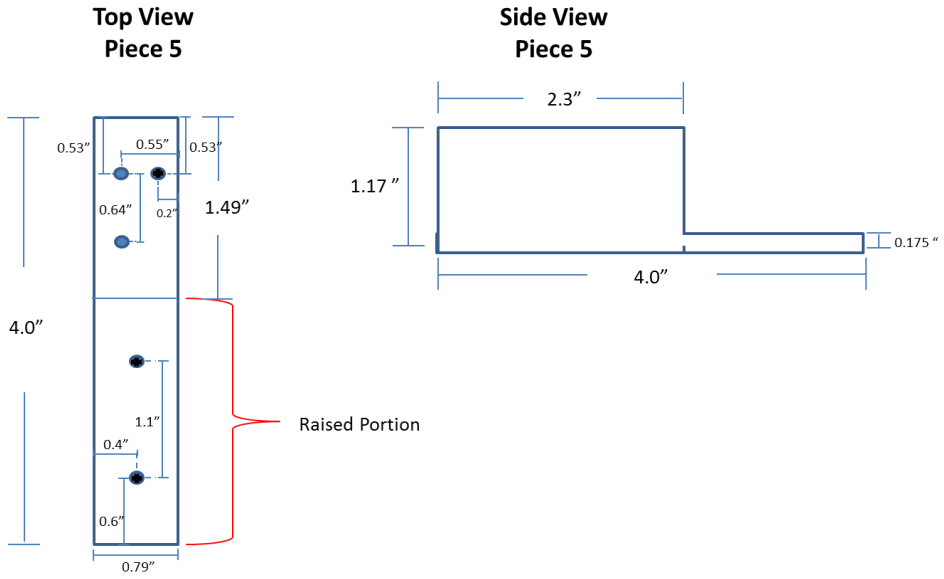

Figure B-6: Schematic of piece 5 for motorized stage fixture.

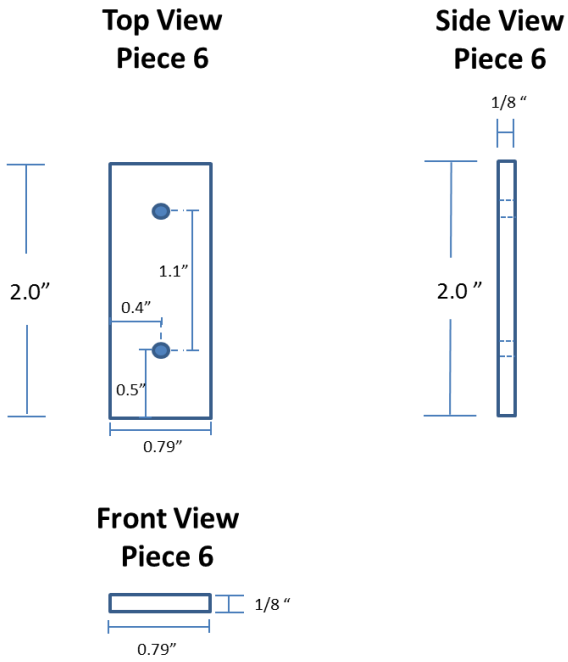

Figure B-7: Schematic of piece 6 for motorized stage fixture.

In order to correct displacement measurements for the inherent backlash of the motorized stage, the motion of the motorized stage was characterized using photography. Images of a screw on the motorized stage fixture were acquired for different step sizes (10 µm, 15 µm, 25 µm, 35 µm, 50 µm, and 100 µm). To measure displacement after a direction change, the motorized stage was advanced one position then reversed a single position. This stage motion was repeated and a total of 9 positions investigated; at each position a single photograph was acquired. To study displacements in a single direction, the stage was advanced three consecutive positions, with an image acquired at each, before reversal of the direction. A total of 12 images were acquired for this pattern. During analysis of stage motion in a single direction, measurements corresponding to change in direction were excluded.

All motorized stage images were imported into MATLAB and image correlation was performed. MATLAB script for the analysis is provided below along with example images for two photographs from the analysis and a plot of the autocorrelation function for the images.

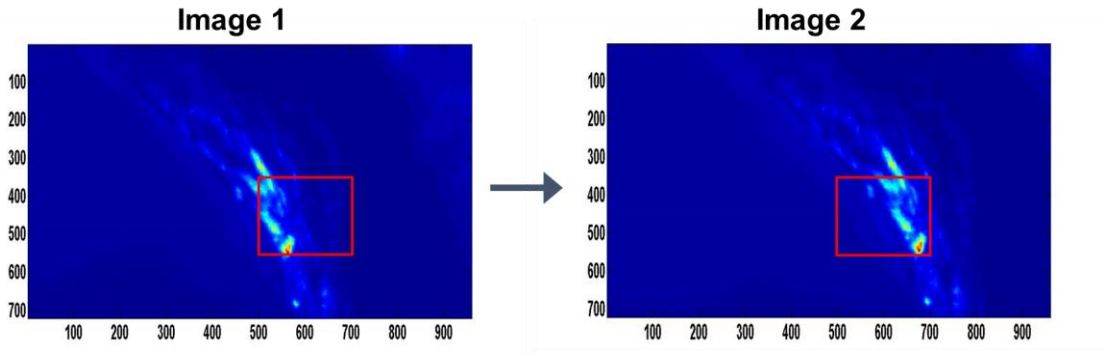

Figure B-8: Two consecutive images of a screw on the motorized stage fixture with correlated pixel regions highlighted in the red boxes (x-values 500:700 and y-values 350:550). Between the photos, a 100 micron displacement of the motorized stage was performed.

MATLAB Code for Image Correlation

```
imagesc(imread('1.tif'));
figure
imagesc(imread('2.tif'));
picture2=imread('1.tif');
picture3=imread('2.tif');
for i=1:4, for j=1:400,
c2(i,j)=corr2(picture2(350:550,500:700),picture3(350-2+i:550-2+i,500-
200+j:700-200+j));end; display(i); end;
figure;plot (c2');
```

Figure B-9: MATLAB script for image correlation. Highlighted regions correspond to the variable x and y coordinates than can be input.

Figure B-10 shows the correlation plot for the above two images. The max correlation (0.9911) between the photos fell at a pixel value of 314. According to the MATLAB code, the pictures were offset by 200 pixels. After applying this correction factor, it was determined that the stage moved a distance of 114 pixels in the x-direction.

The number of pixels moved was converted to a physical distance. Prior to photo analysis, an image of a target was acquired and it was determined that one pixel was equal to 0.726 µm.

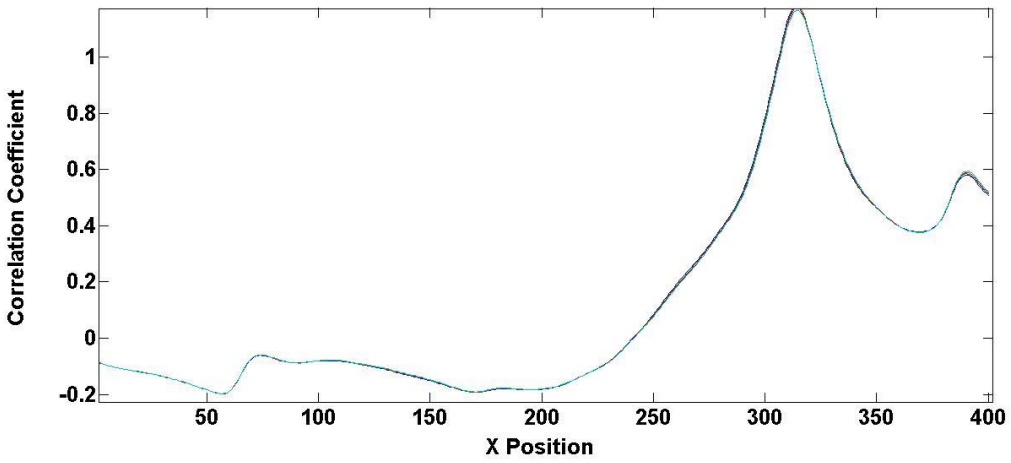

Figure B-10: Correlation coefficient versus x-coordinate for the images shown in B-8.

A summary of the backlash correction values and displacement measurements for a continuous direction are provided in **table B-1** below.

Summary	10	20	25	35	50	100
Direction Change	2.4 ± 0.6	6.02 ± 0.9	14.5 ± 0.7	24.3 ± 1.1	32.2 ± 2.3	81.3 ± 3.3
Backlash	7.6	14.0	10.5	12.2	17.8	18.7
Single Direction	7.1 ± 1.1	18.4 ± 1.2	24.2 ± 1.0	34.5 ± 0.8	49.8 ± 1.6	100.0 ± 1.5

Table B-1: Table summarizing the motorized stage characterization. The row labeled direction change corresponds to images acquired in a forward – reverse – forward-

reverse pattern. Backlash for each step size is highlighted in orange. Step size reproducibility for a single direction is also provided.

Additionally, backlash of the motorized stage was determined from our small displacement spectral measurements. It was found that backlash calculated in this manner, was greater than the backlash from image correlation. The backlash was determined to be 20.1 μm. To calculate the backlash, the average spectral ratio difference between positions 1 and 2 for each stage step size were subtracted and plotted versus the motorized stage step size. The values were fit to a straight line and the x-intercept was calculated. The graphs below show an example of results from a fluorescence quantum dot sensor.

Discrepancy between the backlash calculated from image correlation and from the spectral measurements may be attributed to several factors including friction between the analyzer mask and encoder strip or backlash as a result of buckling of the analyzer mask. Additionally, we have selected to fit the data from the luminescent study to a straight line; resulting in a single backlash value. From the image correlation we observed that the backlash is a function of the programmed stage step size.

For all measurements reported in this dissertation, backlash corrections were applied using values determined from image correlation. These values offer an independent form of measurement that are based solely on the motorized stage and neglect any contribution from the sensor. In the future, a detailed study of the backlash of the stage with no software correction applied should be examined. A preliminary look at

this case, suggested that the backlash was less than was observed with the default backlash correction of 0.050 mm.

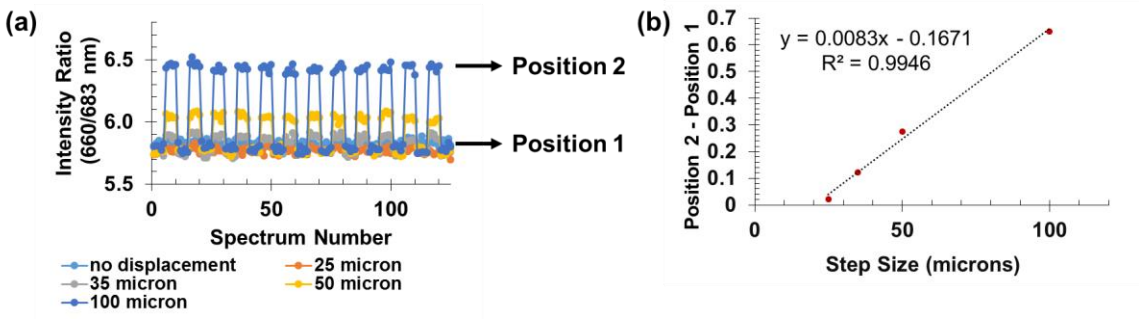

Figure B-11: (a) Spectral ratio values vs. spectrum number for various programmed stage step sizes. Positions 1 and 2 are highlighted for the 100 micron stage step size. (b) Plot of average spectral ratio difference vs. stage step size. The x-intercept, 20.1 µm, gives the backlash correction factor for the measurements.

Appendix C

MATLAB Code for the Removal of Tissue Autofluorescence from Spectral Acquisitions

```
open svddat
minv2=[sens(:,[4 16]) chick(:,2)];
scorest=(minv2\t_sens(:,[2:43])).';
figure; plot(scorest);
for i=1:42, t_sens_c(:,i+1)=t_sens(:,i+1)-scorest(i,3)*chick(:,2); end;
t_sens_c(:,1)=t_sens(:,1);
figure; splot(t_sens_c);
figure; splot(t_sens);
```

Figure C-1: MATLAB code for the removal of tissue autofluorescence.

Graphs provided below for determination of score values. Data worksheet labeled sens, contains all spectra for the fluorescence spectral ruler data without tissue provided in chapter 2, **figure 2.3a-b**, and t_sens all spectra for data through tissue, figure **2.3d-e**. Spectra 4 and 16 were selected from the data set in the absence of tissue because they represent the two extreme positions of the spectral encoder relative to the analyzer mask. Spectrum 4 is representative of the QPP 645 quantum dots and spectrum 16 is representative of the QPP 665 quantum dots. Both spectra are provided in **figure C-2** below. Also shown, in **figure C-3**, is the chicken spectrum (2) used in this evaluation.

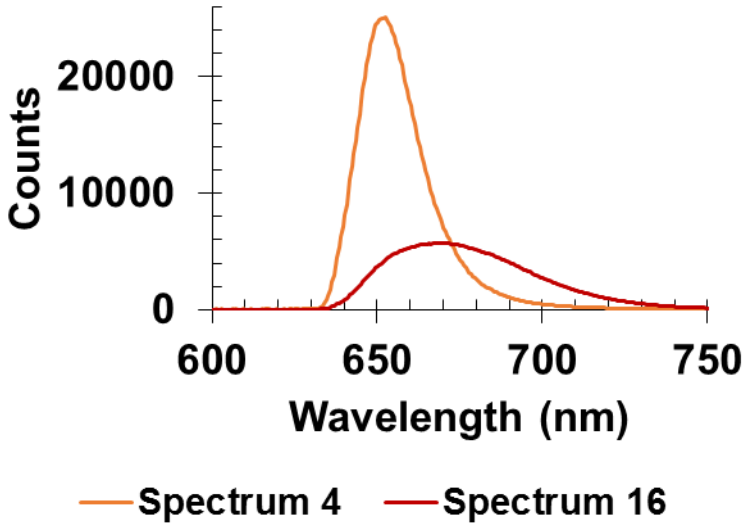

Figure C-2: Emission spectra 4 (QPP 645) and 16 (QPP 665) used to determine scores for the tissue autofluorescence corrections described above.

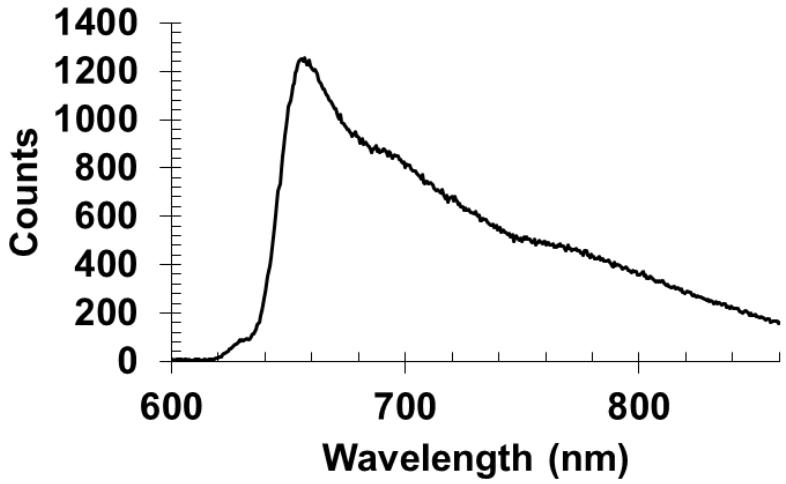

Figure C-3: Fluorescence emission spectrum of tissue breast chicken under 633 nm excitation and the same acquisition parameters as the spectra in **figure C-2**.

Appendix D

SI Programmer Stepper Motor Controls for Magnetic Modulation Experiments

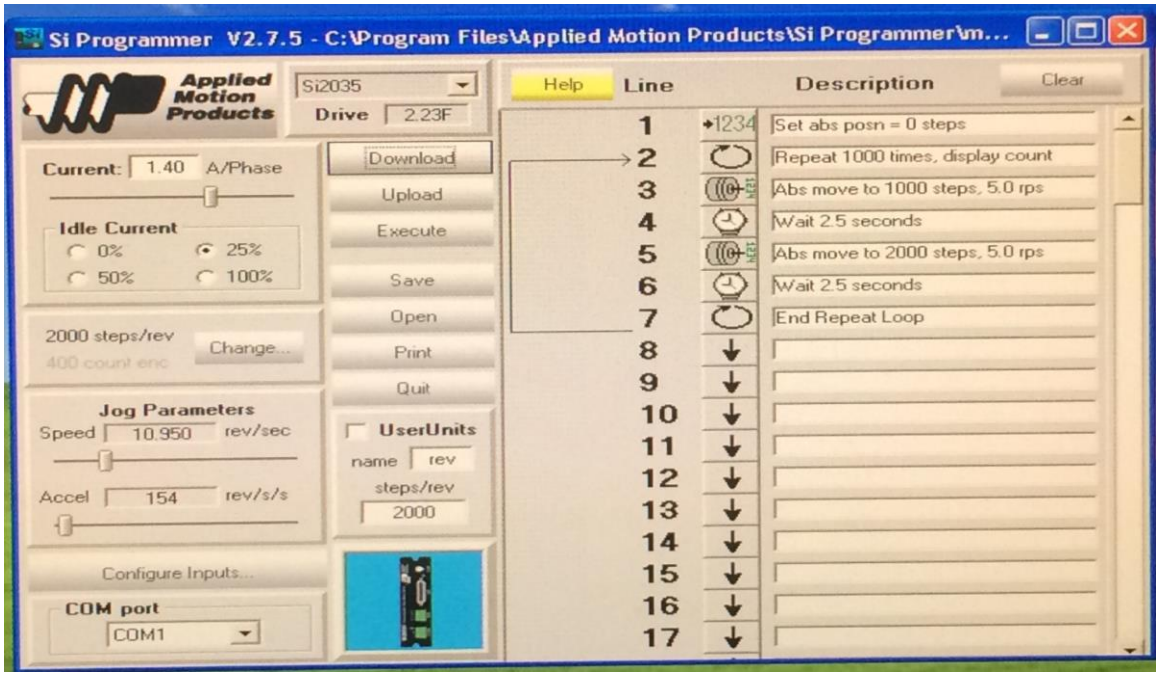

Figure D-1: Photograph displaying the programmed rotation of the external magnet for the pH studies presented in chapter 4 using SI programmer. In the absence of tissue, the wait time was programmed to be 2.5 seconds (lines 4 and 6). In the presence of tissue, the wait time was adjusted to 16 seconds, while all other line descriptions were left unmodified.

Appendix E

Mechanical Testing of Spectral Rulers Using Digital Photography

This dissertation has highlighted the importance of understanding the stresses on implanted fixation devices and changes in load sharing between the fracture callus and the device as a fracture heals. This information is clinically relevant for determining the "end point" of fracture healing. Additionally, it may be valuable to assess hardware fatigue. Although most fixation surgeries are successful, non-union and aseptic implant loosening can occur. Orthopedic implant loosening is often difficult to detect in its early stages but is critical in order to reduce the need for revision surgery. Radiography is commonly used to detect implant loosening by observing bone resorption around the screws but the results are difficult to quantify especially for early detection. With the aim of monitoring fracture healing and hardware fatigue using our luminescent spectral rulers, described in chapters 2 and 3 this appendix demonstrates preliminary mechanical testing studies performed.

The spectral rulers used in the studies shown here do not contain luminescent materials, rather they mimic the design proposed in chapter 2 for proof of concept. The sensors use digital photography as the tracking method. We begin by showing mechanical testing of strain sensors attached to an aluminum bar and end with incorporation of our sensor into an orthopedic screw. The luminescent version of the orthopedic screw is described in our US patent, 9,179,865, "Luminescent Tension-Indicating Orthopedic Strain Gauges for Non-Invasive Measurements."[52]

Mechanical testing of spectral rulers patterned with alternating stripes of cyan and magenta dye was performed using an Instron materials testing system (MTS 810) at NASA, Langley with the assistance of Russell Wincheski. Spectral rulers with 500 µm, 200 µm, and 100 µm linewidths were attached to a 6061-T6 aluminum bar (2 inches wide, 1/8 " thick) and tensile loading was performed. A pre-load of 50 lbs was applied before loading to 2,550 lbs at a rate of 2,490 lbs per minute. At the maximum load, the position was held for a period of 30 seconds before the load was removed at the same rate as it was applied. Images of the sensors were acquired every 0.5 seconds. Images were analyzed in MATLAB and the resultant spectral ratios vs. time were plotted along with strain measured by the Instron.

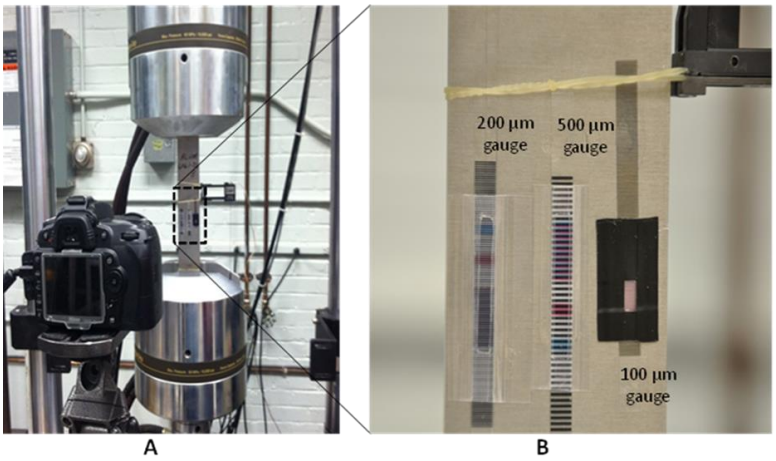

Figure E-1: (a) Photograph of experimental set-up showing position of the camera for photo acquisition relative to the test specimen in the Instron testing system. (b) Enlarged photograph of the 200 µm, 500 µm, and 100 µm linewidth strain sensor attached to the aluminum bar.

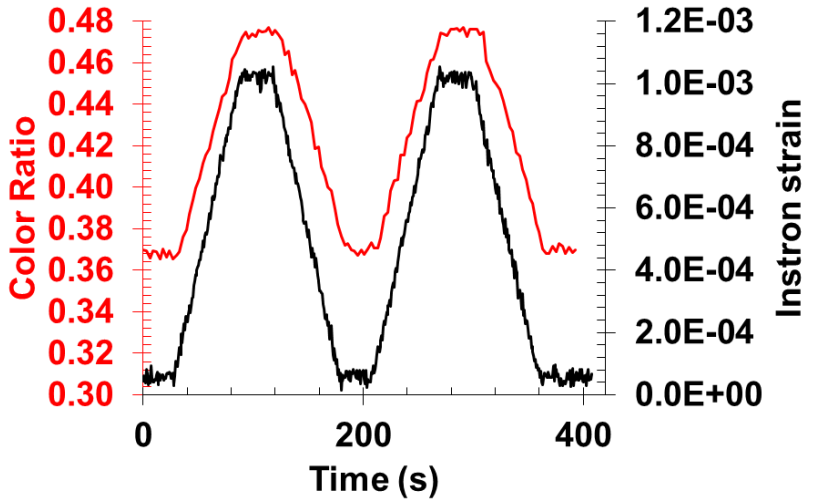

Figure E-2: Change in color ratio vs. time for the 100 micron gauge and corresponding Instron strain vs. time for a 2,500 lb ramp.

The results from this test demonstrate that changes in spectral ratio as a result of compression and extension of a metal specimen can be observed with our ruler and the response follows the expected trend. Future studies on 316 L stainless steel or titanium should be conducted in order to mimic orthopedic devices. Similar mechanical testing of our sensor is reported in "Development and Verification of a Test System to Quantify Strain of an Optical Displacement Indicator and the Design of a Strain Indicating Prototype," a thesis by Joshua Lake at Clemson University.[206] The experiment shown here includes measurements for strain sensors with a smaller linewidth and more robust encoder housing.

In addition to attachment of the spectral ruler to a fracture fixation plate or across the interfragmentary gap of a tibia fracture, the spectral ruler may also be housed in the

head of an orthopedic screw. Enclosing the sensor in the orthopedic screw head will reveal information regarding load on the fixation device and can aid in the detection of hardware fatigue.

A schematic of the sensor in the screw head is shown in **figure E-3a**. The encoder is attached to a movable wedge; the wedge is attached to a spring and the position of the wedge can be altered under tension. The screw contains a central pin that presses against the wedge. The central pin elongates under tension causing the wedge to shift to the right. During this process, the analyzer mask remains in a fixed position; therefore a change in color can be observed through the transparent windows. Prototypes of the screw have been fabricated in stainless steel and 3D printed in PLA.

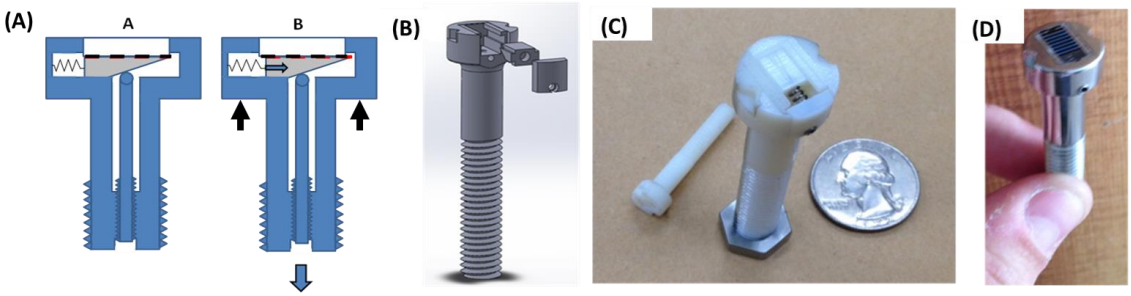

Figure E:3 (A) Schematic of the proposed tension indicating screw. The screw head contains a spectral ruler attached to a movable wedge. As the central pin in the screw elongates under tension, the pattern is displaced relative to the fixed position of the transparent windows. (B) Solidworks computer model. (C) 3D printed PLA screw prototypes. (D) A 500 μm linewidth sensor attached to a 316L stainless steel prototype. Figure was adapted from references 205 and 206.

As a demonstration of the screw function, 500 µm linewidth strain sensors have been incorporated into the prototypes and color change visible through the transparent mask monitored as a function of position. The central pin in the screw was rotated in 45° turns and the color ratio monitored by photography. The experiment in Figure E-4 d-f was performed in collaboration with Joshua Lake and the results are also presented in his thesis on the development of a strain indicating prototype.[206]

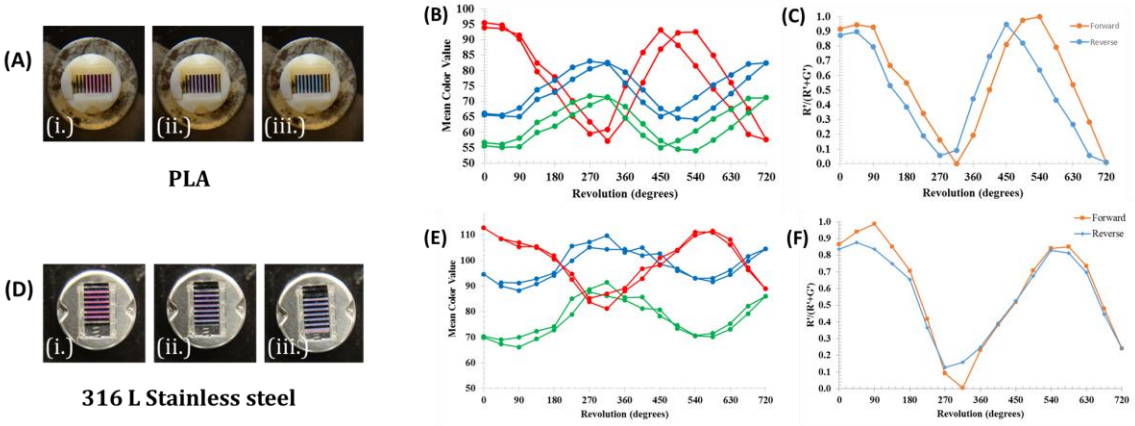

Figure E-4: The central pin in a prototype screw was rotated in 45 ° turns 2 complete revolutions in the forward and reverse directions. (A) and (D) show images of the screw in (i.) the initial position, (ii.) after 1 revolution and (iii.) after 2 revolutions. (B) and (E) show the average mean color (red, green, and blue) for three images acquired at each position. (C) and (F) show the change in color ratio as a function of screw rotation in degrees. Figure E-4 (D) – (F) was adapted from reference 206.

To demonstrate proof of concept for use in a clinical setting, a luminescent spectral ruler similar to the XEOL sensors presented in chapter 2 was inserted into a tension indicating screw prototype. The prototype was similar in design to the screw shown above, however was prepared from a cannulated orthopedic screw to miniaturize the dimensions. For a detailed description of the screw design and mechanical characterization, see our collaborative work described in "Development and Validation of an Optically-Based Strain Measuring Orthopedic Screw for Fracture Fixation Implants," a thesis by Nakul Ravikumar in the Clemson bioengineering department.[205] Briefly, the spectral ruler inserted was prepared to contain 250 micron linewidths using a laser cutter (Epilog Laser, Golden, CO, USA). Both the analyzer and mask were cut from Boise Aspen® copy paper and dyed according to their respective layer (5 µl of bromocresol purple dye for the encoder and 5 µl of black printer ink for the mask). The encoder was overlaid upon a Gd_2O_2S:Eu film containing 5 µl of a 500 mg/ml particle solution in (5 mg/ml) carboxymethyl cellulose sodium. The assembled sensor was attached to the wedge in the screw prototype with double sided tape. A schematic of the assembled sensor and working principle of the spectral ruler are provided in figure **E-5**. The position of the screw's inner rod was attached to a stepper motor with a 3D printed adapter. The rod was rotated in 200 step increments (3.6 °step size) and 5 spectra recorded at each position. The sample was excited with an x-ray source (50 kV, 600 µA) and the portable collection system presented in chapter 2, **figure 2.8** was utilized for signal collection. A schematic of the experimental set-up and the experimental results are presented below, **figure E-6**, for the sensor response without tissue and through 6 mm of chicken breast

tissue. A secondary axis, showing the horizontal displacement of the screw wedge is plotted. Each 3.6 ° rotation is equivalent to a 7.15 micron change in encoder position, assuming a wedge angle of 35 °.

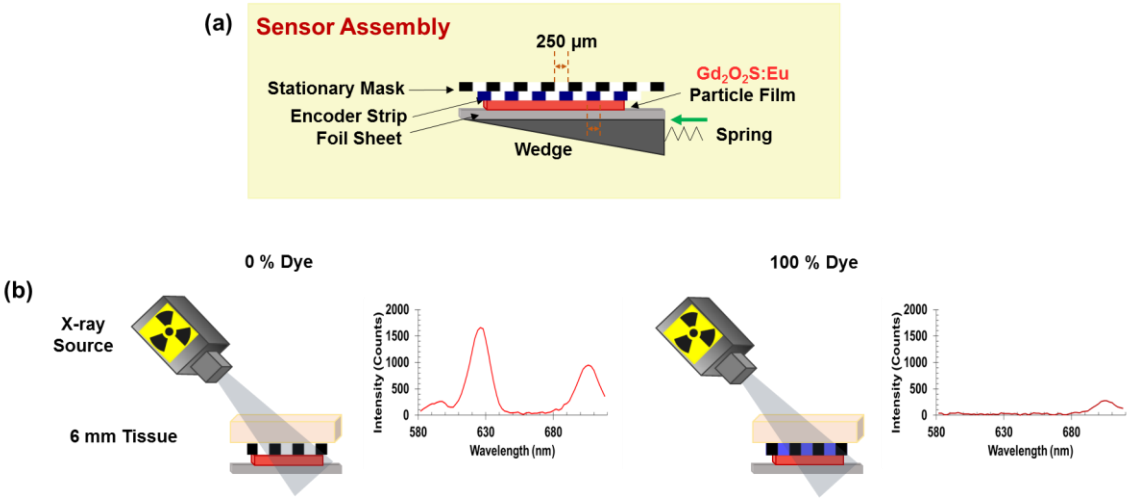

Figure E-5: (a) Schematic showing the assembled spectral ruler attached to the upper surface of the screw wedge. (b) Example spectra showing the signal decrease of the 625 nm particle emission peak with increasing dye visible through the mask.

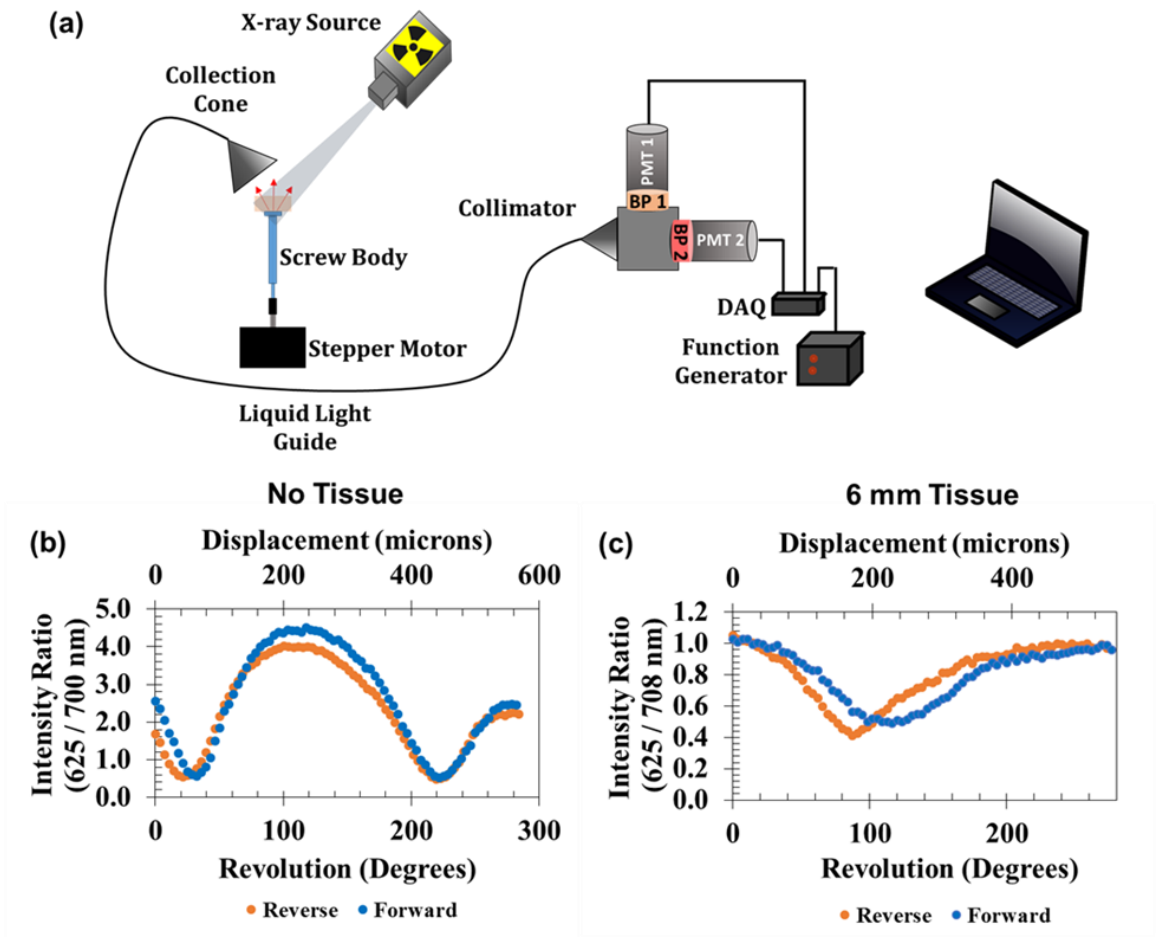

Figure E-6: (a) Diagram of experimental set-up. An XEOL spectral ruler was attached to the movable wedge of a tension indicating orthopedic screw prototype. (b) Ruler response to changes in wedge position in the absence and (c) through 6 mm thick chicken breast tissue. The position of the wedge was modulated by rotating the central rod in 3.6 ° rotations.

The results in **figure E-6** show that change in color can be observed through tissue with our spectral ruler housed in the screw. However, the spectral ratios in the presence and absence of tissue vary. We hypothesize that this difference is a result of the

housing design. There is little to no space between the encoder and mask in the sensors in chapter 2, however, in the prototype screw, the layers are not flush. This may result in an angle dependency that is magnified as the tissue thickness is increased. Further testing will be performed in the future to address this hypothesis. Although, there is a discrepancy, the general working principle of the luminescent screw has been demonstrated.

REFERENCES

1. Weinstein, S. L., 2000–2010: The Bone and Joint Decade. *The Journal of Bone & Joint Surgery* **2000**, *82*, 1-3.

2. Widmer, A. F., New Developments in Diagnosis and Treatment of Infection in Orthopedic Implants. *Clinical Infectious Diseases* **2001**, *33*, S94-S106.

3. Burge, R.; Dawson-Hughes, B.; Solomon, D. H.; Wong, J. B.; King, A.; Tosteson, A., Incidence and Economic Burden of Osteoporosis-Related Fractures in the United States, 2005–2025. *Journal of Bone and Mineral Research* **2007**, *22*, 465-475.

4. Darouiche, R. O., Treatment of Infections Associated with Surgical Implants. *New England Journal of Medicine* **2004**, *350*, 1422-1429.

5. Trampuz, A.; Zimmerli, W., Diagnosis and Treatment of Infections Associated with Fracture-Fixation Devices. *Injury* **2006**, *37*, S59-S66.

6. Ehrlich, G. D.; Stoodley, P.; Kathju, S.; Zhao, Y.; McLeod, B. R.; Balaban, N.; Hu, F. Z.; Sotereanos, N. G.; Costerton, J. W.; Stewart, P. S., Engineering Approaches for the Detection and Control of Orthopaedic Biofilm Infections. *Clinical orthopaedics and related research* **2005**, 59.

7. Augat, P.; Faschingbauer, M.; Seide, K.; Tobita, K.; Callary, S. A.; Solomon, L. B.; Holstein, J. H., Biomechanical Methods for the Assessment of Fracture Repair. *Injury* **2014**, *45 Suppl 2*, S32-8.

8. Augat, P.; Morgan, E. F.; Lujan, T. J.; MacGillivray, T. J.; Cheung, W. H., Imaging Techniques for the Assessment of Fracture Repair. *Injury* **2014**, *45 Suppl 2*, S16-22.

9. Bottlang, M.; Augat, P., The Bottleneck of Evidence-Based Fracture Care. *Injury* **2014**, *45, Supplement 2*, S1-S2.

10. Burny, F.; Donkerwolcke, M.; Moulart, F.; Bourgois, R.; Puers, R.; Van Schuylenbergh, K.; Barbosa, M.; Paiva, O.; Rodes, F.; Bégueret, J., Concept, Design and Fabrication of Smart Orthopedic Implants. *Medical engineering & physics* **2000**, *22*, 469-479.

11. Wade, R.; Richardson, J., Outcome in Fracture Healing: A Review. *Injury* **2001**, *32*, 109-114.

12. Solomon, L. B.; Stevenson, A. W.; Callary, S. A.; Sullivan, T. R.; Howie, D. W.; Chehade, M. J., The Accuracy and Precision of Radiostereometric Analysis in Monitoring Tibial Plateau Fractures. *Acta orthopaedica* **2010**, *81*, 487-494.

13. Chehade, M. J.; Solomon, L. B.; Callary, S. A.; Benveniste, S. H.; Pohl, A. P.; Howie, D. W., Differentially Loaded Radiostereometric Analysis to Monitor Fracture Stiffness: A Feasibility Study. *Clinical Orthopaedics and Related Research®* **2009**, *467*, 1839-1847.

14. Lanyon, L.; Hampson, W.; Goodship, A.; Shah, J., Bone Deformation Recorded in Vivo from Strain Gauges Attached to the Human Tibial Shaft. *Acta Orthopaedica* **1975**, *46*, 256-268.

15. Burr, D.; Milgrom, C.; Fyhrie, D.; Forwood, M.; Nyska, M.; Finestone, A.; Hoshaw, S.; Saiag, E.; Simkin, A., In Vivo Measurement of Human Tibial Strains During Vigorous Activity. *Bone* **1996**, *18*, 405-410.

16. Seide, K.; Aljudaibi, M.; Weinrich, N.; Kowald, B.; Jürgens, C.; Müller, J.; Faschingbauer, M., Telemetric Assessment of Bone Healing with an Instrumented Internal Fixator a Preliminary Study. *Journal of Bone & Joint Surgery, British Volume* **2012**, *94*, 398-404.

17. Schneider, E.; Michel, M. C.; Genge, M.; Zuber, K.; Ganz, R.; Perren, S. M., Loads Acting in an Intramedullary Nail During Fracture Healing in the Human Femur. *Journal of biomechanics* **2001**, *34*, 849-857.

18. Burny, F.; Donkerwolcke, M.; Bourgois, R.; Domb, M.; Saric, O., Twenty Years Experience in Fracture Healing Measurement with Strain Gauges. *Orthopedics* **1984**, *7*, 1823-1826.

19. Richardson, J.; Cunningham, J.; Goodship, A.; O'connor, B.; Kenwright, J., Measuring Stiffness Can Define Healing of Tibial Fractures. *Journal of Bone & Joint Surgery, British Volume* **1994**, *76*, 389-394.

20. D'Lima, D.; Fregly, B.; Colwell, C., Implantable Sensor Technology: Measuring Bone and Joint Biomechanics of Daily Life in Vivo. *Arthritis research & therapy* **2013**, *15*, 203.

21. Yang, P.; Bruggemann, G.; Rittweger, J., What Do We Currently Know from in Vivo Bone Strain Measurements in Humans. *J Musculoskelet Neuronal Interact* **2011**, *11*, 8-20.

22. The Strain Gage. http://www.omega.com/literature/transactions/volume3/strain.html.

23. Stress-Strain Relationships. fp.optics.arizona.edu/optomech/references/OPTI.../OPTI_222_W4.pdf.

24. Roylance, D., *Mechanical Properties of Materials*; MIT, 2008, p 128.

25. Bhopate, D. P.; Mahajan, P. G.; Garadkar, K. M.; Kolekar, G. B.; Patil, S. R., Pyrene Nanoparticles as a Novel Fret Probe for Detection of Rhodamine 6g: Spectroscopic Ruler for Textile Effluent. *RSC Adv.* **2014**, *4*, 63866-63874.

26. Bourret, G. R.; Ozel, T.; Blaber, M.; Shade, C. M.; Schatz, G. C.; Mirkin, C. A., Long-Range Plasmophore Rulers. *Nano Lett* **2013**, *13*, 2270-5.

27. Chatterjee, S.; Lee, J. B.; Valappil, N. V.; Luo, D.; Menon, V. M., Investigating the Distance Limit of a Metal Nanoparticle Based Spectroscopic Ruler. *Biomedical optics express* **2011**, *2*, 1727-1733.

28. dos Remedios, C. G.; Moens, P. D. J., Fluorescence Resonance Energy Transfer Spectroscopy Is a Reliable "Ruler" for Measuring Structural Changes in Proteins: Dispelling the Problem of the Unknown Orientation Factor. *Journal of Structural Biology* **1995**, *115*, 175-185.

29. Hill, R. T.; Kozek, K. M.; Hucknall, A.; Smith, D. R.; Chilkoti, A., Nanoparticle-Film Plasmon Ruler Interrogated with Transmission Visible Spectroscopy. *ACS Photonics* **2014**, *1*, 974-984.

30. Morgner, F.; Geissler, D.; Stufler, S.; Butlin, N. G.; Lohmannsroben, H. G.; Hildebrandt, N., A Quantum-Dot-Based Molecular Ruler for Multiplexed Optical Analysis. *Angew Chem Int Ed Engl* **2010**, *49*, 7570-4.

31. Rabenstein, M. D.; Shin, Y.-K., Determination of the Distance between Two Spin Labels Attached to a Macromolecule. *Proceedings of the National Academy of Sciences* **1995**, *92*, 8239-8243.

32. Ray, P. C.; Fan, Z.; Crouch, R. A.; Sinha, S. S.; Pramanik, A., Nanoscopic Optical Rulers Beyond the Fret Distance Limit: Fundamentals and Applications. *Chem Soc Rev* **2014**, *43*, 6370-404.

33. Sahoo, H.; Roccatano, D.; Hennig, A.; Nau, W. M., A 10-Å Spectroscopic Ruler Applied to Short Polyprolines. *Journal of the American Chemical Society* **2007**, *129*, 9762-9772.

34. Samanta, A.; Zhou, Y.; Zou, S.; Yan, H.; Liu, Y., Fluorescence Quenching of Quantum Dots by Gold Nanoparticles: A Potential Long Range Spectroscopic Ruler. *Nano Lett* **2014**, *14*, 5052-7.

35. Sarkar, R.; Shaw, A. K.; Narayanan, S. S.; Dias, F.; Monkman, A.; Pal, S. K., Direct Observation of Protein Folding in Nanoenvironments Using a Molecular Ruler. *Biophys Chem* **2006**, *123*, 40-8.

36. Shaw, A. K.; Sarkar, R.; Pal, S. K., Direct Observation of DNA Condensation in a Nano-Cage by Using a Molecular Ruler. *Chemical Physics Letters* **2005**, *408*, 366-370.

37. Singh, A. K.; Khan, S. A.; Fan, Z.; Demeritte, T.; Senapati, D.; Kanchanapally, R.; Ray, P. C., Development of a Long-Range Surface-Enhanced Raman Spectroscopy Ruler. *J Am Chem Soc* **2012**, *134*, 8662-9.

38. Sönnichsen, C.; Reinhard, B. M.; Liphardt, J.; Alivisatos, A. P., A Molecular Ruler Based on Plasmon Coupling of Single Gold and Silver Nanoparticles. *Nature biotechnology* **2005**, *23*, 741-745.

39. Stryer, L., Fluorescence Energy Transfer as a Spectroscopic Ruler. *Annu Rev Biochem* **1967**, *47*, 819-846.

40. Stryer, L.; Haugland, R. P., Energy Transfer: A Spectroscopic Ruler. *Proceedings of the National Academy of Sciences of the United States of America* **1967**, *58*, 719.

41. Zubritskaya, I.; Lodewijks, K.; Maccaferri, N.; Mekonnen, A.; Dumas, R. K.; Akerman, J.; Vavassori, P.; Dmitriev, A., Active Magnetoplasmonic Ruler. *Nano Lett* **2015**, *15*, 3204-11.

42. Lee, S. E.; Chen, Q.; Bhat, R.; Petkiewicz, S.; Smith, J. M.; Ferry, V. E.; Correia, A. L.; Alivisatos, A. P.; Bissell, M. J., Reversible Aptamer-Au Plasmon Rulers for Secreted Single Molecules. *Nano letters* **2015**, *15*, 4564-4570.

43. Lermusiaux, L.; Maillard, V.; Bidault, S., Widefield Spectral Monitoring of Nanometer Distance Changes in DNA-Templated Plasmon Rulers. *ACS nano* **2015**, *9*, 978-990.

44. Liu, N.; Hentschel, M.; Weiss, T.; Alivisatos, A. P.; Giessen, H., Three-Dimensional Plasmon Rulers. *Science* **2011**, *332*, 1407-1410.

45. Rostalski, J.; Quinten, M., Effect of a Surface Charge on the Halfwidth and Peak Position of Cluster Plasmons in Colloidal Metal Particles. *Colloid and Polymer Science* **1996**, *274*, 648-653.

46. Clamme, J. P.; Deniz, A. A., Three-Color Single-Molecule Fluorescence Resonance Energy Transfer. *Chemphyschem* **2005**, *6*, 74-7.

47. Henry, A.-I.; Bingham, J. M.; Ringe, E.; Marks, L. D.; Schatz, G. C.; Van Duyne, R. P., Correlated Structure and Optical Property Studies of Plasmonic Nanoparticles. *The Journal of Physical Chemistry C* **2011**, *115*, 9291-9305.

48. Alexeev, V. L.; Das, S.; Finegold, D. N.; Asher, S. A., Photonic Crystal Glucose-Sensing Material for Noninvasive Monitoring of Glucose in Tear Fluid. *Clinical Chemistry* **2004**, *50*, 2353-2360.

49. Asher, S. A.; Baca, J. T., Tear Fluid Photonic Crystal Contact Lens Noninvasive Glucose Sensors. In *Handbook of Optical Sensing of Glucose in Biological Fluids and Tissues*, Taylor & Francis: 2008; pp 387-417.

50. Ben-Moshe, M.; Alexeev, V. L.; Asher, S. A., Fast Responsive Crystalline Colloidal Array Photonic Crystal Glucose Sensors. *Analytical chemistry* **2006**, *78*, 5149-5157.

51. Muscatello, M. M.; Asher, S. A., Poly(Vinyl Alcohol) Rehydratable Photonic Crystal Sensor Materials. *Adv Funct Mater* **2008**, *1186*, 18-8.

52. Anker, J.; Rogalski, M.; Anderson, D.; Heath, J. Luminescent Tension-Indicating Orthopedic Strain Gauges for Non-Invasive Measurements through Tissue. 9,179,865, 2015.

53. Ingle Jr, J. D.; Crouch, S. R., Spectrochemical Analysis. **1988**.

54. Harris, D. C., *Quantitative Chemical Analysis*, Seventh Edition ed.; W. H. Freeman and Company: New York, 2007.

55. Lakowicz, J. R., *Principles of Fluorescence Spectroscopy*; Springer Science & Business Media, 2013.

56. Boens, N.; Qin, W.; Basaric, N.; Hofkens, J.; Ameloot, M.; Pouget, J.; Lefèvre, J.-P.; Valeur, B.; Gratton, E.; VandeVen, M., Fluorescence Lifetime Standards for Time and Frequency Domain Fluorescence Spectroscopy. *Analytical chemistry* **2007**, *79*, 2137-2149.

57. Chen, H.; Rogalski, M. M.; Anker, J. N., Advances in Functional X-Ray Imaging Techniques and Contrast Agents. *Physical Chemistry Chemical Physics* **2012**, *14*, 13469-13486.

58. Rogalski, M. M. N., K. V. T.; Anker, J. N. X-Ray Vision for Molecules. http://the-briefing.com/x-ray-vision-for-molecules/.

59. Rodnyi, P. A., Efficiency and Yield Spectra of Inorganic Scintillates. *Radiation Measurements* **1998**, *29*, 235-242.

60. Benitez, E. L.; Husk, D. E.; Schnatterly, S. E.; Tarrio, C., A Surface Recombination Model Applied to Large Features in Inorganic Phosphor Efficiency

Measurements in the Soft X-Ray Region. *Journal of Applied Physics* **1991**, *70*, 3256-3260.

61. Blasse, G., Scintillator Materials. *Chemistry of Materials* **1994**, *6*, 1465-1475.

62. Wang, F.; Raval, Y.; Tzeng, T. R. J.; Anker, J. N., X-Ray Excited Luminescence Chemical Imaging of Bacterial Growth on Surfaces Implanted in Tissue. *Advanced healthcare materials* **2015**, *4*, 903-910.

63. Chen, H.; Longfield, D. E.; Varahagiri, V. S.; Nguyen, K. T.; Patrick, A. L.; Qian, H.; VanDerveer, D. G.; Anker, J. N., Optical Imaging in Tissue with X-Ray Excited Luminescent Sensors. *Analyst* **2011**, *136*, 3438-45.

64. Chen, H.; Patrick, A. L.; Yang, Z.; VanDerveer, D. G.; Anker, J. N., High-Resolution Chemical Imaging through Tissue with an X-Ray Scintillator Sensor. *Analytical chemistry* **2011**, *83*, 5045-5049.

65. Auzel, F., Upconversion and Anti-Stokes Processes with F and D Ions in Solids. *Chemical reviews* **2004**, *104*, 139-174.

66. DaCosta, M. V.; Doughan, S.; Han, Y.; Krull, U. J., Lanthanide Upconversion Nanoparticles and Applications in Bioassays and Bioimaging: A Review. *Anal Chim Acta* **2014**, *832*, 1-33.

67. Wang, F.; Liu, X., Recent Advances in the Chemistry of Lanthanide-Doped Upconversion Nanocrystals. *Chemical Society Reviews* **2009**, *38*, 976-989.

68. Ge, X.; Sun, L.; Shi, L.; Wei, R., The Modified Upconversion Nanomaterials (Ucnms) for Multimodal Imaging and Therapies. *Biomedical Spectroscopy and Imaging* **2015**, *4*, 391-412.

69. Xu, S.; Huang, S.; He, Q.; Wang, L., Upconversion Nanophosphores for Bioimaging. *TrAC Trends in Analytical Chemistry* **2015**, *66*, 72-79.

70. Li, F.; Feng, W.; Zhou, J.; Sun, Y., Lanthanide-Based Upconversion Nanophosphors for Bioimaging. In *The Chemistry of Molecular Imaging*, John Wiley & Sons, Inc: 2014; pp 299-319.

71. Wang, F.; Banerjee, D.; Liu, Y.; Chen, X.; Liu, X., Upconversion Nanoparticles in Biological Labeling, Imaging, and Therapy. *Analyst* **2010**, *135*, 1839-54.

72. Damasco, J. A.; Chen, G.; Shao, W.; Agren, H.; Huang, H.; Song, W.; Lovell, J. F.; Prasad, P. N., Size-Tunable and Monodisperse Tm(3)(+)/Gd(3)(+)-Doped Hexagonal Naybf(4) Nanoparticles with Engineered Efficient near Infrared-to-near Infrared Upconversion for in Vivo Imaging. *ACS Appl Mater Interfaces* **2014**, *6*, 13884-93.

73. Fodor, L.; Elman, M.; Ullmann, Y., *Aesthetic Applications of Intense Pulsed Light*; Springer Science & Business Media, 2010.

74. Tuchin, V. V., Light-Tissue Interactions. CRC Press: Boca Raton: 2003; pp 3.1-3.26.

75. Farrell, T. J.; Patterson, M. S.; Wilson, B., A Diffusion Theory Model of Spatially Resolved, Steady-State Diffuse Reflectance for the Noninvasive Determination of Tissue Optical Properties Invivo. *Medical physics* **1992**, *19*, 879-888.

76. Tseng, S.-H.; Bargo, P.; Durkin, A.; Kollias, N., Chromophore Concentrations, Absorption and Scattering Properties of Human Skin in-Vivo. *Optics express* **2009**, *17*, 14599-14617.

77. Ardeshirpour, Y.; Chernomordik, V.; Hassan, M.; Gandjbakhche, A. H.; Sackett, D., *In Vivo Molecular Fluorescence Imaging*; John Wiley & Sons, 2015.

78. Smith, A. M.; Mancini, M. C.; Nie, S., Bioimaging: Second Window for in Vivo Imaging. *Nat Nanotechnol* **2009**, *4*, 710-1.

79. Boas, D. A.; Brooks, D. H.; Miller, E. L.; DiMarzio, C. A.; Kilmer, M.; Gaudette, R. J.; Zhang, Q., Imaging the Body with Diffuse Optical Tomography. *Signal Processing Magazine, IEEE* **2001**, *18*, 57-75.

80. Cheong, W.-F.; Prahl, S. A.; Welch, A. J., A Review of the Optical Properties of Biological Tissues. *IEEE journal of quantum electronics* **1990**, *26*, 2166-2185.

81. Ripoll, J.; Yessayan, D.; Zacharakis, G.; Ntziachristos, V., Experimental Determination of Photon Propagation in Highly Absorbing and Scattering Media. *JOSA A* **2005**, *22*, 546-551.

82. Ntziachristos, V., Going Deeper Than Microscopy: The Optical Imaging Frontier in Biology. *Nat Meth* **2010**, *7*, 603-614.

83. Lee, C.; Kim, G. H.; Lee, S.-K., Design and Construction of a Single Unit Multi-Function Optical Encoder for a Six-Degree-of-Freedom Motion Error Measurement in an Ultraprecision Linear Stage. *Measurement Science and Technology* **2011**, *22*, 105901.

84. Stoianovici, D.; Patriciu, A.; Petrisor, D.; Mazilu, D.; Kavoussi, L., A New Type of Motor: Pneumatic Step Motor. *Mechatronics, IEEE/ASME Transactions on* **2007**, *12*, 98-106.

85. Carrica, D.; Funes, M. A.; Gonzalez, S. A., Novel Stepper Motor Controller Based on Fpga Hardware Implementation. *IEEE/ASME transactions on mechatronics* **2003**, *8*, 120-124.

86. Ye, J.; André, S.; Farge, L., Kinematic Study of Necking in a Semi-Crystalline Polymer through 3d Digital Image Correlation. *International Journal of Solids and Structures* **2015**, *59*, 58-72.

87. G'Sell, C.; Hiver, J.; Dahoun, A.; Souahi, A., Video-Controlled Tensile Testing of Polymers and Metals Beyond the Necking Point. *Journal of materials science* **1992**, *27*, 5031-5039.

88. Burgert, I.; Frühmann, K.; Keckes, J.; Fratzl, P.; Stanzl-Tschegg, S. E., Microtensile Testing of Wood Fibers Combined with Video Extensometry for Efficient Strain Detection. *Holzforschung* **2003**, *57*, 661-664.

89. Li, H.; Dou, S.-X.; Liu, Y.-R.; Li, W.; Xie, P.; Wang, W.-C.; Wang, P.-Y., Mapping Intracellular Diffusion Distribution Using Single Quantum Dot Tracking: Compartmentalized Diffusion Defined by Endoplasmic Reticulum. *Journal of the American Chemical Society* **2015**, *137*, 436-444.

90. Yildiz, A.; Selvin, P. R., Fluorescence Imaging with One Nanometer Accuracy: Application to Molecular Motors. *Accounts of chemical research* **2005**, *38*, 574-582.

91. Courty, S.; Luccardini, C.; Bellaiche, Y.; Cappello, G.; Dahan, M., Tracking Individual Kinesin Motors in Living Cells Using Single Quantum-Dot Imaging. *Nano letters* **2006**, *6*, 1491-1495.

92. Warner, J. J.; Micheli, L. J.; Arslanian, L. E.; Kennedy, J.; Kennedy, R., Scapulothoracic Motion in Normal Shoulders and Shoulders with Glenohumeral Instability and Impingement Syndrome a Study Using Moire Topographic Analysis. *Clinical orthopaedics and related research* **1992**, *285*, 191-199.

93. Takasaki, H., Moiré Topography. *Applied optics* **1970**, *9*, 1467-1472.

94. Takasaki, H., Moiré Topography from Its Birth to Practical Application. *Optics and Lasers in Engineering* **1982**, *3*, 3-14.

95. Lai, J.; Shah, B. P.; Garfunkel, E.; Lee, K. B., Versatile Fluorescence Resonance Energy Transfer-Based Mesoporous Silica Nanoparticles for Real-Time Monitoring of Drug Release. *ACS Nano* **2013**, *7*, 2741-50.

96. Bagalkot, V.; Zhang, L.; Levy-Nissenbaum, E.; Jon, S.; Kantoff, P. W.; Langer, R.; Farokhzad, O. C., Quantum Dot-Aptamer Conjugates for Synchronous Cancer Imaging, Therapy, and Sensing of Drug Delivery Based on Bi-Fluorescence Resonance Energy Transfer. *Nano letters* **2007**, *7*, 3065-3070.

97. Zou, P.; Chen, H.; Paholak, H. J.; Sun, D., Noninvasive Fluorescence Resonance Energy Transfer Imaging of in Vivo Premature Drug Release from Polymeric Nanoparticles. *Molecular pharmaceutics* **2013**, *10*, 4185-4194.

98. Maaskant, R.; Alavie, T.; Measures, R.; Tadros, G.; Rizkalla, S.; Guha-Thakurta, A., Fiber-Optic Bragg Grating Sensors for Bridge Monitoring. *Cement and Concrete Composites* **1997**, *19*, 21-33.

99. Alavie, A. T.; Maaskant, R.; Huang, S. Y.; LeBlanc, M. In *Bragg Grating Fiber Optic Sensing for Bridges and Other Structures*, Smart Structures and Materials: Second European Conference, International Society for Optics and Photonics: 1994; pp 162-167.

100. Mishra, V.; Singh, N.; Tiwari, U.; Kapur, P., Fiber Grating Sensors in Medicine: Current and Emerging Applications. *Sensors and Actuators A: Physical* **2011**, *167*, 279-290.

101. Fresvig, T.; Ludvigsen, P.; Steen, H.; Reikeras, O., Fibre Optic Bragg Grating Sensors: An Alternative Method to Strain Gauges for Measuring Deformation in Bone. *Med Eng Phys* **2008**, *30*, 104-8.

102. Mishra, V.; Singh, N.; Rai, D.; Tiwari, U.; Poddar, G.; Jain, S.; Mondal, S.; Kapur, P., Fiber Bragg Grating Sensor for Monitoring Bone Decalcification. *Orthopaedics & Traumatology: Surgery & Research* **2010**, *96*, 646-651.

103. Ren, L.; Song, G.; Conditt, M.; Noble, P. C.; Li, H., Fiber Bragg Grating Displacement Sensor for Movement Measurement of Tendons and Ligaments. *Applied optics* **2007**, *46*, 6867-6871.

104. Behrmann, G. P.; Hidler, J.; Mirotznik, M. S., *Fiber Optic Micro Sensor for the Measurement of Tendon Forces*, 2009; Vol. 70.

105. Talaia, P.; Ramos, A.; Abe, I.; Schiller, M.; Lopes, P.; Nogueira, R.; Pinto, J.; Claramunt, R.; Simões, J., Plated and Intact Femur Strains in Fracture Fixation Using Fiber Bragg Gratings and Strain Gauges. *Experimental mechanics* **2007**, *47*, 355-363.

106. Chehade, M. J.; Pohl, A. P.; Pearcy, M. J.; Nawana, N., Clinical Implications of Stiffness and Strength Changes in Fracture Healing. *Journal of Bone & Joint Surgery, British Volume* **1997**, *79*, 9-12.

107. Floerkemeier, T.; Hurschler, C.; Witte, F.; Wellmann, M.; Thorey, F.; Vogt, U.; Windhagen, H., Comparison of Various Types of Stiffness as Predictors of the Load-Bearing Capacity of Callus Tissue. *Journal of Bone & Joint Surgery, British Volume* **2005**, *87*, 1694-1699.

108. Melik, R.; Unal, E.; Perkgoz, N. K.; Santoni, B.; Kamstock, D.; Puttlitz, C.; Demir, H. V., Nested Metamaterials for Wireless Strain Sensing. *Selected Topics in Quantum Electronics, IEEE Journal of* **2010**, *16*, 450-458.

109. Hao, S.; Taylor, S. In *A Closed-Loop Inductive Power Control System for an Instrumented Strain Sensing Tibial Implant*, Engineering in Medicine and Biology Society (EMBC), 2014 36th Annual International Conference of the IEEE, IEEE: 2014; pp 6553-6556.

110. Graichen, F.; Arnold, R.; Rohlmann, A.; Bergmann, G., Implantable 9-Channel Telemetry System for in Vivo Load Measurements with Orthopedic Implants. *Biomedical Engineering, IEEE Transactions on* **2007**, *54*, 253-261.

111. Milgrom, C.; Burr, D. B.; Finestone, A. S.; Voloshin, A., Understanding the Etiology of the Posteromedial Tibial Stress Fracture. *Bone* **2015**, *78*, 11-4.

112. Al Nazer, R.; Lanovaz, J.; Kawalilak, C.; Johnston, J. D.; Kontulainen, S., Direct in Vivo Strain Measurements in Human Bone-a Systematic Literature Review. *J Biomech* **2012**, *45*, 27-40.

113. Helmchen, F.; Denk, W., Deep Tissue Two-Photon Microscopy. *Nature methods* **2005**, *2*, 932-940.

114. Wang, G.; Cong, W.; Durairaj, K.; Qian, X.; Shen, H.; Sinn, P.; Hoffman, E.; McLennan, G.; Henry, M., In Vivo Mouse Studies with Bioluminescence Tomography. *Optics Express* **2006**, *14*, 7801-7809.

115. Pejović-Milić, A.; Brito, J.; Gyorffy, J.; Chettle, D., Ultrasound Measurements of Overlying Soft Tissue Thickness at Four Skeletal Sites Suitable for in Vivo X-Ray Fluorescence. *Medical physics* **2002**, *29*, 2687-2691.

116. Wang, C.; Gao, X.; Su, X., In Vitro and in Vivo Imaging with Quantum Dots. *Anal Bioanal Chem* **2010**, *397*, 1397-415.

117. Chen, M.; He, X.; Wang, K.; Cheng, Z., Nanoparticles in Fluorescence Optical Imaging. Yang, X., Ed. Nova Science: 2013; pp 165-184.

118. Gong, H.; Peng, R.; Liu, Z., Carbon Nanotubes for Biomedical Imaging: The Recent Advances. *Adv Drug Deliv Rev* **2013**, *65*, 1951-63.

119. Liu, Z.; Yang, K.; Lee, S.-T., Single-Walled Carbon Nanotubes in Biomedical Imaging. *J. Mater. Chem.* **2011**, *21*, 586-598.

120. Welsher, K.; Sherlock, S. P.; Dai, H., Deep-Tissue Anatomical Imaging of Mice Using Carbon Nanotube Fluorophores in the Second near-Infrared Window. *Proc Natl Acad Sci U S A* **2011**, *108*, 8943-8.

121. Barone, P. W.; Baik, S.; Heller, D. A.; Strano, M. S., Near-Infrared Optical Sensors Based on Single-Walled Carbon Nanotubes. *Nat Mater* **2005**, *4*, 86-92.

122. Cherukuri, P.; Gannon, C. J.; Leeuw, T. K.; Schmidt, H. K.; Smalley, R. E.; Curley, S. A.; Weisman, R. B., Mammalian Pharmacokinetics of Carbon Nanotubes Using Intrinsic near-Infrared Fluorescence. *Proc Natl Acad Sci U S A* **2006**, *103*, 18882-6.

123. Bartholomeusz, D.; Boutté, R. W.; Andrade, J. D., Xurography: Rapid Prototyping of Microstructures Using a Cutting Plotter. *Microelectromechanical Systems, Journal of* **2005**, *14*, 1364-1374.

124. Ginger, D. S.; Zhang, H.; Mirkin, C. A., The Evolution of Dip-Pen Nanolithography. *Angewandte Chemie International Edition* **2004**, *43*, 30-45.

125. Guo, L. J., Nanoimprint Lithography: Methods and Material Requirements. *Advanced Materials* **2007**, *19*, 495-513.

126. Truskett, V. N.; Watts, M. P., Trends in Imprint Lithography for Biological Applications. *Trends Biotechnol* **2006**, *24*, 312-7.

127. Hirano, S.; Suzuki, K. T., Exposure, Metabolism, and Toxicity of Rare Earths and Related Compounds. *Environmental health perspectives* **1996**, *104*, 85.

128. Wang, F.; Raval, Y.; Chen, H.; Tzeng, T. R. J.; DesJardins, J. D.; Anker, J. N., Development of Luminescent Ph Sensor Films for Monitoring Bacterial Growth through Tissue. *Advanced healthcare materials* **2014**, *3*, 197-204.

129. https://www.semrock.com/.

130. Zhou, J.; Liu, Z.; Li, F., Upconversion Nanophosphors for Small-Animal Imaging. *Chemical Society Reviews* **2012**, *41*, 1323-1349.

131. Chen, J.; Guo, C.; Wang, M.; Huang, L.; Wang, L.; Mi, C.; Li, J.; Fang, X.; Mao, C.; Xu, S., Controllable Synthesis of Nayf(4) : Yb,Er Upconversion Nanophosphors and Their Application to in Vivo Imaging of Caenorhabditis Elegans. *J Mater Chem* **2011**, *21*, 2632.

132. Bragdon, C. R.; Malchau, H.; Yuan, X.; Perinchief, R.; Kärrholm, J.; Börlin, N.; Estok, D. M.; Harris, W. H., Experimental Assessment of Precision and Accuracy of

Radiostereometric Analysis for the Determination of Polyethylene Wear in a Total Hip Replacement Model. *Journal of Orthopaedic Research* **2002**, *20*, 688-695.

133. Selvik, G., Roentgen Stereophotogrammetric Analysis. *Acta Radiologica* **1990**, *31*, 113-126.

134. Ryd, L.; Albrektsson, B.; Carlsson, L.; Dansgard, F.; Herberts, P.; Lindstrand, A.; Regner, L.; Toksvig-Larsen, S., Roentgen Stereophotogrammetric Analysis as a Predictor of Mechanical Loosening of Knee Prostheses. *Journal of Bone & Joint Surgery, British Volume* **1995**, *77*, 377-383.

135. Kärrholm, J.; Selvik, G.; Elmqvist, L.-G.; Hansson, L. I., Active Knee Motion after Cruciate Ligament Rupture: Stereoradiography. *Acta Orthopaedica Scandinavica* **1988**, *59*, 158-164.

136. Leardini, A.; Chiari, L.; Della Croce, U.; Cappozzo, A., Human Movement Analysis Using Stereophotogrammetry: Part 3. Soft Tissue Artifact Assessment and Compensation. *Gait & posture* **2005**, *21*, 212-225.

137. Bey, M. J.; Derwin, K. A., Measurement of in Vivo Tendon Function. *J Shoulder Elbow Surg* **2012**, *21*, 149-57.

138. Finni, T.; Komi, P.; Lukkariniemi, J., Achilles Tendon Loading During Walking: Application of a Novel Optic Fiber Technique. *European journal of applied physiology and occupational physiology* **1998**, *77*, 289-291.

139. Schepull, T.; Kvist, J.; Andersson, C.; Aspenberg, P., Mechanical Properties During Healing of Achilles Tendon Ruptures to Predict Final Outcome: A Pilot Roentgen Stereophotogrammetric Analysis in 10 Patients. *BMC musculoskeletal disorders* **2007**, *8*, 1.

140. Muramatsu, T.; Muraoka, T.; Takeshita, D.; Kawakami, Y.; Hirano, Y.; Fukunaga, T., Mechanical Properties of Tendon and Aponeurosis of Human Gastrocnemius Muscle in Vivo. *Journal of Applied Physiology* **2001**, *90*, 1671-1678.

141. Oliveira, L.; Peixinho, C.; Silva, G.; Menegaldo, L., In Vivo Passive Mechanical Properties Estimation of Achilles Tendon Using Ultrasound. *Journal of Biomechanics* **2015**.

142. Seynnes, O. R.; Bojsen-Møller, J.; Albracht, K.; Arndt, A.; Cronin, N. J.; Finni, T.; Magnusson, S. P., Ultrasound-Based Testing of Tendon Mechanical Properties: A Critical Evaluation. *Journal of Applied Physiology* **2015**, *118*, 133-141.

143. Gerus, P.; Rao, G.; Berton, E., A Method to Characterize in Vivo Tendon Force–Strain Relationship by Combining Ultrasonography, Motion Capture and Loading Rates. *Journal of biomechanics* **2011**, *44*, 2333-2336.

144. Kay, J.; de Sa, D.; Karlsson, J.; Musahl, V.; Ayeni, O. R., Anterior Cruciate Ligament Rupture: A Family Affair. *Orthopaedic Journal of Sports Medicine* **2015**, *3*, 2325967115616783.

145. Wojtys, E. M., Anterior Cruciate Ligament Injury. *Sports Health* **2015**, *7*, 205-206.

146. Fleming, B. C.; Beynnon, B. D., In Vivo Measurement of Ligament/Tendon Strains and Forces: A Review. *Annals of biomedical engineering* **2004**, *32*, 318-328.

147. Meyer, D.; Jacob, H.; Nyffeler, R.; Gerber, C., In Vivo Tendon Force Measurement of 2-Week Duration in Sheep. *Journal of biomechanics* **2004**, *37*, 135-140.

148. Pichorim, S. F.; Abatti, P. J., Biotelemetric Passive Sensor Injected within Tendon for Strain and Elasticity Measurement. *IEEE TRANSACTIONS ON BIOMEDICAL ENGINEERING BME* **2006**, *53*, 921.

149. Komi, P. V., Relevance of in Vivo Force Measurements to Human Biomechanics. *Journal of Biomechanics* **1990**, *23*, 23-34.

150. Komi, P.; Salonen, M.; Järvinen, M.; Kokko, O., In Vivo Registration of Achilles Tendon Forces in Man. I. Methodological Development. *International journal of sports medicine* **1987**, *8*, 3-8.

151. Brown, T. D.; Sigal, L.; Njus, G. O.; Njus, N. M.; Singerman, R. J.; Brand, R. A., Dynamic Performance Characteristics of the Liquid Metal Strain Gage. *Journal of biomechanics* **1986**, *19*, 165-173.

152. Holden, J. P.; Grood, E. S.; Korvick, D. L.; Cummings, J. F.; Butler, D. L.; Bylski-Austrow, D. I., In Vivo Forces in the Anterior Cruciate Ligament: Direct Measurements During Walking and Trotting in a Quadruped. *Journal of biomechanics* **1994**, *27*, 517-526.

153. West, J. R.; Juncosa, N.; Galloway, M. T.; Boivin, G. P.; Butler, D. L., Characterization of in Vivo Achilles Tendon Forces in Rabbits During Treadmill Locomotion at Varying Speeds and Inclinations. *Journal of biomechanics* **2004**, *37*, 1647-1653.

154. Gregor, R.; Roy, R.; Whiting, W.; Lovely, R.; Hodgson, J.; Edgerton, V., Mechanical Output of the Cat Soleus During Treadmill Locomotion: In Vivo Vs in Situ Characteristics. *Journal of biomechanics* **1988**, *21*, 721-732.

155. Herzog, W.; Archambault, J.; Leonard, T.; Nguyen, H., Evaluation of the Implantable Force Transducer for Chronic Tendon-Force Recordings. *Journal of biomechanics* **1996**, *29*, 103-109.

156. Pourcelot, P.; Defontaine, M.; Ravary, B.; Lematre, M.; Crevier-Denoix, N., A Non-Invasive Method of Tendon Force Measurement. *J Biomech* **2005**, *38*, 2124-9.

157. Richards-Kortum, R.; Sevick-Muraca, E., Quantitative Optical Spectroscopy for Tissue Diagnosis. *Annual review of physical chemistry* **1996**, *47*, 555-606.

158. Sandell, J. L.; Zhu, T. C., A Review of in-Vivo Optical Properties of Human Tissues and Its Impact on Pdt. *Journal of Biophotonics* **2011**, *4*, 773-787.

159. Billinton, N.; Knight, A. W., Seeing the Wood through the Trees: A Review of Techniques for Distinguishing Green Fluorescent Protein from Endogenous Autofluorescence. *Analytical Biochemistry* **2001**, *291*, 175-197.

160. Xu, C. T.; Svenmarker, P.; Liu, H.; Wu, X.; Messing, M. E.; Wallenberg, L. R.; Andersson-Engels, S., High-Resolution Fluorescence Diffuse Optical Tomography Developed with Nonlinear Upconverting Nanoparticles. *ACS nano* **2012**, *6*, 4788-4795.

161. Zhao, J.; Lui, H.; McLean, D. I.; Zeng, H., Automated Autofluorescence Background Subtraction Algorithm for Biomedical Raman Spectroscopy. *Applied spectroscopy* **2007**, *61*, 1225-1232.

162. Dahan, M.; Laurence, T.; Pinaud, F.; Chemla, D.; Alivisatos, A.; Sauer, M.; Weiss, S., Time-Gated Biological Imaging by Use of Colloidal Quantum Dots. *Optics letters* **2001**, *26*, 825-827.

163. Gu, L.; Hall, D. J.; Qin, Z.; Anglin, E.; Joo, J.; Mooney, D. J.; Howell, S. B.; Sailor, M. J., In Vivo Time-Gated Fluorescence Imaging with Biodegradable Luminescent Porous Silicon Nanoparticles. *Nature communications* **2013**, *4*.

164. Van de Lest, C.; Versteeg, E.; Veerkamp, J. H.; Van Kuppevelt, T. H., Elimination of Autofluorescence in Immunofluorescence Microscopy with Digital Image Processing. *Journal of Histochemistry & Cytochemistry* **1995**, *43*, 727-730.

165. Woolfe, F.; Gerdes, M.; Bello, M.; Tao, X.; Can, A., Autofluorescence Removal by Non-Negative Matrix Factorization. *Image Processing, IEEE Transactions on* **2011**, *20*, 1085-1093.

166. Song, B.; Ye, Z.; Yang, Y.; Ma, H.; Zheng, X.; Jin, D.; Yuan, J., Background-Free in-Vivo Imaging of Vitamin C Using Time-Gateable Responsive Probe. *Scientific reports* **2015**, *5*.

167. Meier, R. J.; Simbürger, J. M.; Soukka, T.; Schäferling, M., A Fret Based Ph Probe with a Broad Working Range Applicable to Referenced Ratiometric Dual Wavelength and Luminescence Lifetime Read Out. *Chemical Communications* **2015**, *51*, 6145-6148.

168. Anker, J. N.; Behrend, C. J.; Huang, H.; Kopelman, R., Magnetically-Modulated Optical Nanoprobes (Magmoons) and Systems. *Journal of magnetism and magnetic materials* **2005**, *293*, 655-662.

169. Anker, J. N.; Kopelman, R., Magnetically Modulated Optical Nanoprobes. *Applied physics letters* **2003**, *82*, 1102-1104.

170. Behrend, C. J.; Anker, J. N.; McNaughton, B. H.; Brasuel, M.; Philbert, M. A.; Kopelman, R., Metal-Capped Brownian and Magnetically Modulated Optical Nanoprobes (Moons): Micromechanics in Chemical and Biological Microenvironments. *The Journal of Physical Chemistry B* **2004**, *108*, 10408-10414.

171. Roberts, T. G.; Anker, J. N.; Kopelman, R., Magnetically Modulated Optical Nanoprobes (Magmoons) for Detection and Measurement of Biologically Important Ions against the Natural Background Fluorescence of Intracellular Environments. *Journal of magnetism and magnetic materials* **2005**, *293*, 715-724.

172. Anker, J. N.; Behrend, C.; Kopelman, R., Aspherical Magnetically Modulated Optical Nanoprobes (Magmoons). *Journal of Applied Physics* **2003**, *93*, 6698-6700.

173. Nguyen, K. V. T.; Anker, J. N., Detecting De-Gelation through Tissue Using Magnetically Modulated Optical Nanoprobes (Magmoons). *Sensors and Actuators B: Chemical* **2014**, *205*, 313-321.

174. Nguyen, K. V. Tracking Anisotropic Optical Tracers to Study Biophysical Processes and Cytotoxicity. Dissertation, Clemson University, 2015.

175. Mody, R. M.; Zapor, M.; Hartzell, J. D.; Robben, P. M.; Waterman, P.; Wood-Morris, R.; Trotta, R.; Andersen, R. C.; Wortmann, G., Infectious Complications of Damage Control Orthopedics in War Trauma. *Journal of Trauma and Acute Care Surgery* **2009**, *67*, 758-761.

176. Bauer, T. W.; Schils, J., The Pathology of Total Joint Arthroplasty. *Skeletal radiology* **1999**, *28*, 483-497.

177. Esposito, S.; Leone, S., Prosthetic Joint Infections: Microbiology, Diagnosis, Management and Prevention. *International journal of antimicrobial agents* **2008**, *32*, 287-293.

178. Trampuz, A.; Widmer, A. F., Infections Associated with Orthopedic Implants. *Current opinion in infectious diseases* **2006**, *19*, 349-356.

179. Korostynska, O.; Arshak, K.; Gill, E.; Arshak, A., Review Paper: Materials and Techniques for in Vivo Ph Monitoring. *Sensors Journal, IEEE* **2008**, *8*, 20-28.

180. McNaughton, B. H.; Anker, J. N.; Kopelman, R., Magnetic Microdrill as a Modulated Fluorescent Ph Sensor. *Journal of Magnetism and Magnetic Materials* **2005**, *293*, 696-701.

181. Clark, H. A.; Hoyer, M.; Parus, S.; Philbert, M. A.; Kopelman, R., Optochemical Nanosensors and Subcellular Applications in Living Cells. *Microchimica Acta* **1999**, *131*, 121-128.

182. Clark, H. A.; Hoyer, M.; Philbert, M. A.; Kopelman, R., Optical Nanosensors for Chemical Analysis inside Single Living Cells. 1. Fabrication, Characterization, and Methods for Intracellular Delivery of Pebble Sensors. *Analytical Chemistry* **1999**, *71*, 4831-4836.

183. Clark, H. A.; Kopelman, R.; Tjalkens, R.; Philbert, M. A., Optical Nanosensors for Chemical Analysis inside Single Living Cells. 2. Sensors for Ph and Calcium and the Intracellular Application of Pebble Sensors. *Analytical Chemistry* **1999**, *71*, 4837-4843.

184. Kurabayashi, T.; Funaki, N.; Fukuda, T.; Akiyama, S.; Suzuki, M., Cdse/Zns Quantum Dots Conjugated with a Fluorescein Derivative: A Fret-Based Ph Sensor for Physiological Alkaline Conditions. *Analytical Sciences* **2014**, *30*, 545-550.

185. Wolfbeis, O. S.; Rodriguez, N. V.; Werner, T., Led-Compatible Fluorosensor for Measurement of near-Neutral Ph Values. *Microchimica Acta* **1992**, *108*, 133-141.

186. Bidmanova, S.; Hlavacek, A.; Damborsky, J.; Prokop, Z., Conjugation of 5(6)-Carboxyfluorescein and 5(6)-Carboxynaphthofluorescein with Bovine Serum Albumin and Their Immobilization for Optical Ph Sensing. *Sensors and Actuators B: Chemical* **2012**, *161*, 93-99.

187. Song, A.; Parus, S.; Kopelman, R., High-Performance Fiber-Optic Ph Microsensors for Practical Physiological Measurements Using a Dual-Emission Sensitive Dye. *Analytical chemistry* **1997**, *69*, 863-867.

188. Mini X-Ray Tube System for Xrf. http://amptek.com/products/mini-x-ray-tube/#4.

189. Backgrounder on Biological Effects of Radiation. http://www.nrc.gov/reading-rm/doc-collections/fact-sheets/bio-effects-radiation.html.

190. Hall, E. J., Intensity-Modulated Radiation Therapy, Protons, and the Risk of Second Cancers. *International Journal of Radiation Oncology*Biology*Physics* **2006**, *65*, 1-7.

191. Nano Enabler System Benchtop Molecular Printer. http://www.esco.co.kr/bioforce/brochures/Nano_eNabler_system_brochure_7.pdf (accessed 2016).

192. van der Linden, H. J.; Herber, S.; Olthuis, W.; Bergveld, P., Stimulus-Sensitive Hydrogels and Their Applications in Chemical (Micro) Analysis. *Analyst* **2003**, *128*, 325-331.

193. Jeong, B.; Gutowska, A., Lessons from Nature: Stimuli-Responsive Polymers and Their Biomedical Applications. *Trends in biotechnology* **2002**, *20*, 305-311.

194. Xing, S.; Guan, Y.; Zhang, Y., Kinetics of Glucose-Induced Swelling of P(Nipam-Aapba) Microgels. *Macromolecules* **2011**, *44*, 4479-4486.

195. Matsumoto, A.; Kurata, T.; Shiino, D.; Kataoka, K., Swelling and Shrinking Kinetics of Totally Synthetic, Glucose-Responsive Polymer Gel Bearing Phenylborate Derivative as a Glucose-Sensing Moiety. *Macromolecules* **2004**, *37*, 1502-1510.

196. Wang, D.; Liu, T.; Yin, J.; Liu, S., Stimuli-Responsive Fluorescent Poly (N-Isopropylacrylamide) Microgels Labeled with Phenylboronic Acid Moieties as Multifunctional Ratiometric Probes for Glucose and Temperatures. *Macromolecules* **2011**, *44*, 2282-2290.

197. Farooqi, Z. H.; Khan, A.; Siddiq, M., Temperature-Induced Volume Change and Glucose Sensitivity of Poly[(N-Isopropylacry- Lamide)-Co-Acrylamide-Co-(Phenylboronic Acid)] Microgels. *Polymer International* **2011**, *60*, 1481-1486.

198. Wu, Z.; Zhang, X.; Guo, H.; Li, C.; Yu, D., An Injectable and Glucose-Sensitive Nanogel for Controlled Insulin Release. *Journal of Materials Chemistry* **2012**, *22*, 22788.

199. Matsumoto, A.; Yoshida, R.; Kataoka, K., Glucose-Responsive Polymer Gel Bearing Phenylborate Derivative as a Glucose-Sensing Moiety Operating at the Physiological Ph. *Biomacromolecules* **2004**, *5*, 1038-1045.

200. Richter, A.; Paschew, G.; Klatt, S.; Lienig, J.; Arndt, K.-F.; Adler, H.-J. P., Review on Hydrogel-Based Ph Sensors and Microsensors. *Sensors* **2008**, *8*, 561-581.

201. Murphy, W. L.; Dillmore, W. S.; Modica, J.; Mrksich, M., Dynamic Hydrogels: Translating a Protein Conformational Change into Macroscopic Motion. *Angewandte Chemie International Edition* **2007**, *46*, 3066-3069.

202. Lapeyre, V.; Gosse, I.; Chevreux, S.; Ravaine, V., Monodispersed Glucose-Responsive Microgels Operating at Physiological Salinity. *Biomacromolecules* **2006**, *7*, 3356-3363.

203. Zhang, Y.; Guan, Y.; Zhou, S., Synthesis and Volume Phase Transitions of Glucose-Sensitive Microgels. *Biomacromolecules* **2006**, *7*, 3196-3201.

204. Hoare, T.; Pelton, R., Engineering Glucose Swelling Responses in Poly (N-Isopropylacrylamide)-Based Microgels. *Macromolecules* **2007**, *40*, 670-678.

205. Ravikumar, N. Development and Validation of an Optically-Based Strain Measuring Orthopaedic Screw for Fracture Fixation Implants. Clemson University, 2015.

206. Lake, J. Development and Verification of a Test System to Quantify Strain of an Optical Displacement Indicator and the Design of a Strain Indicating Prototype. Masters, Clemson University, 2013.